Poly(thioketal) Polymers and Their Use in the Formation of Hydrophobic and Hydrophilic Cell-Degradable Tissue Engineering Materials

By

John Robert Martin

Dissertation
Submitted to the Faculty of the
Graduate School of Vanderbilt University
in partial fulfillment of the requirements
for the degree of

DOCTOR OF PHILOSOPHY
in

Biomedical Engineering
May, 2017
Nashville, Tennessee

Approved:

Craig L. Duvall, Ph.D.

Hak-Joon Sung, Ph.D.

Scott A. Guelcher, Ph.D.

Jeffrey M. Davidson, Ph.D.

Lillian B. Nanney, Ph.D.

This work is dedicated to my friends and family

whose encouragement and support made this work possible.

ACKNOWLEDGEMENTS

I would first like to thank my Ph.D. advisor Professor Craig Duvall for the guidance and mentorship he has provided throughout my graduate career. I would also like to thank the members of my committee, Professors Scott Guelcher, Lillian Nanney, Hak-Joon Sung, and Jeffrey Davidson for their experience and insight in helping make this work a success. I would like to thank all of the post-doctoral researchers, graduate students, undergraduate students, and research technicians who contributed to this research and supported my efforts through my career at Vanderbilt. Lastly, I would especially like to thank Dr. Mukesh Gupta, Dr. Fang Yu, Alonda Pollins, Nancy Cardwell, Dr. Jonathan Page, and Dr. Christopher Nelson for their invaluable expertise and contributions to these efforts.

I would like to acknowledge the funding agencies for the financial support of this work, including the Vanderbilt University School of Engineering, the Department of Veterans Affairs, the NIH through grants R21EB012750, R01AR056138, R01EB019409, and T32DK101003, and the NSF through grants DMR-1006558 and DMR-1349604. I would also like to acknowledge the Translational Pathology Shared Resource supported by NCI/NIH Cancer Center Support Grant 2P30 CA068485-14 and the Vanderbilt Mouse Metabolic Phenotyping Center Grant 5U24DK059637-13. qRT-PCR was performed through the Vanderbilt University Molecular Cell Biology Resource Core, while DLS, SEM, and FT-IR were performed through the Vanderbilt Institute of Nanoscale Sciences and Engineering (VINSE).

TABLE OF CONTENTS

Page

DEDICATION iii

ACKNOWLEDGEMENTS iv

LIST OF TABLES vii

LIST OF EQUATIONS x

Chapter

1. Introduction and Significance 1

    Motivation 1
    Molecular basis for chronic wounds 1
    Biodegradable tissue engineering materials 3
    Reactive oxygen species as a trigger for biomaterial responsiveness 5
    Approach 5
    Innovation 7
    Specific aims 8
    Outline 9

2. Background: Hydrolytic and Cell-Mediated Degradation Mechanisms of Biomaterials 10

    Introduction 10
    Hydrolytically-degradable tissue engineering materials and PEUR scaffolds 11
    PEG-based hydrogels 13
    Proteolytically-degradable biomaterials 15
    ROS-responsive materials in biomedical applications 15
    Biomaterials for local delivery of therapeutics to skin wounds 34

3. Synthesis and In Vitro Characterization of PTK-UR Scaffolds 37

    Introduction 37
    Materials and methods 39
    Results 46
    Discussion 53
    Conclusion 58

4. Local Delivery of siRNA from PTK-UR Scaffolds to Promote Diabetic Wound Healing 59

Introduction 59
Materials and methods 61
Results and discussion 70
Conclusion 79

5. Enhanced Cell Viability and In Vivo Degradation of PTK-Crosslinked PEG Hydrogels 81

Introduction..... 81
Materials and methods 84
Results 90
Discussion 96
Conclusion 100

6. Synopsis and Future Directions 102

Summary 102
Concerns and limitations 103
Broader impacts 105
Future work 106
Conclusion 108

BIBLIOGRAPHY 109

Appendix

A. Chapter 3 Supplementary Information 120
B. Chapter 4 Supplementary Information 126
C. Chapter 5 Supplementary Information 133
D. Chapter 6 Supplementary Information 136
E. Detailed Protocols and Additional Unpublished Data 140

LIST OF TABLES

Table Page

Table 1. Characterization of PTK diols. 48
Table 2. Physical properties of PTK-UR and PEUR scaffolds. 52
Table 3. PEG-MAL-PTK polymer characterization values. 92
Table A1. Thermomechanical properties of PTK-UR and PEUR scaffolds and neat polymers. 121
Table A2. PTK-UR and PEUR scaffold components 126
Table A3. Nucleic acid sequences. 130

LIST OF FIGURES

Figure Page

Figure 1. PHD2 signaling in normoxia and hypoxia. 3
Figure 2. Schematic of the approaches used 7
Figure 3. Oxidation responsive polymers. 16
Figure 4. Drug delivery strategy for intracellular drug delivery. 18
Figure 5. Localized, extra-cellular drug delivery schematic. 28
Figure 6. ROS-degradable tissue engineering scaffolds 31
Figure 7. Synthesis and characterization of a family of PTK diols.. 47
Figure 8. Tri-functional isocyanates used in polyurethane scaffolds. 48
Figure 9. PTK-UR and PEUR scaffold mechanical properties 49
Figure 10. SEM images of *in vitro* PTK-UR degradation 50
Figure 11. *In vitro* degradation kinetics of PTK-UR scaffolds 51
Figure 12. Degradation of PTK-UR and PEUR scaffolds made with either LTI or HDIt. 53
Figure 13. PTK-UR scaffolds in subcutaneous rat wounds 72
Figure 14. PTK-UR scaffolds in diabetic and non-diabetic rats. 73
Figure 15. PEUR and PTK-UR scaffolds in diabetic excisional wounds 74
Figure 16. Chemical structure of the micelle-forming diblock copolymer 75
Figure 17. Biochemical evaluation of PTK-UR scaffolds loaded with PHD2-siNPs 76
Figure 18. PHD2-siNP scaffolds for improved tissue regeneration. 78
Figure 19. EDDT-PTK polymer and PEG-MAL-PTK macromer synthesis schemes. 90
Figure 20. PEG-MAL-PTK polymer characterization 91
Figure 21. *In vitro* degradation of PEG-MAL hydrogels. 93
Figure 22. MSCs encapsulation in PEG-MAL hydrogels 94
Figure 23. *In vivo* degradation of PEG-MAL hydrogels. 95

Figure A1. GPC chromatograms of PTK diols 120
Figure A2. SEM images of PTK-UR scaffolds 120
Figure A3. Proposed mechanism for hydroxyl radical degradation of PTK polymers. 122
Figure A4. *In vitro* degradation of full set of PTK-UR scaffolds. 122
Figure A5. H_2O_2 dose-dependent degradation of 900t-PEUR scaffolds. 123
Figure A6. *In vitro* degradation of PTK-UR scaffolds in varying ROS media 123
Figure A7. *In vitro* cell-mediated degradation and cytocompatibility of PTK-UR scaffolds. 124
Figure A8. Subcutaneous wound lengths of implanted scaffolds 126
Figure A9. Subcutaneous wound areas of implanted scaffolds 127
Figure A10. PTK-UR (LTI) scaffolds in subcutaneous rat wounds 127
Figure A11. Camera pictures of diabetic excisional wounds with implanted scaffolds 128

Figure A12. Macrophage presence in PEUR and PTK-UR scaffolds.. 128
Figure A13. *In vitro* screen of PHD2 siRNA..... 129
Figure A14. *In vitro* release of nanoparticles from scaffolds 129
Figure A15. Initial *in vivo* screen of PEUR and PTK-UR scaffolds with PHD2 siNPs..... 130
Figure A16. PTK-UR (HDIt) scaffolds with PHD2 siNPs in diabetic excisional wounds..... 131
Figure A17. Representative comparison of Ki67 and S100A4 IHC staining. 131
Figure A18 Physical characterization of hydrogels. 133
Figure A19. Alternative strategy for synthesizing hydrophilic PTK polymers. 134
Figure A20. Optimized rat ischemic flap model..... 136
Figure A21. Impaired porcine wound healing model featuring..... 137
Figure A22. Laser Doppler perfusion imaging of scaffolds in impaired porcine wounds. 137
Figure A23. Histology of PTK-UR scaffolds in ischemic and non-ischemic porcine wounds.. 138

LIST OF EQUATIONS

Equation Page

Equation 1. First order mass loss model. 44
Equation 2. Swelling ratio determination for PEG-MAL hydrogels. 87

CHAPTER 1

Introduction and Significance

1.1 Motivation

Soft tissue wounds, predominantly in the skin and underlying area, represent a major clinical challenge in the United States and the rest of the world. Skin wounds can be classified as acute or chronic in nature, with acute tissue defects typically arising from trauma or burns and non-healing chronic wounds being categorized as either diabetic ulcers, pressure ulcers, or venous ulcers[1]. The treatment costs of managing chronic wounds in the United States is estimated at $25B annually, and is predicted to significantly increase in the future[1]. This anticipated rise in patients developing chronic wounds is directly tied to the rise in diabetic cases over the past three decades, with the CDC reporting that the incidence and prevalence of diabetes doubled in the US from 1980-2012[2]. Patients with diabetes are more prone to cardiovascular and peripheral arterial disease and impaired wound healing, often helping steer initially simple skin wounds towards chronic ulceration and ultimately leading to limb amputation. Approximately 25% of diabetics develop chronic ulcers[1], and roughly 60% of non-traumatic lower-limb amputations for patients over 20 years old occur in diabetics[3]. The correlation between diabetes and poor skin wound healing outcomes is clear, and as the prevalence of diabetes continues to grow, so will the incidence of amputation caused by chronic skin wounds. These statistics highlight the deleterious impact of diabetes in the United States today and clearly define a tremendous clinical need for improved therapeutic strategies to reduce wound related morbidity and mortality.

1.2 Molecular basis for chronic wounds

The hallmark clinical manifestation of diabetes is sustained hyperglycemia resulting from either the destruction of insulin-producing beta cells in Type 1 diabetes, or insulin resistance in Type 2 diabetes.

Though diabetes is typically managed with a combination of lifestyle modifications and pharmacological interventions, prolonged or unmanaged hyperglycemia has been implicated in many pathologies, including cardiovascular complications, neuropathy, and poor collateral vessel formation[4]. Consequently, small skin wounds or pressure ulcers in diabetic patients may develop into chronic non-healing wounds that do not respond to normal standard of care practices for wound care. These non-healing wounds are particularly challenging due to local tissue hypoxia, inflammation, and high oxidative stress[5, 6]. To alleviate these chronic wounds, more advanced therapies employing biologic drugs or stem cells have been administered in attempts to correct the underlying molecular dysfunction. However, delivery of platelet derived growth factor (PDGF in Regranex®) resulted in incomplete wound healing in 50% of patients in clinical trials [7], while stem cell delivery still suffers from high regulatory burdens and poor clinical outcomes[8].

Recent evidence has implicated diminished activation of the transcription factor hypoxia-induced factor 1-alpha (HIF-1α) in diabetic patients as a key player in the development of chronic wounds[9, 10]. Increasing HIF-1α activation in chronic wounds may help restore normal healing processes as stabilized HIF-1α promotes the expression of multiple reparative genes, including vascular endothelial growth factor (VEGF)[11], angiopoietin-1 (ANG-1)[12], and stromal cell-derived factor-1 (SDF-1)[13]. Prolyl hydroxylase domain protein 2 (PHD2) negatively regulates HIF-1α[14, 15] (depicted in Figure 1) and represents a promising therapeutic target for stabilizing HIF-1α levels *in vivo* to improve tissue regeneration of skin wounds[16-19]. A number of drug agents have been pursued for pharmacological inhibition of PHD2 activity, including small molecule drugs and small interfering RNA (siRNA). Though small molecule inhibitors have demonstrated promising results in promoting wound healing[20-23], they do not specifically target PHD2 among different PHD isoforms and can cause off-target effects[24-26]. siRNA molecules are short, double stranded RNA that load into the RNA induced silencing complex (RISC), a cohort of proteins intrinsic to mammalian cells, to undergo complementary base pairing with target messenger RNA (mRNA) sequences and facilitate mRNA degradation. To selectively inhibit PHD2 activity and promote HIF-1α-mediated wound healing, recent work has pursued the local delivery of PHD2 siRNA for wound healing applications[27-30].

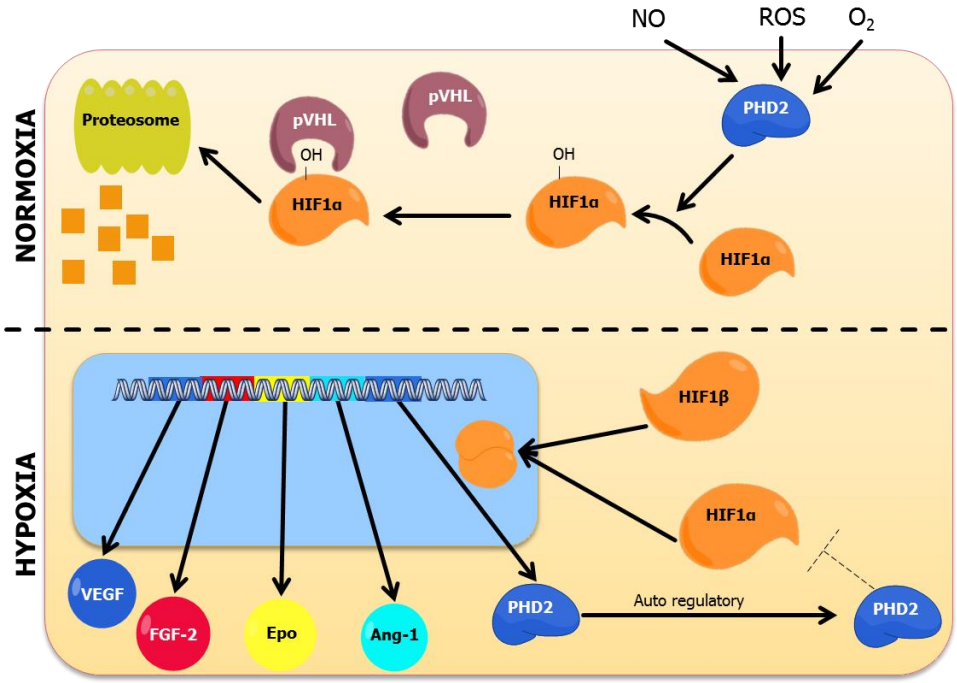

Figure 1. PHD2 signaling in normoxia and hypoxia. During normoxia, the oxygen-dependent PHD2 hydrolyxates HIF-1α, leading to its recognition by the Von Hippel-Lindau Tumor suppressor (pVHL) and subsequent degradation. Alternatively, in hypoxia, PHD2 is inactive from the lack of oxygen and HIF-1α is free to bind with HIF-1β to translocate to the nucleus and begin transcribing pro-growth genes. Adapted from [31].

Though inhibition of PHD2 to promote local HIF-1α stabilization is a promising strategy for promoting healing in chronic wounds, the local delivery of an exogenous PHD2 inhibitory molecule could be limited by depletion of the drug over time. *In situ* delivery of mesenchymal stem cells (MSCs) has been also been pursued in wound healing applications as these cells can modulate local inflammation while secreting paracrine growth factors that promote tissue repair[32]. MSCs implanted at wound sites have been shown to secrete a host of growth factors that can improve wound healing outcomes, including VEGF, insulin-like growth factor (IGF), and keratinocyte growth factor (KGF), among others[33]. Therefore, the *in vivo* delivery of viable stem cells could provide a depot of continuously-produced reparative growth factors as an alternative strategy to promote the repair of non-healing wounds.

1.3 Biodegradable tissue engineering materials

The fields of regenerative medicine and tissue engineering are founded on the usage of bulk-scale biomaterial implants that help direct the repair of damaged or non-functioning tissues or organs. These

biomaterials can have a variety of functions as reviewed previously[34], but often serve as either scaffolds for directing 3D tissue growth, vehicles for the delivery of cells, depots for the controlled release of therapeutic agents, or some combination of these functions. As the long-term implantation of any foreign material inevitably leads to a host response and some degree of immune rejection[35], these biomaterials predominantly feature degradable segments that allow the host to remodel the implant and gradually replace it with new tissue. To this end, these implantable materials must be non-toxic and also feature degradation products that do not promote toxicity or a deleterious immune response. Biodegradable implants fall into two broad classes based on their source: synthetic (i.e. polymers synthesized by conventional organic chemistry techniques), or natural (i.e. re-processed materials extracted from human or animal tissue). Both of these two material classes have different strengths and weaknesses as implantable biomaterials, but the work here has been exclusively focused on the development of synthetic polymeric biomaterials due to their capacity for repeatable fabrication and ease of functionalization.

Biodegradable synthetic biomaterials are typically fabricated to leverage either hydrolysis or enzymatic cleavage of covalent bonds in the material's polymeric backbone for *in vivo* degradation of the construct. Hydrolytically-degradable biomaterials have been utilized in a number of FDA-approved products in the clinic as they are non-cytotoxic, produce nontoxic degradation byproducts, and are cheaply and easily synthesized for a number of applications. However, though the *in vivo* degradation profile of hydrolytically-degradable materials can be nominally tuned by modifying their chemical composition, this material breakdown happens irrespective of the biological tissue response to the implant. This mismatch between new tissue growth and biomaterial degradation can lead to compromised tissue regeneration in certain applications[36], thereby motivating the development of environmentally-responsive materials that are degraded by cell-mediated mechanisms. This has encouraged the incorporation of protease-degradable peptides into a number of tissue engineering materials, thus making these implants specifically degradable by cell-generated enzymes. However, the translational potential of bulk-scale, peptide-based biomaterials remains in question due to the difficulty in synthesizing peptides at large scales[37, 38]. Therefore, there

remains an unmet clinical need for biomaterial implants that are specifically degraded by cell-mediated activity but can be affordably synthesized in large scales.

1.4 Reactive oxygen species as a trigger for biomaterial responsiveness

Reactive oxygen species (ROS), including hydrogen peroxide (H_2O_2), superoxide (O_2-), hypochlorous acid (HOCl), hydroxyl radical, and singlet oxygen, serve as important biological mediators in many biological processes such as cell signaling and the immune response against invading pathogens[39]. However, overproduction of ROS (termed oxidative stress) can damage proteins, rendering them non-functional, and oxidize DNA, causing mutations. Furthermore, elevated ROS is a hallmark of inflammation and the pathogenesis of myriad diseases, including cancer, aging, and neurodegeneration[40]. The number of diseases that are caused or exacerbated by oxidative stress has motivated the development and utilization of biomaterials that can interact with ROS in either a diagnostic or therapeutic capacity[41-43]. Most ROS-sensitive polymers are synthetically-derived and employ straight-forward fabrication techniques, though to date most biomaterial platforms featuring ROS-degradable chemistries have been primarily employed in a nanoscale format to target cell populations with elevated levels of ROS intracellularly. However, polymeric biomaterial implants have been shown to elicit a stable three-fold increase in ROS production at surgery sites over a four-week timeframe [44], and chronic wounds are characterized by high levels of oxidative stress[5, 6]. Consequently, cell-generated ROS represent an intriguing, ubiquitous target for triggering biomaterial degradation *in vivo*.

1.5 Approach

Our work has focused on the development of a polymer chemistry platform technology to fabricate synthetic biomaterials that are specifically degraded by cell-generated ROS. These biomaterials were produced from poly(thioketal) (PTK) polymers that were originally applied for development of nanoparticles that specifically release their cargo “on demand” at sites of oxidative stress [45]. We have extended this polymer chemistry to create a variety of PTK polymers that are amenable to formulation in

very different biomaterial systems, namely hydrophobic polyurethane scaffolds and hydrophilic poly(ethylene glycol) (PEG) hydrogels. Despite the differences in these two distinct classes of materials, both PTK-based polyurethane (PTK-UR) scaffolds and PTK hydrogels are specifically degraded by ROS both *in vitro* and *in vivo.* Compared to benchmark polyurethane and hydrogel biomaterials, these PTK-based constructs have both improved degradation kinetics and an enhanced translational potential due to their affordability and simple fabrication. Furthermore, these two classes of PTK-based biomaterials are both amenable to *in situ* gelation for minimally-invasive delivery in the clinic and can carry therapeutic payloads to improve the healing of chronic wounds.

As outlined in Figure 2A, PTK-UR scaffolds are formed from a PTK diol polymer, a trifunctional isocyanate, and water. The water reacts with the isocyanates to generate carbon dioxide bubbles during the reactive gelling process, thus producing a scaffold with a porous, 3D architecture that is well suited for hosting cellular infiltration after implantation. PTK-UR scaffolds were sensitive to ROS-mediated degradation and underwent controlled biodegradation *in vivo* while hosting robust new tissue formation in implanted materials[30]. These scaffolds were also loaded with siRNA-carrying, environmentally-responsive nanoparticles (NPs) that locally deliver siRNA to scaffold-infiltrating cells. These NPs electrostatically condense siRNA to protect the drug from nuclease degradation, and upon cellular internalization can undergo pH-dependent membrane disruption to mediate siRNA release from endo-lysosomal vesicles into the cytoplasm. Previous efforts demonstrated the utility of this local siRNA delivery platform for the formation of new blood vessels in preclinical *in vivo* proof of concept studies[28], and this work was extended by using the more highly regenerative PTK-UR scaffolds loaded with siRNA-NPs (siNPs) to enhance healing in excisional diabetic wounds[46].

Though PTK polymers are inherently hydrophobic, this chemistry was extended to make thiolated, water-soluble PTK molecules. These hydrophilic PTK polymers could then be combined with a thiol-reactive 4-arm PEG-maleimide (PEG-MAL) macromer to form covalently-linked hydrogels as shown in Figure 2B. These injectable hydrogels were sensitive to ROS *in vitro* and successfully hosted viable MSCs over multiple days in culture. Furthermore, PTK hydrogels displayed more favorable *in vivo* degradation

kinetics than gels crosslinked with a protease-cleavable peptide, indicating that targeting ROS as a biomaterial degradation trigger could be even more potent than exploiting enzymatic mechanisms to promote *in vivo* material break down.

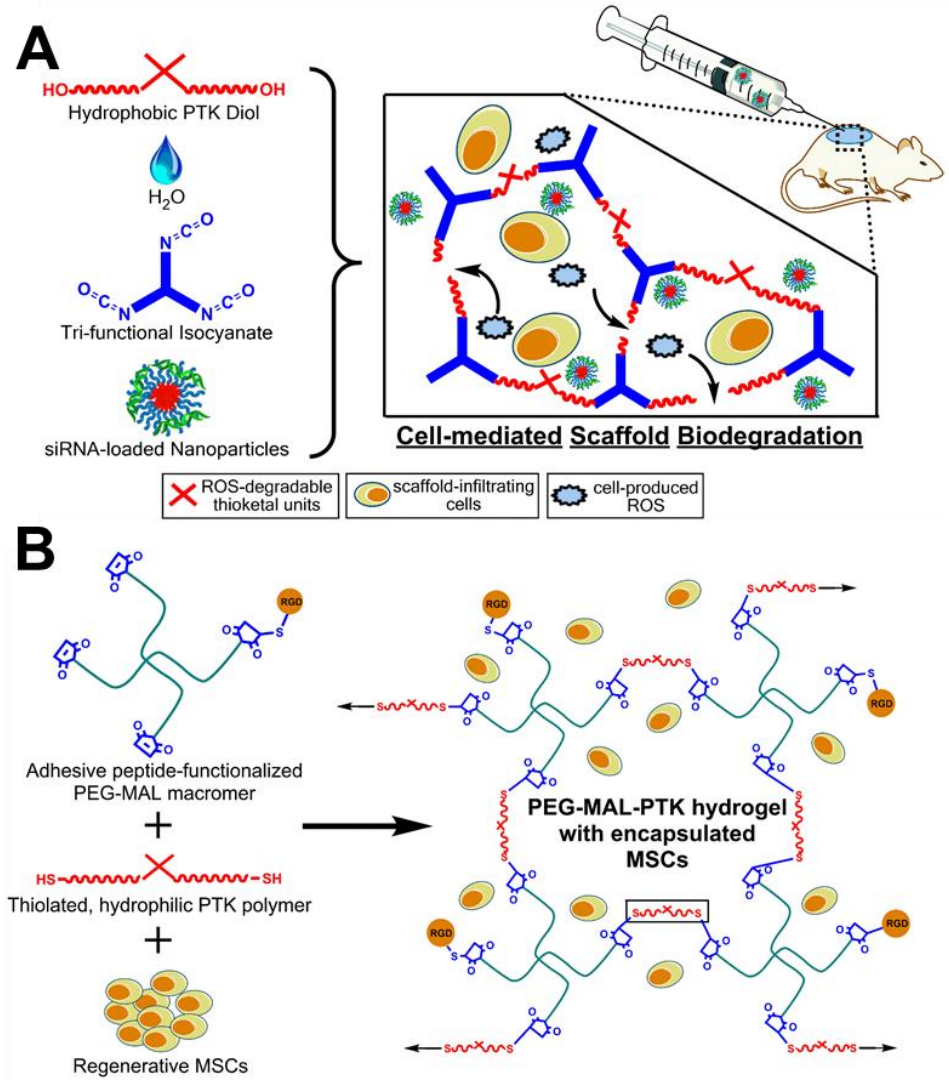

Figure 2. Schematic of the approaches used in these studies. (A) Injectable PTK-UR scaffolds are fabricated from a hydrophobic PTK diol polymer and a trifunctional isocyanate and can also be loaded with siRNA-loaded nanoparticles. (B) Injectable PEG-MAL-PTK hydrogels are fabricated by combining water-soluble, thiol-terminated PTK polymers with 4-arm PEG-MAL macromers. Dispersed MSCs can also be mixed with the hydrogel precursors prior to gelation for 3D cell encapsulation after gel formation.

1.6 Innovation

PTK-UR scaffolds are the first reported example of injectable polyurethane biomaterials that are specifically degraded by ROS, and one of the first synthetic tissue engineering scaffolds overall to feature

exclusively cell-mediated degradation. Though PHD2 siRNA has previously been delivered from polyurethane scaffolds *in vivo*[28], the work presented here is the first to deliver PHD2 siRNA from an implanted scaffold to enhance healing in diabetic wounds in rats. Targeting PHD2 in chronic diabetic wounds to improve healing outcomes is a novel approach and potentially very rewarding scientific pursuit. The creation of a water-soluble PTK polymer is the first report of a hydrophilic PTK material, and the creation of novel PTK hydrogels is the first example of a covalently-linked PEG hydrogel that is exclusively degraded by ROS. Though other hydrogel formulations have featured antioxidant activity or used ROS to drive a change in solubility of hydrophobic domains to mediate hydrogel degradation, PTK-based hydrogels are the first materials to feature ROS-mediated cleavage of covalent bonds to stimulate degradation.

1.7 Specific aims

The central hypothesis of this work is that PTK-based implants that use cell-generated ROS to mediate *in vivo* material degradation will provide a more generalizable, clinically-translatable, and better-performing biomaterial platform than currently used biodegradable materials.

Specific Aim 1: Synthesize and characterize a library of PTK-urethane (PTK-UR) scaffolds from ROS-degradable PTK polymers. PTK polymers will be synthesized by the condensation polymerization of 2,2 dimethoxy propane and different dithiol monomers to create a family of PTK polymers. The size and molecular composition of these polymers will be characterized before incorporating them into 3D, porous PTK-UR scaffolds by reacting them with tri-functional, biocompatible isocyanates and water. Mechanical properties, cytotoxicity, and ROS-dependent degradation of the resultant PTK-UR scaffolds will all be assessed *in vitro*.

Specific Aim 2: Assess the *in vivo* performance of PTK-UR scaffolds for basal tissue regeneration and as a therapeutic siRNA delivery platform. Initial *in vivo* biocompatibility, biodegradation, and tissue infiltration of PTK-URs will be compared against PEUR materials in both subcutaneous and excisional diabetic wounds. Lead PTK-UR and PEUR scaffolds will also be evaluated as local delivery vehicles for endosomolytic nanoparticles complexed with siRNA targeting PHD2 to improve wound

healing in diabetic rats. Therapeutic response to the siRNA-loaded scaffolds will be assessed by qRT-PCR, Western blot, and immunohistochemistry.

Specific Aim 3: Synthesize and characterize PTK-based PEG hydrogels for comparison against proteolytically-degradable hydrogels. Water-soluble, thiol-terminated PTK polymers will be synthesized and characterized before reacting with multi-arm, maleimide-functionalized PEG macromers to form cross-linked PEG hydrogels. PTK hydrogels will be characterized *in vitro* by rheometry, measurements of ROS-dependent gel degradation, and cytotoxicity as benchmarked against hydrogels made with a minimally-degradable PEG crosslinker or gels made with a proteolytically-degradable peptide. Finally, *in vivo* degradation of the three hydrogel formulations subcutaneously implanted in mice will be evaluated by non-invasive fluorescence imaging.

1.8 Outline

This dissertation contains a thorough description of the development of a clinically-translatable, ROS-degradable biomaterial platform. Chapter 2 will provide a concise and targeted review of previous work with biodegradable materials in regenerative medicine. Chapter 3 will detail the *in vitro* development and characterization of PTK-UR materials to confirm their degradability and biocompatibility. Chapter 4 will describe the *in vivo* testing of PTK-UR scaffolds against gold-standard PEUR implants, and illustrate the utility of these materials as an siRNA delivery platform to improve the healing of diabetic wounds. Chapter 5 will consider the usage of PTK polymers in the formation of PEG hydrogels that undergo cell-mediated degradation *in vivo* as an alternative to PEG gels made with enzymatically-degradable peptides. Finally, a summary outlining the broader impacts, challenges, and future work will conclude this dissertation. Each research chapter (3-5) will also contain a short introduction and methods section with their own results and discussions.

CHAPTER 2

Background: Hydrolytic and Cell-Mediated Degradation Mechanisms of Biomaterials

Text partially adapted from:

Martin JR, Gupta MK, Page JM, Yu F, Davidson JM, Guelcher SA, Duvall CL. A porous tissue engineering scaffold selectively degraded by cell-generated reactive oxygen species. Biomaterials. 2014; 35: 12, 3766-3776.

Martin JR, Duvall CL. Oxidation State as a Bioresponsive Trigger. In: T. Dziubla T and D.A. Butterfield, eds. Oxidative Stress in Biomaterials, Academic Press, Cambridge, MA. 2016; 225-250.

Martin JR, Prarthana P, Gupta MK, Duvall CL. Enhanced *In Vivo* Degradation of Injectable, Reactive Oxygen Species-Sensitive PEG Hydrogels. In preparation.

2.1 Introduction

Since the approval of biodegradable sutures in the 1960's, biodegradable tissue engineering materials made from synthetic polymers have been explored as therapies for a number of pathologies in the clinic. The degradability of these substances allows for the clearance of the material from the body, enabling the infiltrated or surrounding host tissue to restore its function after having benefitted from the implanted material. These biodegradable polymer systems have found usage in organ/tissue replacement, chronic wound healing, restoration of critically sized bone defects, and many other applications. To date, however, many biodegradable polymer systems which are degraded by either hydrolytic or enzymatic activity *in vivo* suffer from a number of drawbacks, including high cost of material fabrication and a mismatch between the rates of material degradation and new tissue formation. These material shortcomings have spurred the exploration of synthetic, biodegradable materials that undergo controlled degradation in response to new cellular growth *in vivo* but are economically manufactured.

This chapter reviews currently developed biomaterial technologies and also outlines emerging next-generation material platforms and advanced applications of these systems. The review will begin with a description of biomedically-relevant hydrophobic and hydrophilic synthetic polymer systems that are

degraded by non-specific hydrolysis or enzymatic activity. Next, the development of environmentally-responsive polymer systems that are sensitive to ROS will be examined. Finally, tissue engineering polymer systems that have been used as vehicles for the local delivery of cells or therapeutic drugs will be discussed. As these topic areas are rapidly growing areas of research, the reader is referred to several recent reviews on the following subjects: hydrolytically and enzymatically degradable tissue engineering materials[34], PEG hydrogels[47], biomaterials for skin wound healing[48], ROS-degradable polymer systems[41, 42], local delivery of siRNA therapeutics[49], and stem cell delivery platforms[50].

2.2 Hydrolytically-degradable tissue engineering materials and PEUR scaffolds

Synthetic, biocompatible polymers degraded by hydrolysis, including poly(lactic-*co*-glycolic acid) (PLGA)[51, 52], poly(ε-caprolactone) (PCL)[53, 54], polyanhydrides (PAA)[55, 56], and polyurethanes[57, 58], are the mostly widely explored class of biomaterials and have a history of use in products approved by the FDA[59-62]. These materials are applicable for a diverse range of regenerative applications because they offer a high degree of tunability, generate a minimal host inflammatory response, and degrade into non-cytotoxic components[63, 64] that are resorbed and cleared from the body[65, 66]. Synthetic biomaterials fabricated from polyesters are the most commonly used biodegradable constructs and are degraded by hydrolytic cleavage of ester bonds. Glycolide, lactide, and caprolactone, the most heavily investigated monomeric constituents of biodegradable polyesters, are most often used to form water-insoluble constructs due to the relative hydrophobicity of the monomers, though many hydrogel formulations also feature ester bonds and hydrolytic degradation mechanisms[67]. The degradation rate of polyesters can be tuned using a number of strategies, including copolymerizing monomers with different degradation time scales, tuning the monomer composition of copolymers, and using materials with varying degrees of crystallinity. For example, lactide is a chiral molecule (L-lactide and D-lactide) and polymerized versions of lactide monomers have very different degradation properties depending on the isomeric composition. Poly(L-lactide) (PLLA) is crystalline and takes more than two years for complete *in vivo*

resorption[68], while polymers comprised of a mixture of the two isomers, poly(DL-lactide) (PDLLA), is amorphous and can degrade within 12-16 months[69].

Though the design parameters of polyesters allow for the fabrication of highly tunable biomaterials based on a combination of monomer hydrophobicity, crystallinity, and composition, the hydrolysis of ester bonds is also catalyzed by the presence of acidic by-products. As polyester-based materials degrade, low molecular weight and soluble α-hydroxy acids diffuse from the polymer bulk into the medium resulting in mass loss. However, the scission of ester bonds in the polymer chain forms hydroxyl and carboxylic acid end groups in the polymer bulk. Residual carboxylic acids in the polymer reduce the local pH at later stages of degradation[70, 71], thereby catalyzing accelerated hydrolysis of the polymer[72]. Although α-hydroxy acids are non-toxic and can be cleared from the body[63, 73], autocatalytic degradation of the polyester polymer networks driven by residual carboxylic acid groups can result in a mismatch in the rates of scaffold degradation and new tissue growth.

Injectable PEUR scaffolds

In situ curing, injectable scaffolds such as poly(ester urethanes) (PEURs) that support cellular infiltration and degrade into non-toxic breakdown products represent a particularly promising class of biomaterials[74]. Porous PEUR scaffolds are formed by mixing hydroxyl-functionalized polyols (*e.g.*, 900 g mol^{-1} triols comprised of caprolactone, glycolide, and D,L-lactide)[63] with isocyanate-functional precursors to form a crosslinked network. Water can be added as a blowing agent to create an inter-connected pore structure, and the mechanical, chemical, and degradation properties of the scaffold can be modified through the selection of the polyol and isocyanate precursors[75, 76]. Unlike many other techniques used for fabrication of porous scaffolds, this approach does not require a porogen leaching step. This *in situ* foaming method, combined with the relatively short working time of the reactive liquid mixture[77], renders PEURs useful as injectable and settable scaffolds suitable for minimally invasive procedures in the clinic. PEUR scaffolds have been utilized in a number of regenerative medicine applications, including as scar-reducing skin wound implants[46, 78-80] and as weight-bearing fillers for

critically-sized bone defects[36, 77, 81-83]. Furthermore, PEURs can be used as delivery vehicles for growth factors[36, 63, 77, 78, 81], antibiotics[84], nanoparticles with therapeutic nucleic acids[28, 85, 86], or cell-carrying hydrogel microparticles[87]. Similar to other polyester-based biomaterials, PEUR scaffolds are primarily degraded by hydrolysis but are also somewhat sensitive to oxidation[76]. However, due to the autocatalytic cleavage of ester bonds in the polymeric network structure, the *in vivo* degradation of these scaffolds does not match the growth rate of new tissue in certain applications, leading to resorption gaps and compromised tissue regeneration[36].

2.3 PEG-based hydrogels

In creating biomaterials that closely mimic the natural three-dimensional extracellular matrix, synthetic hydrogels have emerged as promising materials in regenerative medicine applications due to their highly hydrated nature and robust cross-linked polymer networks[88]. Importantly, when compared to naturally derived materials such as collagen or gelatin, artificial matrices offer the advantages of much higher degrees of control over cellular adhesion molecule presentation, manufacturability, material mechanical properties[89]. Due to their intrinsically low protein-adsorption[90], precedent for safe *in vivo* usage, and ease of functionalization[91], PEG-based hydrogels remain the most heavily investigated matrix-mimicking class of synthetic biomaterials. These hydrogels are most commonly formed by the covalent cross-linking of PEG macromers, which swell upon exposure to water due to PEG's hydrophilic nature but do not dissolve due to the covalently linked polymer network. Recent work in the area has focused on *in situ* cross-linking PEG hydrogels that can be delivered in a minimally invasive manner in the clinic (preferably by syringe injection) while maintaining an active depot of living cells[92-94], proteins[95], or drugs[96].

Strategies for inducing *in situ* hydrogel formation include UV cross-linking of acrylate or ene-terminated units in the presence of a photo-initiator[92, 95, 97], enzyme-mediated cross-linking with horseradish peroxidase[98-100], covalent cross-linking induced by click reactions[101, 102], or Michael-type addition[103-105]. Of these cross-linking strategies, photo-polymerization and Michael-type addition

have been the most popular to date. To cross-link acrylate-terminated PEG macromers, UV light is employed to cleave a photoinitiator to spur free-radical polymerization of acrylate end groups[106]. The spatial employment of the UV light source allows for location-dependent fine-tuning of biomolecule incorporation[107] and mechanical properties[89] through additive or subtractive photo-patterning. However, UV light[108] and many photoinitators[109, 110] are inherently cytotoxic and achieving *in situ* photo cross-linking at the hydrogel's *in vivo* delivery site remains difficult due to problems with non-destructively supplying UV light to the tissue area. Conversely, Michael-type addition does not require an exogenous light source or free radicals to achieve polymerization, but instead uses a nucleophilic reagent (such as triethanolamine) to catalyze the addition reaction between a branched, end-functionalized PEG macromer and a bi-functional or multi-functional nucleophilic cross-linker[111]. PEG macromers end-functionalized with acrylate and vinyl-sulfone groups have been previously investigated as components for Michael-addition injectable hydrogels in biomedical applications[103, 105, 112].

Recently, García et al. have explored the use of maleimide-functionalized PEG (PEG-MAL) macromers as precursors for injectable hydrogels formed by Michael-addition cross-linking[93, 94]. Maleimide groups have been extensively used in peptide biochemistry as they quickly and efficiently react with thiol groups with very high specificity at physiological pH levels[113]. When compared to more conventional Michael-addition hydrogel systems featuring acrylate or vinyl-sulfone groups, these PEG-MAL materials possess superior cytocompatibility, increased cross-linking efficiency, and appropriate *in situ* gelation kinetics that make this system ideal for *in vivo* delivery applications[93]. Furthermore, PEG-MAL macromers demonstrate limited cytotoxicity and inflammation *in vivo* while possessing rapid renal clearance of the hydrogel degradation products[94]. In a therapeutic capacity, PEG-MAL hydrogels have shown promise as delivery vehicles for both bioactive, pro-angiogenic proteins and functional pancreatic islets[94]. In all, PEG-MAL hydrogels represent a highly clinically-translatable biomaterial on the cutting edge of minimally-invasive therapeutic delivery systems.

2.4 Proteolytically-degradable biomaterials

In order to tie scaffold degradation to cellular growth, environmentally-responsive polymers have been heavily investigated for the development of smart materials that respond to specific biological stimuli[114]. In particular, biomaterials that degrade by cell-mediated mechanisms, such as materials with protease-cleavable peptides, have been successfully utilized to synthesize environmentally-sensitive tissue engineering constructs such as hydrogels[115, 116] and polyurethanes[117-119]. In particular, recently developed PEG-MAL hydrogels[93, 94] featured a protease-cleavable peptide linker that was specifically tailored to degrade in response to cell-produced enzymes[120]. However, it is difficult to establish this approach as a generalizable tissue engineering platform because these peptide sequences are cleaved by specific enzymes that are upregulated in specific pathological environments[120] and feature highly variable levels across cellular subtypes[121] and patient populations[122]. Also, manufacturing peptides on the scale necessary to fabricate large tissue scaffolds is both expensive and time-consuming with current technology[37, 38]. Development of degradable polymers that can be affordably synthesized in large scales but that target a ubiquitous cell-mediated signal for scaffold degradation may provide a more generalizable and better-performing biomaterial.

2.5 ROS-responsive materials in biomedical applications

The number of diseases that are caused or exacerbated by oxidative stress motivates the development and utilization of biomaterials that can interact with ROS in either a diagnostic or therapeutic capacity. This section outlines the chemistry and function of the different oxidation-responsive polymers currently researched for therapeutic purposes. The most prevalent, biomedically-relevant, ROS-responsive polymers developed to date, along with their degradation products, are summarized in Figure 3. There are two primary classes of polymers that react to oxidative stimuli: (1) those with an oxidation-induced polymer solubility switch and (2) those that undergo oxidation-induced polymer degradation[41]. The polymers that undergo a ROS-mediated solubility switch, including poly(propylene sulfide) (PPS) and selenium-linked polymers, are typically formulated into hydrophobic, water-insoluble materials that can be oxidized by cell-generated

ROS. These polymers' reaction with ROS adds double-bonded oxygen atoms onto the polymer chain and increases the polarity and thus overall hydrophilicity of the polymer. For the micro- or nano-scale particles, this hydrophilic transition drives disassembly of the material[123] and can be leveraged for a number of biomedical applications such as triggered drug release. For polymers that fully degrade in the presence of ROS, including oxalates, phenylboronic esters, thioketals, and oligoprolines, oxidation of the sensitive chemical units in the respective polymer leads to covalent chain scission and the production of low molecular weight degradation products[124]. Since these polymers do not rely on a phase change for their ROS-mediated responsivity, these units can be more easily incorporated into a wide range of hydrophilic or hydrophobic materials.

Oxidation-Responsive Material	Structure and Degradation Products	References
Oxidation-Induced Solubility Switch		
Poly(propylene sulfide)	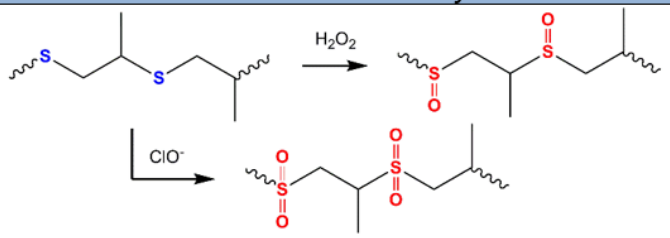	123, 140-152
Selenium-linked polymer	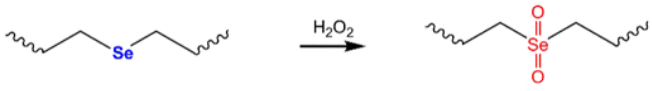	153-157
Oxidation-Induced Degradation		
Poly(oxalate)	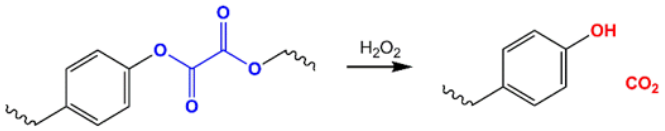	161-165
Phenylboronic ester	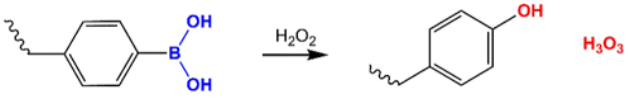	167-176
Thioketal	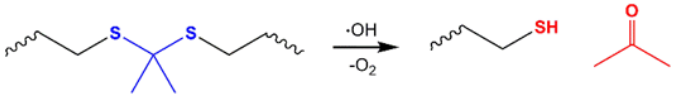	30, 45-46, 124, 177-178, 189
Oligoproline	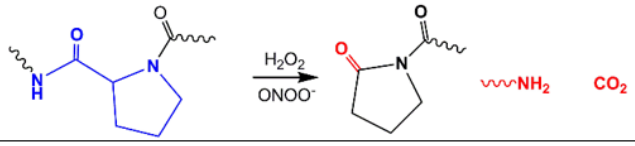	186-188

Figure 3. Oxidation responsive polymers.

Utilizing oxidation-responsive polymers in drug delivery

In the drug delivery field, significant effort over the past twenty years has been aimed at developing targeted delivery technologies to enhance drug potency, decrease off-target effects, and reduce overall treatment costs. Several currently employed drug delivery strategies utilize biodegradable, nano- and macro-scale biomaterials to temporally-sustain drug release[125, 126], though many of these biomaterial drug carriers regulate their payload discharge by simple diffusion or hydrolytic degradation and do not respond specifically within targeted tissue or subcellular locations. To mediate better-directed therapeutic delivery to disease sites, "environmental targeting" that specifically responds to biological stimuli characteristic of the pathological cell and tissue environment remains a promising strategy. Oxidative stress is tied to a number of pathologies, making ROS targeting an effective strategy for selectively delivering a therapeutic payload to diseased cells or tissues. To this end, many groups have employed oxidation-responsive biomaterial drug delivery systems for the ROS-mediated release of therapeutics in both intracellular and extracellular environments.

Polymeric systems for intracellular, oxidation-triggered drug delivery

To date, the majority of work with oxidation-responsive polymers has been focused on the development of nanoparticles that can achieve intracellular drug delivery. Many potential drug targets lie in the cellular cytoplasm and are minimally accessible with currently utilized drug formulations due to substantial delivery barriers[127]. These barriers include poor drug solubility in an aqueous medium, poor cellular uptake due to drug size or charge, and lysosomal degradation following endocytosis. Packaging of a drug into a nanoparticle formulation can not only protect the drug molecule during transit to the cell, but can also help solubilize a poorly-circulating hydrophobic drug[128] or help facilitate cellular uptake[129]. However, to achieve cytosolic drug delivery after endocytic uptake, an ideal nanoparticle formulation must leverage the endosomal environment to escape these cellular vesicles. Previous work has utilized the acidic pH in endolysosomes[130, 131] to achieve endosomal escape, though this stimulus is somewhat ubiquitous across different cell types and does not allow for specific intracellular targeting. However, phagocytic cells[132-

134] and cancer cells[135, 136] are known to produce high levels of ROS in their intracellular compartments, thus making oxidative species a targetable biological stimulus that can facilitate intracellular nanoparticle unpackaging and cytosolic drug delivery. Phagocytic cells, such as neutrophils, dendritic cells, and macrophages, produce increased ROS when immune activated, though an over-production of oxidative species by these cells can also contribute to a number of pathologies[137, 138]. Cancer cells, due to their oncogenic dysregulation and decreased expression of endogenous antioxidant genes[135], constitutively produce higher levels of ROS than analogous non-cancerous cells and also grow more rapidly in response to persistent oxidative stress[136]. Therefore, ROS-mediated targeting of phagocytic and cancerous cells represents a promising strategy for achieving selective intracellular drug delivery as outlined in Figure 4, and has been explored using a number of different oxidation-responsive biomaterial formulations as described in the following sections.

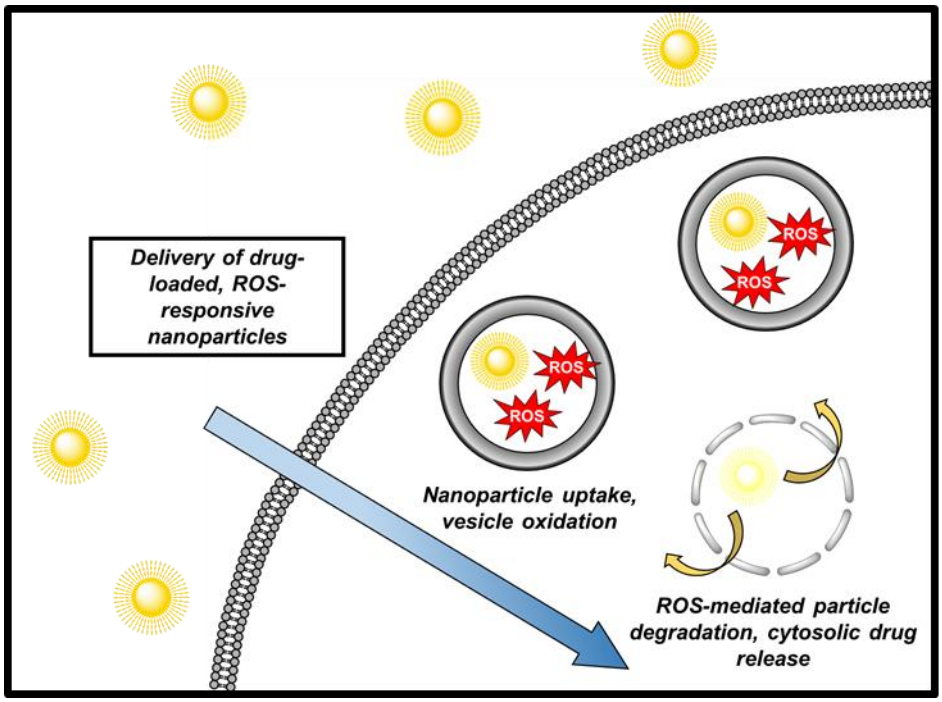

Figure 4. Drug delivery strategy using ROS-responsive materials for intracellular drug delivery.

Poly(propylene sulfide)-based nanoparticles

Sulfur(II)-containing polymers, or polysulfides, have been the most heavily investigated oxidation-responsive materials due to their non-toxic nature, robust response to oxidative environments, and ease of

synthesis[139]. Though these materials have been used in a number of applications over many years, the oxidative-responsiveness of poly(alkylene sulfides) was not reported until 2004 with the pioneering work by Tirelli, Hubbell, et al. exploring ROS-responsive polymersomes. These nanoparticles, formed from a poly(ethylene glycol)-*block*-poly(propylene sulfide)-*block*-poly(ethylene glycol) (PEG-PPS-PEG) triblock polymer, quickly unpackaged in oxidative conditions and thus became the foundational work for research into ROS-responsive polymers[123]. This ROS-responsiveness is caused by the oxidation of the sulfurs in the polymer backbone which increases the hydrophilicity of the bulk polymer and causes a phase change in the PPS as it becomes more water-soluble. Recently, this oxidation of PPS was studied in more detail with respect to different ROS commonly found *in vivo*, exploring oxidation kinetics of PPS incubated with hydrogen peroxide (H_2O_2) and hypochlorite (ClO^-). The less reactive H_2O_2 converted the PPS into poly(propylene sulfoxide) without significant generation of sulfones, while ClO^- treatment caused the rapid formation of sulfones and sulfoxides and spurred dramatic PPS depolymerization. Interestingly, fibroblasts treated with the H_2O_2-generated sulfoxides did not experience significant cytotoxicity while ClO^--generated sulfones were notably cytotoxic[140, 141]. With respect to other commonly encountered oxidative species, PPS is also sensitive to peroxynitrite[142-144] but does not respond to superoxide[145]. In addition to its inherent sensitivity to oxidation, PPS is also a particularly advantageous polymer for use in the formation of self-assembled nanoparticles[142, 146]. PPS is more hydrophobic than its oxygen analogue poly(propylene oxide) (PPO), and PEG-PPS polymers have been shown to form more stable self-assembled nanostructures than commonly used PEG-PPO-PEG Pluronic micelles[146]. Due to its stable nanoparticle formation and sensitivity to a number of different ROS, PPS has thus been used in a host of different biomedical applications for intracellular drug delivery.

Small molecule delivery from PPS nanoparticles

Micellar nanoparticles formed from amphiphilic polymer systems have been recently explored for the delivery of small molecule hydrophobic drugs[128]. Under aqueous conditions, the hydrophobic portion of the polymer forms the core of the nanoparticle and can sequester hydrophobic molecules, while the

hydrophilic polymer segment forms the nanoparticle corona and stabilizes the interface between the hydrophobic core and the aqueous medium. This strategy was first employed with PPS-based nanoparticles for the encapsulation the immunosuppressive drug cyclosporine A. Using PEG-PPS diblock copolymers that readily self-assemble into nanoparticles, up to 19% w/w drug loading was achieved and sustained over 19 days in an aqueous medium, though the ROS-responsiveness was not directly explored in this study[147]. Similar PEG-PPS micelles have also been loaded with an anti-inflammatory drug (mometasone furoate) or immunosuppressive drugs (rapamycin and tacrolimus) for delivery to draining lymph nodes[148]. Though these previous data demonstrate the effectiveness of solubilizing small hydrophobic drugs into PPS-based nanoparticles, they did not specifically study the ROS-responsive nature of PPS for environmental targeting with these drug delivery systems.

However, work by the Tirelli group demonstrated the potential for PPS-based nanoparticles to mediate small molecule drug delivery in response to oxidation. PEG-PPS micelles were conjugated to superoxide dismutase (SOD), a naturally occurring enzyme that converts highly reactive superoxides to more stable H_2O_2. In the body, SOD is paired with the enzyme catalase, a scavenger of H_2O_2, but the synthetic system described here utilizes the conjugated SOD and the H_2O_2-absorbing nature of PPS to mimic this paired functionality. Therefore, this system acts as an ROS scavenger for both superoxide and H_2O_2 while also leveraging the selective absorption of H_2O_2 to mediate on demand release of a model small molecule hydrophobic drug from the nanoparticles' PPS core[145]. Work by Gupta et al. also conclusively demonstrated the potential of oxidative responsiveness of PPS-based nanoparticles in the context of intracellular small molecule delivery. In their study, PPS was extended with a hydrophilic block made via the reversible addition chain transfer (RAFT) polymerization method. This approach yielded self-assembling (N,N-dimethylacrylamide)-*block*-PPS (DMA-PPS) nanoparticles that selectively released their drug cargo in an H_2O_2 dose-dependent manner and also disassembled after incubation with H_2O_2 as confirmed by dynamic light scattering and transmission electron microscopy. Finally, in a Förster resonance energy transfer (FRET)-based study, the DMA-PPS micelles loaded with model small molecule hydrophobic drugs were shown to selectively release their drug cargo after being engulfed by activated,

ROS-producing macrophages[142]. These data collectively indicate the therapeutic potential for PPS-based intracellular delivery of poorly soluble drug molecules to cells that produce high levels of ROS.

PPS nanoparticles as immunotherapy vehicles

As detailed in the previous section, a diblock copolymer architecture has been primarily utilized for small molecule delivery from PPS-based nanoparticles. PPS nanoparticles have also been synthesized by an anionic emulsion ring-opening polymerization where the propylene sulfide monomer was polymerized into PPS while emulsified in an aqueous environment by Pluronic F-127. After PPS polymerization, these particles were also exposed to air to spur the formation of oxidized disulfide bridges between free thiol groups in the polymer bulk to confer additional stability. This synthesis strategy allows for the creation of PEG-stabilized, ROS-responsive PPS nanoparticles that are easily tuned for both size and surface functionalization[149]. Subsequently, Reddy et al. found that 20nm PEG-stabilized PPS nanoparticles were effectively taken up by dendritic cells in the lymph nodes but that analogous 100nm particles were not retained[150]. Further work using these particles as a vaccine delivery system indicated that PPS nanoparticles decorated with surface hydroxyl groups acted as an adjuvant by targeting dendritic cells in mice and priming their complement activation. Moreover, these PPS nanoparticles were conjugated to the model antigen ovalbumin and generated humoral and cellular immunity to the antigen after delivery[151]. For the delivery of a small molecule adjuvant in conjunction with a protein antigen, a polymersome-forming PEG-PPS diblock polymer was utilized and loaded with the antigen ovalbumin and the small molecule gardiquimod or R848. Ovalbumin release was oxidation mediated and promoted antigen presentation, while the small molecule adjuvants promoted dendritic cell activation[152]. This work demonstrates another ROS-mediated biomaterial strategy for immunotherapies derived from PPS-based materials.

Selenium-linked polymer systems for drug delivery

As another member of the oxygen family (group 16 on the periodic table), selenium shares many common attributes with sulfur, including its responsiveness to oxidation. Since the electronegativity of

selenium is lower than that of sulfur, the corresponding bond energy of the C-Se bond is also lower than that of C-S (C-S 272 kJ mol^{-1}; C-Se 244 kJ mol^{-1}) thus making the C-Se bond more susceptible to oxidation[153]. This higher sensitivity to oxidation has spurred recent investigation into selenium containing biomaterials for their potential application in intracellular drug delivery, and much like sulfur-containing polymers, selenium-doped materials undergo a hydrophobic-to-hydrophilic phase change (i.e. minimal covalent bond cleavage) upon oxidation. A number of selenium-containing polymer systems have thus been developed to facilitate ROS-mediated intracellular delivery. Using a step-growth polymerization scheme, a triblock ABA polymer featuring flanking hydrophilic PEG "A" blocks surrounding a central hydrophobic "B" block containing selenium was synthesized and self-assembled into micellar nanoparticles in aqueous conditions. As expected, these particles were more sensitive to oxidative conditions than analogous nanoparticles formed with sulfur and more quickly released their encapsulated drug payload[154].

Selenium-based, self-assembling micellar nanoparticles have also been formulated using charge interactions with a selenium-containing surfactant. A PEG-poly(acrylic acid) (PEG-PAA) diblock polymer dissolved in a basic aqueous solution (in which the PAA would be predominantly deprotonated and anionic) was added to a positively charged selenium-containing surfactant solution, driving self-assembly of the polymer into micelles that disassembled under oxidative conditions[155]. A selenium-containing precursor can also be grafted onto PEG-PAA as a side-chain modification by conjugating to PAA's carboxylic acid, yielding nanoparticles that disassemble in an ROS-containing medium after oxidation of the selenium. Additionally, these particles could also spontaneously re-assemble with the addition of a reducing agent[156]. The Yan group has also reported the synthesis of a selenium-containing, hyperbranched amphiphilic polymer that can selectively release loaded doxorubicin under oxidative conditions[157]. Interestingly, the selenium-containing nanoparticles alone displayed inherent anticancer activity as they were selectively toxic to ROS-generating cancer cells without any drug loading, potentially due to cancer-specific selenium activation of the apoptosis-mediating enzyme caspase-3[158]. For delivering the chemotherapeutic doxorubicin, nanoparticles synthesized with ROS-sensitive selenium were also an order

of magnitude more effective at promoting cancer cell apoptosis compared to an oxidation-inert control polymer. These data indicate that these hyperbranched selenium-containing nanoparticles can play two roles in the treatment of cancer, both as an ROS-targeting drug carrier for efficient intracellular delivery and to provide inherent anticancer effects[157].

Polyoxalate-based nanoparticles for drug delivery and theranostic applications

Polyoxalate polymers are particularly intriguing ROS-responsive biomaterials due to their dual functionalities, both degrading in oxidative environments and also producing chemiluminescence upon interacting with peroxides in the presence of a fluorophore[159]. As oxalates are oxidized by H_2O_2, the high energy intermediate 1,2-dioxetanedione is produced and can complex with and activate an appropriate fluorophore; the decomposition of this complex produces light from the fluorophore's decaying energy state, along with a carbon dioxide (CO_2) byproduct[160]. Since oxalate oxidation is very specifically mediated by H_2O_2, oxalate-based probes are attractive for *in vitro* or *in vivo* detection of this particular cell-generated ROS. Work by the Murthy group first incorporated polyoxalates into a nanoparticle for *in vivo* imaging of H_2O_2, exhibiting this polymer's high selectivity for H_2O_2 over other ROS and imaging inflammation-generated H_2O_2 in the peritoneal cavity of mice[161]. Subsequent to this demonstration, a number of groups have utilized polyoxalates for both diagnostic and therapeutic research. Combining these two aims into a theranostic system, nanoparticles formulated in an emulsion process from Pluronic, hydroxy-benzyl alcohol-incorporated copolyoxalate (HPOX), and fluorescent dyes were used to image H_2O_2 in an inflamed mouse ankle, reduce H_2O_2 in activated macrophages following phagocytosis, and also promote cytosolic delivery of nanoparticle-encapsulated drugs. The reduction in intracellular ROS is thought to result from both the H_2O_2-mediated oxidation of the oxalate bond and the release of the antioxidant hydroxybenzyl alcohol upon oxalate degradation, making these particles a potent agent for both intravital imaging and antioxidant therapies[162]. Besides their intrinsic antioxidant and bio-imaging capabilities, HPOX nanoparticles were also amenable to drug delivery. They have been loaded with the anti-apoptotic agent 4-amino-1,8-napthalimide (4-AN) and shown to selectively release this payload to sites

of elevated H_2O_2 resulting from ischemia/reperfusion injury[163]. HPOX nanoparticles were also utilized for the delivery of the antioxidant/anti-inflammatory vanillyl alcohol (a derivative of the natural product vanillin) for the treatment of ischemia/reperfusion injury, reducing ROS levels and exerting potent anti-apoptotic activity[164]. Vanillin itself can also be polymerized directly into the polyoxalate chain to achieve H_2O_2 and acid-triggered release to inhibit oxidative and inflammatory activity in cells[165].

Phenylboronic ester-based polymer systems for drug delivery

Phenylboronic esters (PBEs), which are cleaved through reaction with ROS, remain one of the most heavily investigated ROS-responsive chemistries in biomaterials research[42]. These chemical units selectively interact with H_2O_2 and generate boronic acid and phenol derivatives upon oxidation[166]. This H_2O_2-selective reaction does not proceed with other ROS such as superoxide, hypochlorous acid, hydroxyl radicals, etc., making PBEs particularly advantageous in applications as intravital, small molecule H_2O_2 imaging agents[167]. For example, PBE chemistry was employed to confer H_2O_2 imaging specificity to an activatable cell-penetrating peptide (ACPP) by covalently coupling fluorescently-tagged polycationic and polyanionic CPPs through a PBE linker[168]. The two respective fluorophores conjugated to the polycation and polyanion CPPs are a FRET pair, causing FRET when covalently linked by the PBE but only displaying donor fluorophore emission upon H_2O_2-mediated PBE cleavage. The cationic CPP is also released upon PBE oxidation and can penetrate nearby cells, thus making this a useful platform for both H_2O_2 imaging and selective drug payload delivery to environments with elevated H_2O_2[168]. Phenylboronic esters have also been used to transform small molecule and protein drugs into pro-drugs by making them selectively activatable at sites of elevated ROS. PBEs conjugated to a matrix metalloproteinase (MMP) inhibitor show promise as a drug that is selectively activated at sites of ischemia and reperfusion injury during stroke[169], and PBE modification of an anti-cancer protein therapeutic leads to specific drug toxicity in ROS-producing cancer cells[170].

PBEs have also recently been utilized to confer ROS-responsiveness to polymeric nanoparticles. The Fréchet group was one of the first to create PBE-based, ROS-responsive nanoparticles by modifying the

naturally derived, water-soluble polymer dextran with pendant boronic esters and fabricating them into particles by oil-in-water emulsion[171]. The PBE-modified dextran was hydrophobic but became water soluble through H_2O_2-mediated cleavage of the PBE groups, causing particle dissolution and drug payload release. Similar to results seen with PPS-based nanoparticles[151], PBE-dextran ROS-responsive nanoparticles more effectively delivered encapsulated antigens to the cytosol of dendritic cells as compared to PLGA particles by targeting these cells' highly oxidative phagosomes[171]. This unique chemistry was also exploited by incorporating PBE units directly into the backbone of a nanoparticle-forming polymer. The Almutairi group copolymerized adipoyl chloride either directly with a boronic ester or with a benzyloxy-spaced boronic ester to yield two polymers with backbones that were degradable by cell-generated ROS[172]. Nanoparticles formed from the polymer with the benzyloxy spacer were more susceptible to H_2O_2-mediated chain scission, displaying H_2O_2 dose-dependent release of an encapsulated drug payload at H_2O_2 concentrations as low as 50μM[172]. These PBE-based nanoparticles have also been shown to release gadolinium oxide (a magnetic resonance imaging (MRI) contrast agent) in an H_2O_2 dose-dependent manner, potentially making these ROS-responsive particles applicable as *in vivo* imaging agents for locating sites of inflammation with non-invasive MRI[173]. Recent work has also incorporated PBE units into β-cyclodextrin (β-CD) nanoparticles for the selective targeting of cancer cells, combining the proven *in vivo* safety and drug-loading capabilities of β-CD with the ROS-responsiveness of phenylboronic esters[174]. These nanoparticles decreased intracellular ROS levels in macrophages, promoted higher levels of apoptosis in cancer cells when loaded with docetaxel compared to the free drug, and more effectively inhibited tumor growth than the free drug after intravenous administration[174].

PBEs can also be combined with other degradable polymer chemistries to create dual-responsive systems. Song et al. synthesized a micelle-forming diblock copolymer with an outer hydrophilic PEG block and a hydrophobic inner block comprised of ROS-sensitive phenylboronic esters and acid-sensitive ortho-esters[175]. As the PBE groups were cleaved off by H_2O_2, carboxylic acid groups were uncovered and catalytically increased the degradation of the ortho-ester groups. By tuning the relative composition between boronic and ortho-esters, a family of micellar nanoparticles with a range of dual-responsive

properties were synthesized and could be used for intracellular drug delivery applications[175]. In closely related work, Song et al. also developed a polymer system that could capture the potentially toxic degradation products resulting from boronic ester degradation[176]. Quinone methides, highly reactive products generated by the oxidation of phenylboronic ester-containing compounds, can potentially react with biomolecules *in vivo* and cause undesirable side effects. To collect these reactive degradation products, an amphiphilic polymer containing ROS-degradable PBE units and primary or secondary amino groups was synthesized; with this composition, the toxicity of the PBE was reduced by the amines which effectively scavenged the quinone methide byproducts[176].

Thioketal nanoparticles in drug delivery

Poly(thioketals) (PTKs) are another class of fully oxidation-cleavable polymers that were first synthesized by the Murthy group for utilization in an ROS-degradable nanoparticle system[45]. PTK polymers are synthesized by a relatively simple condensation polymerization from low molecular weight dithiol precursors, yielding hydrophobic polymers that are amenable to the formation of solid polymeric particles via oil-in-water emulsion[45]. Furthermore, PTK polymers are very specifically degraded by ROS into their original dithiol precursors and acetone (thioketal degradation susceptibility: hydroxyl radical > hydrogen peroxide > superoxide[177, 178]) but are impervious to hydrolysis under all pH conditions. PTK robustness at extreme pH levels (i.e. pH > 13, pH < 1) was initially leveraged to create an orally-administered, small interfering RNA (siRNA) drug delivery system that could traverse the enzymatic and acidic conditions in the stomach to selectively deliver the drug payload to inflamed, ROS-producing sites in the intestines[45]. The siRNA loaded into the PTK nanoparticles targeted the pro-inflammatory cytokine tumor necrosis factor-alpha (TNF-α), primarily produced by activated phagocytes, which plays an essential role in the onset and persistence of intestinal inflammation[179]. The ROS-specific degradation of these nanoparticles effectively targeted these phagocytes as they generate large quantities of both intracellular and extracellular ROS[134, 137]. Therefore, PTK-based nanoparticles synthesized using an emulsion process are not only able to protect drug cargo from the harsh environment of the stomach, but also can

utilize their oxidation-specific degradation to target high levels of ROS at a tissue or cellular level. Further utilizing PTK polymers for the targeting of ROS-producing phagocytic macrophages, Pu et al. incorporated PTK polymers into a chitosan-based nanoparticle system for the intracellular delivery of the antioxidant drug curcumin[124]. The hydrophobic PTK polymer helps to stabilize the hydrophobic nanoparticle core while also conferring ROS-responsiveness for drug release, while the chitosan forms a hydrophilic particle corona that is pH-responsive. These particles showed relatively moderate sensitivity to both pH and ROS individually, but the presence of both stimuli synergistically triggered release of the encapsulated drug. This effect was also translated into *in vivo* efficacy as curcumin-loaded PTK nanoparticles decreased local ROS levels and prevented tissue damage in an inflammation model[124]. This work again demonstrates PTK polymers' ability to target ROS-producing phagocytic cells for drug delivery applications, while also displaying the propensity for integration into multi-functional nanoscale technologies.

Besides targeting phagocytic cells, PTK-based nanoparticle systems have also been utilized to specifically deliver drugs to cancer cells. High levels of intracellular ROS production are a hallmark of many cancers, and heightened ROS production has also been tied to the aggressiveness of certain prostate tumor cells [136]. Therefore, these PTK-based polymer systems utilize elevated intracellular ROS levels to enhance cytosolic drug delivery as the nanoparticles will degrade and release their drug payload upon cellular internalization. For the delivery of a hydrophobic small molecule chemotherapeutic, water-insoluble Paclitaxel was loaded into hydrophobic PTK polymers by oil-in-water emulsion and administered to prostate cancer cells[178]. Non-loaded particles caused minimal cytotoxicity, while drug-loaded particles caused dose-dependent cell death at much lower Paclitaxel doses than previously reported in similar, oxidation-inert nanoparticle delivery systems. To deliver plasmid DNA to cancer cells, Shim and Xia utilized a novel strategy for incorporating thioketal units into a nanoparticle construct by synthesizing a low molecular weight diacrylate thioketal crosslinker and then polymerizing it with a positively-charged oligoamine to create a poly(amino thioketal) (PATK)[177]. These polymers were water soluble (unlike previous PTK polymers), efficiently condensed plasmid DNA, and promoted ROS-induced intracellular drug unpackaging for higher plasmid transfection. This work demonstrates both the potential utility for

synthesis of water soluble PTK-based polymers while reinforcing the concept of ROS-mediated drug targeting of cancer cells by PTK nanoparticles.

Oxidation-responsive polymeric systems for locally targeted, extracellular drug delivery

The majority of the work with oxidation-responsive polymer systems has leveraged cell-generated ROS as an intracellular drug release mechanism. Nanoparticle systems are particularly amenable to this type of drug delivery application as their small size allows for both systemic delivery through intravenous injection and access to the intracellular space through size-based cellular uptake mechanisms[126]. However, size-based diffusion of nanoparticles also decreases their *in vivo* retention as they more readily diffuse away from their site of administration within a few hours[143]. Therefore, larger sized particles or bulk scaffolds and hydrogels that are ROS-degradable remain particularly advantageous for locally sustained drug delivery and tissue engineering applications. Though many ROS have intracellular origins[132], high levels of extracellular ROS are common in many pathologies[134, 180] and thus can be leveraged to achieve drug delivery from micro- or macro-scale therapeutic delivery systems. This local, extra-cellular drug delivery strategy is outlined in Figure 5.

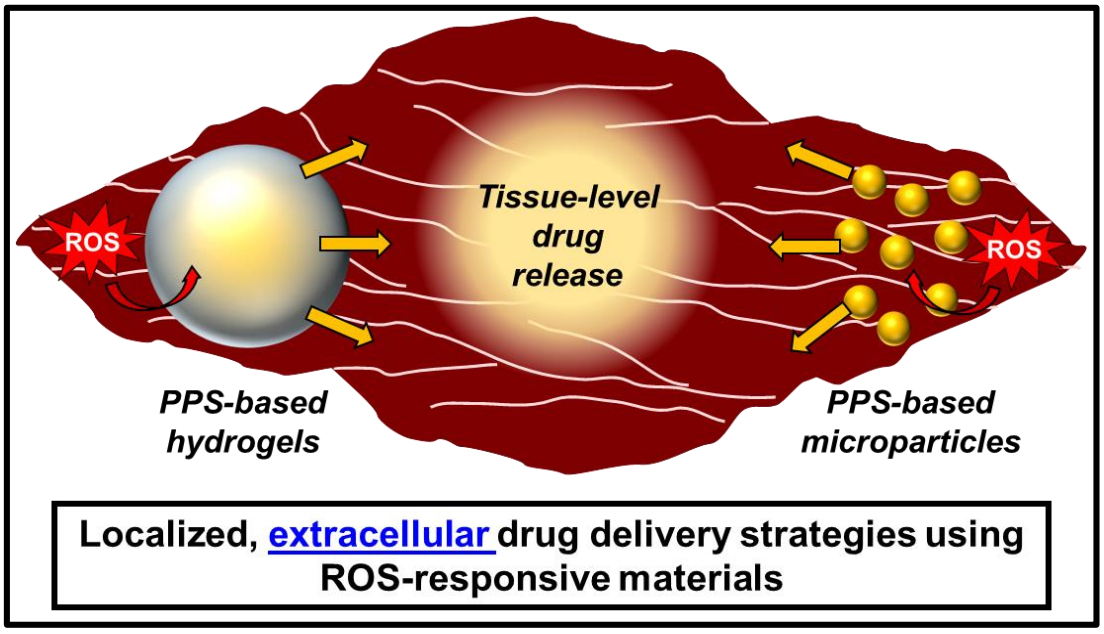

Figure 5. Localized, extra-cellular drug delivery schematic.

Poly(propylene sulfide) microparticles for local drug delivery

Because it was one of the first polymers developed as an oxidation-responsive biomaterial[123], PPS has been tested in several nanoparticle applications as outlined above. The Duvall group was the first to apply PPS in a microparticle format, using this polymer to develop a localized ROS-responsive sustained release platform for the delivery of the hydrophobic drug curcumin[144]. Curcumin is a naturally-derived antioxidant and anti-inflammatory agent that has shown promise in the treatment of ischemia/reperfusion injury[181], though the extreme hydrophobicity of the molecule limits its *in vivo* bioavailability and thus its clinical usage[182]. These particles were fabricated from an oil-in-water emulsion method using conditions that yielded particles on the micron-scale and were developed as an "on demand" delivery system for curcumin; the concept is that the level of environmental ROS present would modulate the rate of release of the antioxidant/anti-inflammatory curcumin molecule. To this end, *in vitro* curcumin release was shown to be dose-dependent in relation to ROS concentrations. Though this microparticle system was designed to achieve local retention for sustained extracellular curcumin release, particles between 1-2 μm are selectively taken up by activated phagocytic cells[183, 184] thus allowing for a combination of extracellular release and selective uptake (due to physical size) of the drug-loaded microparticles by the cells which are the primary producers of ROS. PPS is a known scavenger of H_2O_2[145], and this work also highlighted the therapeutic benefit of using PPS for the particle substrate. Even without drug loading, there was a therapeutic benefit of the "blank" PPS particles in that their presence protected fibroblasts from the cytotoxic effects of exogenous H_2O_2 (and the protective effect of the PPS particles was further enhanced by loading with curcumin). These results were confirmed in mice as ischemic limbs treated with PPS and curcumin-PPS microparticles experienced decreased levels of ROS, while curcumin was also released at a faster rate in the highly oxidative ischemic limbs when compared to non-ischemic controls[144]. This work demonstrates the ability of PPS microparticles to incorporate hydrophobic drugs and selectively release them upon ROS stimulation, while also highlighting the potential therapeutic benefit of these materials as ROS-scavengers both *in vitro* and *in vivo*.

Poly(propylene sulfide)-based hydrogels for local drug delivery

Previous work has demonstrated the highly stable nature of micelles synthesized with a PPS core, as the polymer's extremely hydrophobic nature drives robust self-assembly in aqueous media[142, 146]. This chemistry was extended by Gupta et al. using a unique combination of anionic and RAFT polymerization to create an ABC triblock copolymer of PPS-*block*-(*N*,*N*-dimethylacrylamide)-*block*-(*N*-isopropylacrylamide) (PPS-*b*-PDMA-*b*-PNIPAAM)[143]. This polymer self-assembles into micellar nanoparticles in aqueous conditions (driven by the hydrophobic PPS "A" block) but forms a supramolecular hydrogel when heated to physiologic temperatures (driven by the thermo-responsive solubility transition of the PNIPAAM "C" block). The hydrophilic PDMA "B" block helps to maintain the hydration of the formed gels. These materials were synthesized as a ROS-degradable hydrogel that could use oxidative conditions to facilitate on demand drug release and material biodegradation. The hydrophobic PPS domains in the nanoparticles were pre-loaded with a model hydrophobic small molecule drug, and after thermo-gelation released the drug payload from the bulk hydrogels in an ROS-concentration dependent manner. These drug-loaded hydrogels also demonstrated *in vivo* drug release as subcutaneously injected hydrogels gradually released their drug payload over 14 days, validating that *in vivo* ROS concentrations are sufficient to promote localized drug delivery from these materials[143].

Utilizing oxidation-responsive polymers in biodegradable tissue engineering scaffolds

Biodegradable scaffolds made from synthetic polymers have been extensively investigated for use in tissue engineering and regenerative medicine. These materials, including PLGA, PCL, and polyurethanes, are applicable for a diverse range of regenerative applications because they offer a high degree of tunability, generate a minimal host inflammatory response, and degrade into non-cytotoxic components[63, 64] that are resorbed and cleared from the body[65, 66]. However, the biodegradation of these materials, primarily mediated by hydrolysis of ester bonds in the polymer backbone, produces acidic byproducts which can catalyze accelerated polymer hydrolysis[72] and result in a mismatch in the rates of scaffold degradation and tissue in-growth that leads to resorption gaps and compromised tissue regeneration[36]. Therefore,

many recent efforts in tissue engineering have focused on the development a more generalizable and better-performing biomaterial created from degradable polymers that can be affordably synthesized in large scales, similar to polyesters, but that target a ubiquitous cell-mediated signal for scaffold degradation. Scaffolds degraded by cell-generated ROS are a promising candidate because ROS serve as important biological mediators in many normal biological processes[39], and elevated ROS is a hallmark of inflammation and the pathogenesis of myriad diseases[40]. Importantly, polymeric biomaterial implants have also been shown to elicit a stable three-fold increase in ROS production at surgery sites over a four-week timeframe[44], further highlighting the potential utility of this cell-generated signal as a trigger for material degradation. This strategy is highlighted in Figure 6.

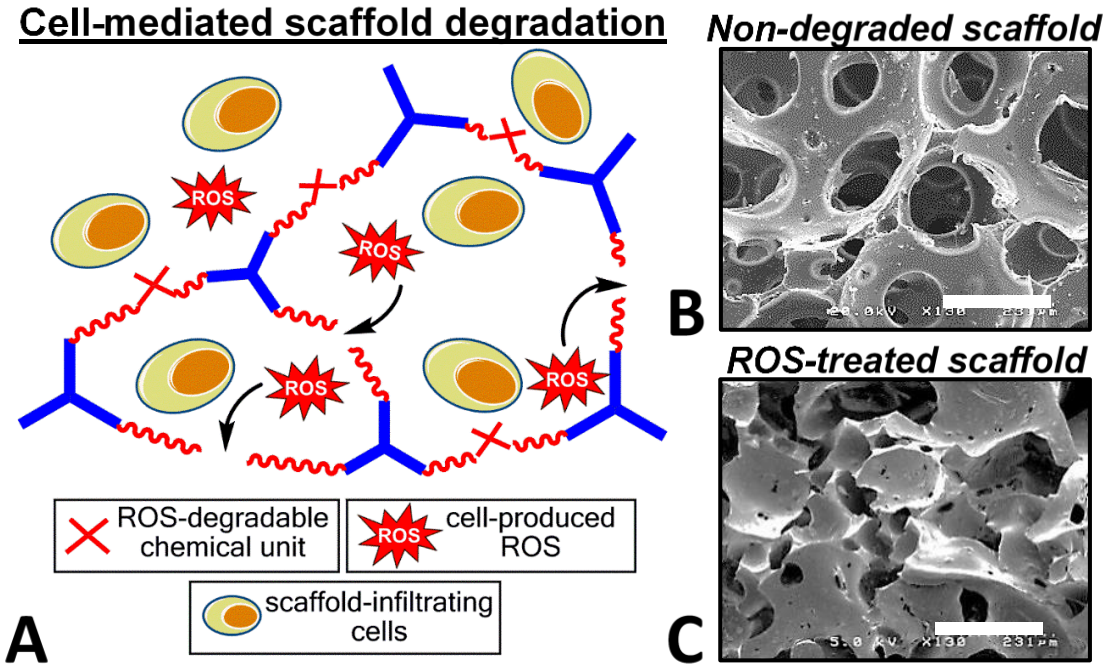

Figure 6. ROS-degradable tissue engineering scaffolds. (A) Schematic for the cell-mediated degradation of oxidation-sensitive scaffolds, which maintain (B) an intact structure before (C) being degraded by ROS.

Oligoproline peptide-crosslinked scaffolds

The incorporation of cell-degradable peptides into tissue engineering scaffolds has been heavily investigated as a strategy to confer specific protease biodegradability to different classes of biomaterials[115-118]. Interestingly, many specific amino acids are also susceptible to oxidative

degradation[185], and ROS-induced peptide cleavage has been effectively utilized for oxidation-targeted nanoparticle delivery of plasmid DNA[186]. These findings motivated the creation of bulk-scale biomaterials crosslinked with oxidation sensitive peptides, a material design strategy first employed by the Sung group by incorporating proline oligomers into a salt-leached, porous, PCL-based tissue engineering scaffold[187]. The oligoproline crosslinked materials underwent significant degradation over 28 days when incubated in oxidative conditions, as compared to scaffolds crosslinked with a non-degradable crosslinker which remained relatively inert due to the high content of slowly-degrading PCL. Furthermore, when incubated with activated, ROS-producing macrophages, the proline-linked scaffolds developed extensive surface pitting indicative of cell-mediated material degradation[187]. This proof of concept work demonstrated the potential utility of these scaffolds as ROS-degradable tissue engineering constructs, and was further expanded to *in vivo* experimentation by subcutaneously implanting oligoproline-crosslinked PCL scaffolds into mice[188]. These scaffolds encouraged a more robust cellular infiltration and increased blood vessel formation compared to PCL or non-degradable crosslinked PCL scaffolds, potentially due to the degradation of the oligoproline crosslinks through ROS associated with the early inflammatory response following scaffold implantation. Thus, the incorporation of oxidation-sensitive oligoprolines into ester-based biomaterials may be a means to enhance performance of conventional degradable biomaterials.

Injectable poly(thioketal-urethane) scaffolds

In situ curing, injectable tissue engineering scaffolds such as poly(ester urethanes) (PEURs) represent a promising class of biomaterials due to their minimally-invasive delivery mechanism, support of cellular infiltration, non-toxic degradation products, and ability to completely fill irregularly-sized tissue defects[74, 77]. PEUR scaffolds are formed by mixing hydroxyl-functionalized polyols (e.g., 900 g mol^{-1} triols comprised of caprolactone, glycolide, and D,L-lactide) with isocyanate-functional precursors to form a crosslinked network. Once implanted *in vivo*, however, PEUR implants, like all polyester-based materials, are sensitive to acid-catalyzed hydrolysis; this autocatalytic degradation mechanism can limit the effectiveness of polyesters in slowly healing injury sites as the scaffold can undergo sudden, late-stage

failure or pore-collapse prior to being fully infiltrated with new tissue[36]. To overcome this limitation, the Duvall group replaced the ester-based polyol with novel, ROS-degradable, hydroxyl-terminated poly(thioketal) (PTK) polymers and incorporated them into injectable, porous PTK-urethane (PTK-UR) scaffolds[30]. PTK-UR scaffolds were selectively degraded by ROS but were stable under aqueous conditions over 25 weeks, indicating their exclusively cell-mediated biodegradation as opposed to PEURs and other polyester-containing materials that hydrolytically degrade independent of cellular activity. Moreover, the *in vitro* oxidative degradation rates of the PTK-URs followed first-order degradation kinetics and displayed dose-dependent degradation with respect to ROS concentration. The PTK-UR scaffolds also supported robust cell infiltration and granulation tissue formation *in vivo*, and were proven to undergo controlled, first-order kinetics of biodegradation *in vivo*. This was in contrast to PEUR scaffolds which experienced accelerated rates of *in vivo* degradation over time, as predicted by the autocatalytic degradation mechanism[30]. These collective results indicate that PTK polymers are particularly amenable to tissue engineering scaffold formation due to their selective ROS-mediated degradation, excellent *in vivo* cytocompatibility, and first-order degradation rates. PTK-UR scaffolds have also been recently utilized as drug delivery vehicles in diabetic wound healing[46] and as the binder component in bone cements[189].

Thermoresponsive poly(propylene sulfide)-based hydrogels

As previously highlighted, thermoresponsive hydrogels formed from ABC triblock polymer micelles (PPS-b-PDMA-b-PNIPAAM) show tremendous promise as injectable drug depots for long-term, ROS-mediated delivery of hydrophobic small molecule drugs[143]. These materials also show great promise in regenerative medicine applications as ROS-degradable, injectable hydrogels that are inherently anti-oxidative and amenable to cell delivery. When the hydrogel is exposed to ROS, the PPS core transitions to the more hydrophilic poly(propylene sulfoxide) and finally to poly(propylene sulphone) which triggers disassembly of the nanoparticles[123] and degradation of the macro-scale hydrogel. These PPS-based hydrogels undergo ROS-mediated degradation as demonstrated by a loss in mechanical integrity after incubation with H_2O_2 and decreasing mechanical properties after incubation with SIN-1 (a peroxynitrite

generator[190]). Similar to results seen with PPS microparticles[144], these PPS hydrogels also protected fibroblasts from cytotoxic levels of H_2O_2 and were able to encapsulate and deliver viable fibroblasts in *in vitro* proof of concept testing. Therefore, ROS-degradable PPS hydrogels with "ROS sponge" activity have broad potential use in regenerative medicine applications as tissue scaffolds, drug delivery depots, and vehicles for cell delivery.

In summation, oxidation-responsive polymer systems possess a number of benefits for the treatment and diagnosis of pathologies characterized by high levels of ROS. Utilizing elevated concentrations of ROS to promote intracellular and extracellular drug delivery has shown promise in the treatment of many disease states, and the use of ROS-degradable tissue engineering scaffolds represent a new paradigm for the fabrication of cell-degradable materials for regenerative medicine applications. Future work is needed to properly characterize the *in vivo* degradation kinetics of these materials, and to explore the toxicity and clearance of these materials' degradation byproducts before full clinical translation is feasible. However, the assortment of currently employed ROS-responsive polymers and their varying performance characteristics presents a promising platform for new exploration and development of advanced therapies for a variety of diseases.

2.6 Biomaterials for local delivery of therapeutics to skin wounds

Since chronic skin wounds are a highly localized pathology, the systemic administration of pro-healing therapeutics can be avoided to minimize off-target effects and maximize the therapeutic concentration directly at the wound site. Though local therapeutic delivery also suffers from many challenges[191], a biomaterial implanted into a skin wound has direct contact with the target tissue and can potentially mediate a more powerful healing response. Chronic wounds have an especially high risk of bacterial infections[192], and hydrophobic tissue engineering scaffolds and hydrogels loaded with antibiotics have been used to increase local healing[84, 193]. Small hydrophobic drugs have also been locally delivered from hydrophobic scaffolds to improve blood vessel formation[194] or increase cell proliferation[195] in skin wounds. Though most commonly used hydrogel formulations are not well suited for the sustained delivery

of small hydrophobic molecules due to these materials' hydrophilic nature and large diffusional capacity, some strategies have recently emerged for local delivery of small molecules from hydrogels. Recently developed hydrogels that feature hydrophobic nanodomains within the gel structure can mediate sustained *in vivo* delivery of hydrophobic drugs[21, 143], while hydrogels that solidify with cyclodextrin-adamantane guest/host reactions can sequester small molecules based on drug affinity to the cyclodextrin moieties and slowly release them over time[196].

The local delivery of growth factors from wound-implanted biomaterials has arguably been the most highly researched strategy for mediating the regeneration of chronic, non-healing wounds. Epidermal growth factor (EGF), vascular endothelial growth factor (VEGF), fibroblast growth factor (FGF), platelet-derived growth factor (PDGF), have all been extensively investigated for their role in wound repair and remain intriguing therapeutic agents to improve wound healing[78, 197-199]. However, the clinical efficacy of growth factor delivery remains limited; delivery of PDGF from a hydrogel dressing had minimal effectiveness in hypertensive leg ulcers in phase III studies [200], while topical administration of VEGF to diabetic foot ulcers had a nonsignificant increase in the healing rate of diabetic ulcers in phase I trials[201]. The relatively poor performance of local growth factor delivery for regenerating non-healing wounds can potentially be attributed to abundant levels of growth factor-degrading proteases in chronic wounds[202] or the over-simplified approach of delivering a single factor to stimulate complex biological healing processes[198]. As such, more work is needed to implement this therapeutic delivery strategy in the clinic.

To promote more advanced healing processes through local therapeutic delivery, many groups have recently begun exploring the deployment of nucleic acids (namely plasmid DNA or siRNA) to promote wound healing. Plasmid DNA delivery, though less efficient than viral gene transfer, is a promising strategy for expressing a therapeutic gene for wound healing applications. Sustained delivery of plasmid DNA from implanted scaffolds has been used to increase the local gene expression of PDGF[203], SDF-1[204], or KGF[205], with scaffold-mediated plasmid delivery demonstrating better efficacy than direct topical delivery of the DNA[206]. The local delivery of siRNA has the potential to selectively silence the expression of target genes in order to reduce the expression of deleterious proteins or to block the expression

of regeneration-inhibiting protein antagonists. Scaffold-mediated gene silencing through *in vivo* siRNA delivery to improve wound healing has been explored for matrix metalloproteinase-9 (MMP-9)[207], connective tissue growth factor (CTGF)[208], p53[209], and PHD2[27-29, 46]. Currently there is one ongoing clinical trial utilizing local siRNA delivery to enhance wound healing by decreasing scar formation after surgery. RXi-109 (RXi Pharmaceuticals, Marlborough, MA) delivers siRNA against CTGF from a collagen/silicone membrane and has been shown to decrease the formation of hypertrophic dermal scars and keloids in initial results from phase 2a trials[210], highlighting the potential utility of siRNA in wound healing applications. Despite the promising early results, implementation of local nucleic acid delivery in wounds is hampered by substantial delivery barriers, including degradation by endogenous nucleases, inability to access the cytoplasm, and insufficiently sustained bioactivity in the target tissue[211, 212]. However, the potential of nucleic acid therapeutics justifies their continued exploration and refinement for the development of next-generation chronic wound therapies.

Finally, the delivery of regenerative mesenchymal stem cells (MSCs) has also been heavily explored as a strategy for improving the healing of chronic wounds. Biomaterial-mediated delivery of single (or even several) therapeutic drugs can only partially recapitulate complex regenerative signaling pathways that normally collaborate during wound healing, thereby motivating the delivery of regenerative cells to wound sites. MSC therapies can orchestrate a diversity of processes, including direct epidermal differentiation[213], modulation of inflammatory response[32, 214], and paracrine stimulation of other cells to adopt reparative phenotypes[32]. Stem cells delivered in fibrin sprays[215], nanofiber scaffolds[216], antioxidant hydrogels[217-219], or in collagen sponges[220, 221] have been successfully delivered to chronic wounds and have helped orchestrate an enhanced healing response. Though testing of stem cell therapies have indicated that MSC delivery is safe in patients, the overall clinical therapeutic efficacy has been relatively modest[222] primarily due to poor cellular retention and survival in the wound [217]. To this end, there is a significant need for innovative new strategies to improve the engraftment and viability of MSCs after delivery to chronic wounds.

CHAPTER 3

Synthesis and In Vitro Characterization of PTK-UR Scaffolds

Text partially adapted from:

Martin JR, Gupta MK, Page JM, Yu F, Davidson JM, Guelcher SA, Duvall CL. A porous tissue engineering scaffold selectively degraded by cell-generated reactive oxygen species. Biomaterials. 2014; 35: 12, 3766-3776.

Martin JR, Nelson CE, Gupta MK, Yu F, Sarett SM, Hocking KM, Pollins AC, Nanney LB, Davidson JM, Guelcher SA, Duvall CL. Local delivery of PHD2 siRNA from ROS-degradable scaffolds to promote diabetic wound healing. Advanced Healthcare Materials. 2016; DOI 10.1002/adhm.201600820

3.1 Introduction

Biodegradable scaffolds made from synthetic polymers have been extensively investigated for use in tissue engineering and regenerative medicine. Examples include poly(lactic-*co*-glycolic acid) (PLGA) [51, 52], poly(ε-caprolactone) (PCL) [53, 54], polyanhydrides (PAA) [55, 56], and polyurethanes [57, 58], all of which have a history of use in products approved by the FDA [59-62]. These materials are applicable for a diverse range of regenerative applications because they offer a high degree of tunability, generate a minimal host inflammatory response, and degrade into non-cytotoxic components [63, 64] that are resorbed and cleared from the body [65, 66].

In situ curing, injectable scaffolds such as poly(ester urethanes) (PEURs) that support cellular infiltration and degrade into non-toxic breakdown products represent a particularly promising class of biomaterials [74]. Porous PEUR scaffolds are formed by mixing hydroxyl-functionalized polyols (*e.g.*, 900 g mol^{-1} triols comprised of caprolactone, glycolide, and D,L-lactide) [63] with isocyanate-functional precursors to form a crosslinked network. Water can be added as a blowing agent to create an inter-connected pore structure, and the mechanical, chemical, and degradation properties of the scaffold can be modified through the selection of the polyol and isocyanate precursors [75, 76]. Unlike many other techniques used for fabrication of porous scaffolds, this approach does not require a porogen leaching step.

This *in situ* foaming method, combined with the short working time of the reactive liquid mixture [77], renders PEURs useful as injectable and scaffolds suitable for minimally invasive procedures in the clinic.

PEUR scaffolds are primarily degraded by acid-catalyzed hydrolysis of ester bonds in the amorphous soft segment, resulting in chain scission and formation of hydroxyl and carboxylic acid end groups. Residual carboxylic acids in the polymer reduce the local pH at later stages of degradation [70, 71], thereby catalyzing accelerated hydrolysis of the polymer [72]. As the polymers degrade, low molecular weight and soluble α-hydroxy acids diffuse from the scaffold into the medium, resulting in mass loss. Although α-hydroxy acids are non-toxic and can be cleared from the body [63, 73], autocatalytic degradation of the PEUR network driven by residual carboxylic acid groups can result in a mismatch in the rates of scaffold degradation and tissue in-growth that leads to resorption gaps and compromised tissue regeneration [36].

Environmentally-responsive polymers have been heavily investigated for the development of smart materials that respond to specific biological stimuli [114]. In particular, biomaterials that degrade by cell-mediated mechanisms, such as materials with protease-cleavable peptides, have been successfully utilized to synthesize environmentally-sensitive nanoparticles [223, 224], hydrogels [115, 116], and polymeric scaffolds [117, 118]. However, it is difficult to establish this approach as a generalizable tissue engineering platform because these peptide sequences are cleaved by specific enzymes that are upregulated in specific pathological [120] and feature highly variable levels across patient populations [122]. Also, manufacturing peptides on the scale necessary to fabricate large tissue scaffolds is both expensive and time-consuming with current technology [37]. Development of degradable polymers that can be affordably synthesized in large scales, similar to polyesters, but that target a ubiquitous cell-mediated signal for scaffold degradation may provide a more generalizable and better-performing biomaterial. Scaffolds degraded by cell-generated reactive oxygen species (ROS) are a promising candidate because ROS serve as important biological mediators in many normal biological processes [39], and elevated ROS, or “oxidative stress”, is a hallmark of inflammation and the pathogenesis of myriad diseases [40]. Polymeric biomaterial implants have also been shown to elicit a stable three-fold increase in ROS production at surgery sites over a four-week timeframe [44], further highlighting the potential utility of this cell-generated signal as a trigger for material

degradation. This has motivated the recent emergence of new classes of ROS-responsive polymer-based nanoparticles [45, 123, 142, 171, 172, 177] and development of salt-leached, porous scaffolds composed of a combination of the polyester PCL and ROS-sensitive, proline-based peptides [187].

Here we sought to develop a generalizable, cell-degradable polyurethane scaffold formulated from polyols exhibiting ROS-dependent degradation. To do so, we synthesized a class of polyols based on ROS-degradable poly(thioketals). Poly(thioketals) (PTKs) were recently applied in orally-delivered nanoparticles that remain stable through the stomach and specifically release their cargo "on demand" at sites of ulcerative colitis [45]. To date, however, this unique polymer chemistry has solely been utilized in targeted nanoparticle drug delivery applications [45, 177]. Herein, we report the development and testing of PTK macrodiols amenable to synthesis of injectable, porous poly(thioketal)-urethane (PTK-UR) tissue engineering scaffolds that are selectively degraded by cell-generated ROS. These fully synthetic scaffolds have been developed to further explore utilization of an ROS-dependent degradation mechanism in order to yield scaffolds with better matched rates of cellular infiltration and degradation.

3.2 Materials and methods

Materials

All chemicals were purchased from Sigma-Aldrich (Milwaukee, WI) except the following. 2-mercaptoethyl ether (MEE), glutaraldehyde, and cobalt chloride were purchased from Fisher Scientific (Pittsburgh, PA), and the tertiary amine catalyst (TEGOAMIN33) was obtained from Goldschmidt (Hopewell, VA). Glycolide and D,L-lactide were obtained from Polysciences (Warrington, PA). Coscat83, an organobismuth urethane catalyst, was supplied by ChasChem, Inc. (Rutherford, NJ). Hexamethylene diisocyanate trimer (HDIt, Desmodur N3300A) was received as a gift from Bayer Material Science (Pittsburgh, PA). Lysine triisocyanate (LTI) was obtained from Kyowa Hakko USA (New York, NY). Cell culture reagents, including Dulbecco's Modified Eagle Medium (DMEM), fetal bovine serum (FBS), and penicillin/streptomycin were supplied by Gibco Cell Culture (Carlsbad, CA). All materials were used as received unless otherwise indicated.

PTK dithiol synthesis

The condensation polymerization protocol for PTK prepolymer synthesis was adapted from Wilson et al. [45]. Briefly, p-toluenesulphonic acid monohydrate (PTSA) was added to a tri-necked boiling flask equipped with an attached addition funnel. The vessels were placed under vacuum for 15 min before being purged with nitrogen. The boiling flask was charged with anhydrous acetonitrile and batch-specific amounts of MEE (x molar eq) and 1,4 butanedithiol (BDT) (1-x molar eq) where x = 1, 0.75, 0.5, 0.25, and 0 for the synthesized PTKs, respectively. The addition funnel was also charged with anhydrous acetonitrile and 2,2-dimethoxypropane (DMP) (0.83 molar eq). A molar excess of dithiol monomers was utilized relative to DMP to ensure the formation of polymers with free terminal thiols. Both the addition funnel and boiling flask's solutions were purged with flowing nitrogen for 30 min before submerging the boiling flask into an oil bath at 80°C. After 15 min of temperature equilibration, the addition funnel stopcock was set so that the acetonitrile-DMP solution was added drop-wise over a period of 16 h. Post synthesis, the acetonitrile was removed by rotary evaporation and the resultant PTKs were isolated by precipitation into cold ethanol and dried under vacuum. To evaluate polymer compositions, samples of the respective PTKs were dissolved in deuterated chloroform ($CDCl_3$) and analyzed with ^1H nuclear magnetic resonance spectroscopy (NMR, Bruker 400 MHz Spectrometer). ^1H NMR chemical shifts were reported as δ values in ppm relative to the deuterated $CDCl_3$ (δ = 7.26). Multiplicities are reported as follows: s (singlet), d (doublet), t (triplet), and m (multiplet). ^1H NMR (400 MHz, $CDCl_3$): δ = 3.67-3.61 (m, 4H), δ = 2.83 (t, 4H), δ = 2.63 (t, 4H), δ = 1.72 (t, 4H), δ = 1.60 (s, 6H).

Polyester polyol synthesis

Trifunctional or bifunctional polyester polyols were synthesized as previously documented [63]. To synthesize the trifunctional polyol, glycerol was vacuum dried for 48 h at 80^{o}C and then added to a 100 mL three neck flask. By molar amount, 60% ε-caprolactone, 30% glycolide, and 10% D,L-lactide were added to the glycerol starter along with a stannous octoate catalyst to yield a 900 g mol^{-1} triol, a 1000 g mol^{-1} diol, and a 1500 g mol^{-1} triol.

PTK hydroxyl functionalization

The hydroxyl-functionalization of the PTK dithiols was completed [225] in order to generate polyols compatible with standard polyurethane synthesis. Briefly, PTK dithiol polymers were transferred to a boiling flask, placed under vacuum, and then exposed to a nitrogen atmosphere. The flask was charged with anhydrous dichloromethane (DCM) before adding a 10x molar excess of β-mercaptoethanol to the solution. This solution was stirred continuously at room temperature to reduce any disulfide bonds and recover the reactive thiol end groups. After 3 h of stirring, the DCM was evaporated and the residue was washed three times in cold ethanol to remove residual β-mercaptoethanol. The reduced PTK polymers were dissolved in anhydrous tetrahydrofuran (THF) before adding a 10x molar excess of cesium carbonate ($CsCO_3$) under nitrogen and stirring for 30 min at room temperature. A 5x molar excess of 2-bromoethanol was next added to the solution and stirred for 18 h under nitrogen at room temperature. After stirring, the solution was added to a separation funnel with an excess of deionized water to effectively separate the PTK-solubilizing THF layer from the water-soluble $CsCO_3$ catalyst. The hydroxyl-functionalized PTKs were extracted in THF before removing the solvent by rotary evaporation, followed by precipitation three times in cold ethanol before vacuum drying for 24 h. Molecular weights and polydispersities of the five synthesized PTK diols were analyzed by gel permeation chromatography (GPC, Agilent Technologies, Santa Clara, CA). Polymer molecular weights were quantified using a calibration curve generated from poly(ethylene glycol) (PEG) standards (400 – 4000 g mol^{-1}). Hydroxyl-functionalization was confirmed by ^1H NMR (400 MHz, $CDCl_3$): δ = 2.74 (t, 4H) and attenuated total reflectance Fourier transform infrared spectroscopy (ATR-FTIR; Bruker Tensor 27 FTIR, Billerica, MA). For ATR-FTIR, thiol-terminated and hydroxyl-terminated PTK polymers were placed in contact with a ZnSe ATR crystal to quantify absorbance at 2550 cm^{-1} and 3400 cm^{-1}, which correspond to absorbance peaks of free thiol and free hydroxyl groups, respectively. The hydroxyl (OH) numbers of the different PTK diols were determined by titration (Metrohm 798 MPT Titrino, Herisan, Switzerland) according to ASTM E1899 – 08 [226], and this number was used to determine the OH number molecular weight of each polymer[83].

PTK-UR and PEUR synthesis

The PTK-UR and PEUR scaffolds were prepared using two-component reactive liquid molding of: (a) hexamethylene diisocyanate trimer (HDIt) or lysine triisocyanate (LTI), and (b) a hardener component comprising the PTK diol or polyester triol, water, TEGOAMIN33 catalyst, sulfated castor oil stabilizer, and calcium stearate pore opener [63]. The makeup of the hardener components for the different respective PTK diols was individually optimized to yield scaffolds with mechanical integrity and an intact porous structure. PEUR scaffolds were respectively designated by their polyester precursor as 900t-PEUR, 1000d-PEUR, and 1500t-PEUR and served as hydrolytically-degradable controls. The hardener component elements were first mixed for 30 s at 3300 rpm in a Hauschild DAC 150 FVZ-K SpeedMixer (FlackTek, Inc., Landrum, SC) before adding the HDIt and mixing for an additional 30 s. This reactive liquid mixture was allowed to rise freely for 10-20 min for complete setting and hardening. The targeted index (ratio of NCO to OH equivalents times 100) was 115, where the number of OH equivalents is calculated from the experimentally measured OH number for the relevant PTK diol.

Characterization of scaffold physical properties

The core densities of PTK-UR and PEUR scaffolds made with HDIt were determined by measuring the mass and volume of cylindrical porous scaffold core samples, with the core porosities being subsequently calculated from these density values [63]. The porous morphologies of the different PTK-UR scaffolds were qualitatively assessed by scanning electron microscopy (Hitachi S-4200 SEM, Finchampstead, UK). The amount of unreacted components (sol fraction) in the cross-linked network was measured from the mass loss of dried scaffold cylinders (25 mm × 12 mm) previously incubated in DCM for 24 h. To measure the molecular weight between crosslinks (M_c), scaffold samples (n = 3) were weighed dry and then incubated in DCM for 24 h. After incubation, samples were gently blotted to remove excess DCM and then the samples' swollen mass was measured. These values, along with the solvent parameters, were used in the Flory-Rhener equation to determine M_c. For measuring scaffold hydrophilicity, PTK-UR films of 100%, 50%, and 0% MEE-PTK diols were synthesized using an index of 105 and the gelling catalyst Coscat83 at

1000 ppm. After mixing the catalyst and PTK diol for 30 s at 3300 rpm, HDIt was added and mixed for an additional 30 s. The mixtures were cast into Teflon compression molds and allowed to cure for 18 h at 60°C. The contact angle of water on these PTK-UR films was measured using a Rame-Hart (Mountain Lakes, NJ) Model A-100 contact angle goniometer. A 4 μL water drop was added to the film surface, and after 10 min, an equilibrium contact angle was measured to account for molecular surface reorganization which increased the hydrophilicity at the contact site [227].

Thermal and mechanical properties

Thermal transitions were measured by a TA Instruments (New Castle, DE) Q200 DSC and Q800 DMA. For DSC analysis, samples ranging in mass from 10-15 mg were heated from -80° C to 200° C at a rate of 10° C min^{-1}, cooled to -80° C at a rate of -20° C min^{-1}, and heated a second time to 200° C at a rate of 10° C min^{-1}. All transitions were obtained from the second heating run. For dynamic mechanical analysis (DMA, Q800 DMA, TA Instruments, New Castle, DE), cylindrical samples (6 mm diameter × 6 mm height) were analyzed from -80° to 55° C at a ramp rate of 1° C min^{-1}. Scaffolds were compressed at a frequency of 1 Hz with 1% strain during the thermal treatment. Glass transitions were obtained at the peak of tan δ.

The mechanical properties of the different PTK-UR and PEUR scaffold formulations made with HDIt were measured in compression at 37°C in a submersion compression clamp using the Q800 DMA. Cylindrical 6 × 6 mm scaffolds were tested after incubation in phosphate buffered saline (PBS) for 7 days at 37°C. Using a preload force of 0.1 N, samples were compressed along the longitudinal axis at a strain rate of 10% per min until 60% compressive strain was achieved. The Young's modulus for each sample was calculated from the slope of the initial linear region of each respective stress-strain curve after toe-in.

In vitro degradation of PTK-UR and PEUR scaffolds made with HDIt

Long-term hydrolytic stability of PTK-UR and PEUR scaffolds made with HDIt was determined by incubating 10 mg samples in PBS at 37°C on a shaker and measuring the mass loss at each time point (n = 3). Before beginning the experiment, scaffolds were soaked in an excess of DCM for 24 h to remove any

unreacted components before vacuum drying for 24 h. Scaffold samples were removed from the buffer at each time point, rinsed in deionized water, vacuum dried for 48 h, and weighed. The buffer medium was not changed between time points. Short term oxidative degradation rates of PTK-UR scaffolds were similarly assessed using an oxidative degradation medium that simulates *in vivo* oxidative degradation at an accelerated rate [228, 229]. This oxidative medium comprised 20 wt% hydrogen peroxide (H_2O_2) in 0.1 M cobalt chloride ($CoCl_2$), with the H_2O_2 and cobalt ion reacting to stimulate oxidative radical formation [228]. As with the long-term study, triplicate samples were pre-soaked in DCM for 24 h before vacuum drying and incubated at 37°C in the oxidative medium on a shaker. At specified time points over 10 days, samples were removed, rinsed with deionized water, vacuum dried, and weighed. The oxidative medium was replaced every 3 days, and the morphology of both PBS-incubated and H_2O_2-incubated scaffolds was qualitatively assessed with SEM.

The effect of radical concentration on PTK-UR (HDIt) scaffold degradation kinetics was also explored. The original 20% H_2O_2 in 0.1 M $CoCl_2$ degradation medium was diluted ten and one hundred fold to yield a 2% H_2O_2 in 0.01 M $CoCl_2$ solution and a 0.2% H_2O_2 in 0.001 M $CoCl_2$ solution. These three degradation media were used to incubate 100%, 50%, and 0% MEE-PTK-UR scaffolds along with 900t-PEUR control samples, with material preparation steps and incubation conditions being the same as previously described.

Mathematical modeling of PTK-UR oxidative degradation

The degradation behavior of the PTK-UR scaffold formulations made with HDIt were fit to first-order decay kinetics equation to create a mathematical model of scaffold degradation with respect to H_2O_2 concentration. The first-order degradation model is given in Equation 1.

$$M_t/M_0 = e^{-kt}$$

Equation 1. First order mass loss model.

In this equation, M_t is the scaffold mass remaining at time t, M_0 is the initial scaffold mass, and k is the degradation rate constant. Non-linear regression was used to fit this first-order degradation model to the

experimentally determined degradation data. This method was used to determine the degradation rate constant *k* for the scaffolds incubated in the different media.

Degradation of PTK and PEUR scaffolds made with different isocyanate chemistries

Before beginning degradation experiments, 900t-PEUR and 100% MEE-PTK-UR scaffold samples made with either HDIt or LTI were soaked in an excess of DCM for 24 h to remove any unreacted components. Samples were dried under vacuum and pre-weighed before being placed in degradation media. Triplicate samples were incubated in accelerated hydrolytic conditions (phosphate buffered saline (PBS) at 77°C), high oxidative conditions (20 wt% hydrogen peroxide (H_2O_2) in 0.1 M cobalt chloride ($CoCl_2$) at 37°C), or low oxidative conditions (2 wt% H_2O_2 in 0.01 M $CoCl_2$ at 37°C). At specified time points, the samples were removed from the degradation media, rinsed with deionized water, vacuum dried, and weighed. The oxidative media were changed every three days.

Degradation of PTK-UR scaffolds in specific ROS

100% MEE-PTK-UR scaffolds were fabricated with LTI and weighed pre-degradation. Triplicate 5-10 mg scaffold samples were incubated at 37°C for three days in 1mL of either water, 5 mM hydrogen peroxide (H_2O_2), 5 mM H_2O_2 with 0.08 mM $CoCl_2$, (generates hydroxyl radicals)[228], 5 mM KO_2 (superoxide), or 5 mM 3-Morpholino-sydnonimine (SIN-1, generates peroxynitrite)[230]. The media was replaced once after 24hr. After three days of incubation, scaffolds were removed, rinsed with water, lyophilized, and then weighed to determine mass loss.

In vitro culture of macrophages on PTK-UR scaffolds

RAW 264.7 macrophages were cultured in DMEM supplemented with 10% FBS and 1% penicillin/streptomycin. 100% and 0% MEE-PTK-UR scaffolds made with HDIt were cut into 6.5 × 1-mm discs, sterilized by UV-radiation for 1 h (30 min per side), placed into 96-well plates, and incubated with culture medium for 30 min. Macrophages were seeded onto the scaffolds at a density of 2.5×10^5

cells/scaffold. The cells were allowed to adhere to the scaffolds for 3 h, at which point the media were removed and the cells were treated with either fresh culture media or activation media containing 5 μg mL^{-1} lipopolysaccharide (LPS) and 1000 U mL^{-1} interferon gamma (IFN-γ). Cells were incubated on the scaffolds for 3 days with fresh culture media being applied daily. After the 3-day incubation, the scaffolds were fixed in 5% glutaraldehyde for 2 h followed by 2% osmium tetroxide for 1 h. These fixed scaffolds were dehydrated in ascending grades of ethanol before being vacuum dried, sputter-coated, and imaged with SEM to evaluate surface pitting.

Cytotoxicity of PTK-UR and PEUR scaffolds

NIH 3T3 mouse fibroblasts stably transfected with a firefly luciferase reporter gene were cultured in DMEM supplemented with 10% FBS and 1% penicillin/streptomycin. 100% MEE-PTK-UR, 0% MEE-PTK-UR, and 900t-PEUR scaffolds made with HDIt were cut into 6.5 × 1-mm discs, sterilized by UV-radiation for 1 h (30 min per side), placed into a black-walled 96-well plate, and incubated with culture medium for 30 min. Fibroblasts were seeded at a density of 5.0×10^4 cells/scaffold on n=3 scaffolds and allowed to grow for 0, 1, and 3 days in 200 μL of culture media per well (changed every two days). At the endpoint, the cell-seeded scaffolds were treated with culture media containing a luciferin substrate. After 10 min, the scaffolds were imaged with an IVIS 200 (Xenogen, Alameda, CA) bioluminescence imaging system with an exposure time of 2 min to quantify the luciferase-based bioluminescence signal from each scaffold's viable cell population. All readings were normalized to day 0 bioluminescence values.

3.3 Results

PTK polymer synthesis and characterization

Thiol-terminated PTK polymers were successfully synthesized from the condensation polymerization of MEE, BDT, and DMP monomers using PTSA as a catalyst (Figure 7A). Five copolymers were synthesized with varying percent molar composition of MEE and BDT, and each polymer is designated by its relative mol% MEE. ^{1}H-NMR spectra confirmed that the composition of the synthesized polymers

closely matched the monomer ratios in the feed (Figure 7B, Table 1), and gel permeation chromatography (GPC) analysis showed that the polymers had M_n values of around 1000 g mol^{-1} with polydispersity index (PDI) values near 1.35 (Figure A1, Table 1).

Efficient conversion of terminal thiols to hydroxyls was demonstrated by ATR-FTIR. The thiol absorbance peak at 2550 cm^{-1} was apparent in the thiol-terminated, parent PTKs but did not appear with the hydroxyl-terminated polymers, which generated a characteristic ATR-FTIR hydroxyl peak at 3400 cm^{-1} (Figure 7C). OH numbers experimentally measured with titration were utilized to calculate a titration M_n (Table 1) that was used to balance the hydroxyl-isocyanate reaction used to form PTK-URs. Consistent with previous findings, the experimental OH numbers trended higher than theoretical values [75].

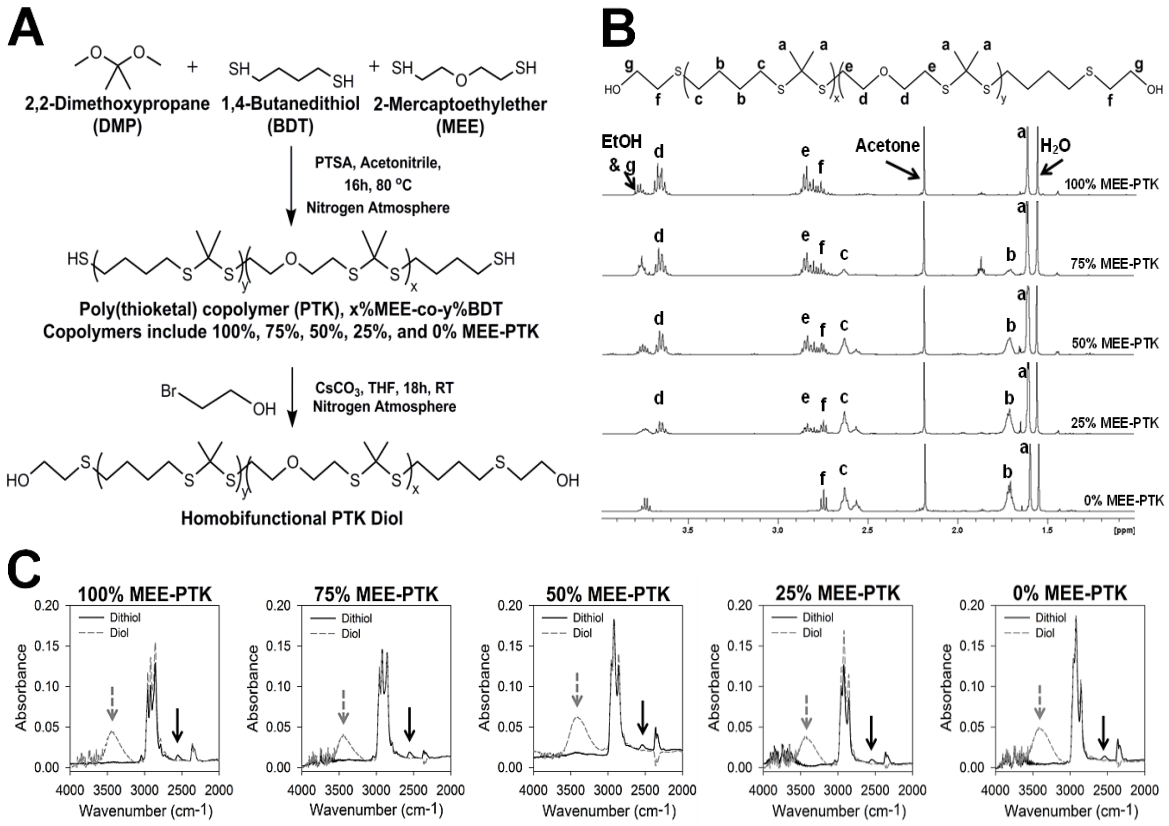

Figure 7. Synthesis and characterization of a family of PTK diols. (A) Scheme for the condensation polymerization of thiol-terminated PTKs and their conversion into PTK diols. (B) ^{1}H-NMR spectra of the PTK copolymer diols. Peaks associated with MEE and BDT monomers closely matched the molar composition used in the polymer feed. (C) ATR-FTIR spectra of thiol- and hydroxyl-terminated PTKs. The thiol absorbance peak is seen at 2550 cm^{-1} (black arrow) and the hydroxyl absorbance peak is seen at 3400 cm^{-1} (grey arrow). These spectra demonstrate efficient conversion of PTK terminal thiols into hydroxyls.

PTK-UR scaffold formation and physical properties

PTK-UR scaffolds were successfully synthesized from the PTK diols and HDIt, yielding porous, mechanically robust 3D scaffolds (SEM images shown in Figure A2). PEUR control scaffolds were also successfully formed from HDIt and the three different polyester prepolymers (1000d, 1500t, and 900t). The resulting PTK-UR and PEUR scaffolds possessed similar sol fraction and porosity, as seen in Table 2. The average molecular weight between crosslinks (M_c) for 1000d- and 1500t-PEUR was statistically equal to all of the PTK-UR scaffolds, while the 900t-PEURs had a significantly lower M_c ($p < 0.05$) relative to all other formulations except for the 100% and 0% MEE-PTK-UR scaffolds (Table 2). The relative surface hydrophilicity of the PTK-UR materials was assessed using contact angle measurements on films, with 100%, 50%, and 0% MEE-PTK-URs having contact angle values of 66°, 77°, and 80°, respectively. PTK-UR and PEUR scaffolds were also formed with lysine triisocyanate (LTI), and the structures of both HDIt and LTI tri-functional isocyanate molecules is give in Figure 8.

Table 1. Characterization of PTK diols.

Copolymer (PTK diol)	*Feed MEE%*	*Actual MEE%*[a]	*GPC M_n*[b]	*PDI*[b]	*Titration M_n*[c]
100% MEE-PTK	100%	100%	1027	1.38	825
75% MEE-PTK	75%	76%	1005	1.34	850
50% MEE-PTK	50%	52%	947	1.35	810
25% MEE-PTK	25%	26%	1053	1.36	745
0% MEE-PTK	0%	0%	807	1.32	680

[a]Calculated from NMR peaks at δ=1.72 and δ=3.64 ppm.

[b]Calculated from GPC standards.

[c]Calculated from measured titration OH numbers.

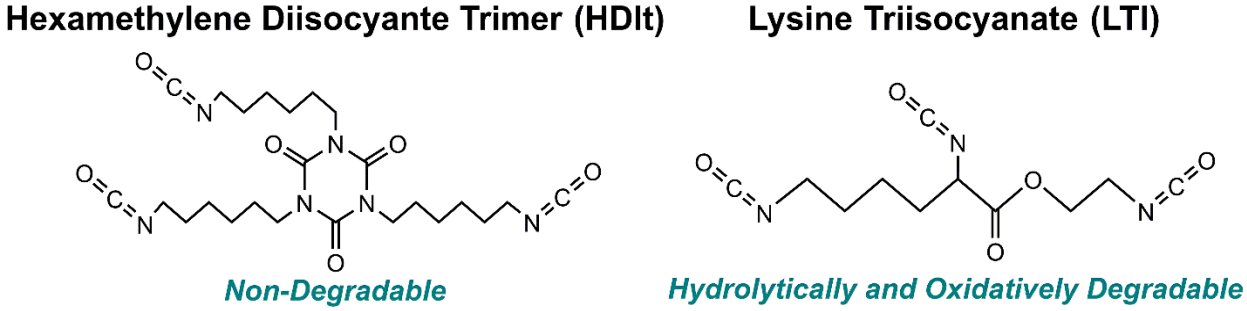

Figure 8. Tri-functional isocyanates used in the formation of PTK-UR and PEUR polyurethane scaffolds.

Thermal and mechanical analysis of PTK-UR scaffolds

The glass-transition temperature (T_g) of PTK polyols was determined by differential scanning calorimetry (DSC), and the T_g of the PTK-UR scaffolds made with HDIt was measured by DSC and dynamic mechanical analysis (DMA) (Table A1). The wet compressive moduli of the PTK-UR scaffolds ranged from 100 - 250 kPa, and the PEUR moduli ranged from 20 – 100 kPa (Figure 9). All the PTK-UR formulations had significantly higher modulus values than the 1500t-PEUR and 1000d-PEUR materials, while the lower M_c 900t-PEUR scaffolds possessed stiffness values closer to the PTK-UR samples. However, even this more tightly crosslinked formulation was significantly less stiff than the 100% and 0% MEE-PTK-UR materials.

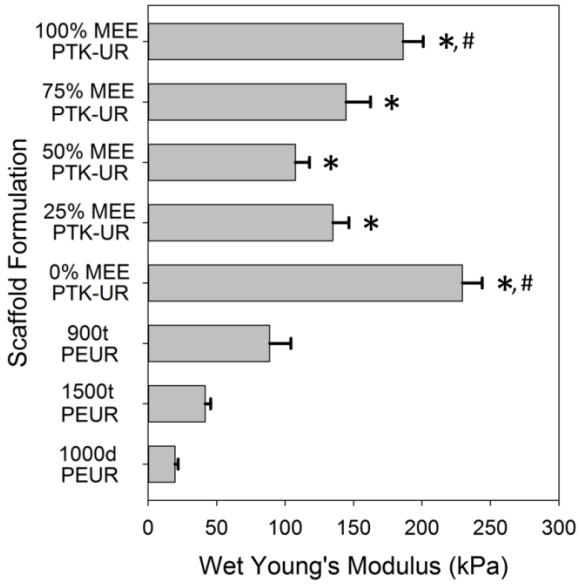

Figure 9. PTK-UR and PEUR scaffold mechanical properties. The compressive moduli of porous scaffolds were determined under aqueous conditions at 37°C. *$p < 0.05$ compared to 1500t- and 1000d-PEUR. $^{\#}p < 0.05$ compared to 900t-PEUR.

In vitro degradation of PTK-UR scaffolds under aqueous and oxidative conditions

The hypothesized oxidative degradation mechanism of PTK copolymers is seen in Figure A3. Qualitative degradation of PTK-UR scaffolds made with HDIt was demonstrated by SEM as scaffolds incubated for 10 days in oxidative media illustrated loss of porous architecture and surface pitting, while these morphological changes in scaffold architecture were not apparent following PTK-UR scaffold incubation in PBS for 25 weeks (Figure 10 and A2). The PTK-UR scaffolds were stable over a long-term,

25-week study in PBS at 37°C, while the 900t-PEUR scaffolds underwent significant hydrolytic degradation over this time period (Figure 11A). Conversely, the PTK-URs rapidly degraded under accelerated oxidative conditions (20% H_2O_2 in 0.1 M $CoCl_2$) as seen in Figure 11B. The comprehensive temporal degradation data for all PTK-URs tested in the 20% H_2O_2 media are displayed in Figure A4.

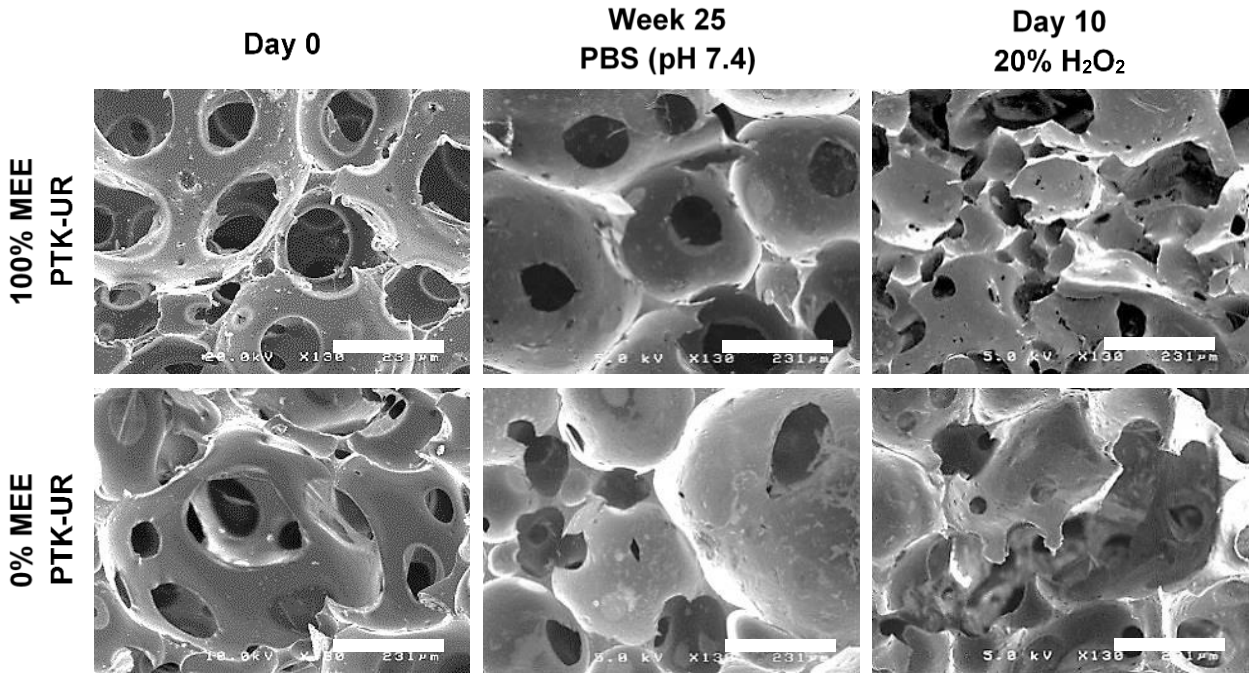

Figure 10. Representative SEM images of *in vitro* PTK-UR degradation. Freshly made scaffolds (left column), scaffolds incubated in PBS for 25 weeks (middle column), and scaffolds incubated in 20% H_2O_2 media for 10 days (right column). Scale bars = 231 μm. The ROS-degraded PTK-URs feature more irregular pore morphology and surface pitting while PBS-incubated scaffolds appear unchanged relative to freshly made scaffolds.

Mathematical model of ROS-dependent PTK-UR scaffold degradation

To further elucidate the relationship between ROS concentration and the degradation rates of the different PTK-UR scaffold formulations made with HDIt, degradation was measured in oxidative media comprising 20%, 2%, and 0.2% H_2O_2 and 0.1, 0.01, and 0.001 M $CoCl_2$, respectively. The degradation rates of PTK-UR scaffolds made with HDIt were dependent on the concentration of H_2O_2 (Figure 11C-F). The mass loss profiles of the PTK-UR scaffolds were fit to first-order degradation kinetics (Equation 1) to mathematically model the process of scaffold degradation with respect to H_2O_2 concentration. The model-generated degradation profiles are concurrently shown with the respective experimental data as dotted lines

in Figure 11B-E, with the derived degradation rate constants being shown in Figure 11F. The 900t-PEUR samples incubated in these same oxidative media did not display significant degradation over the same timeframe (Figure 11F and Figure A5).

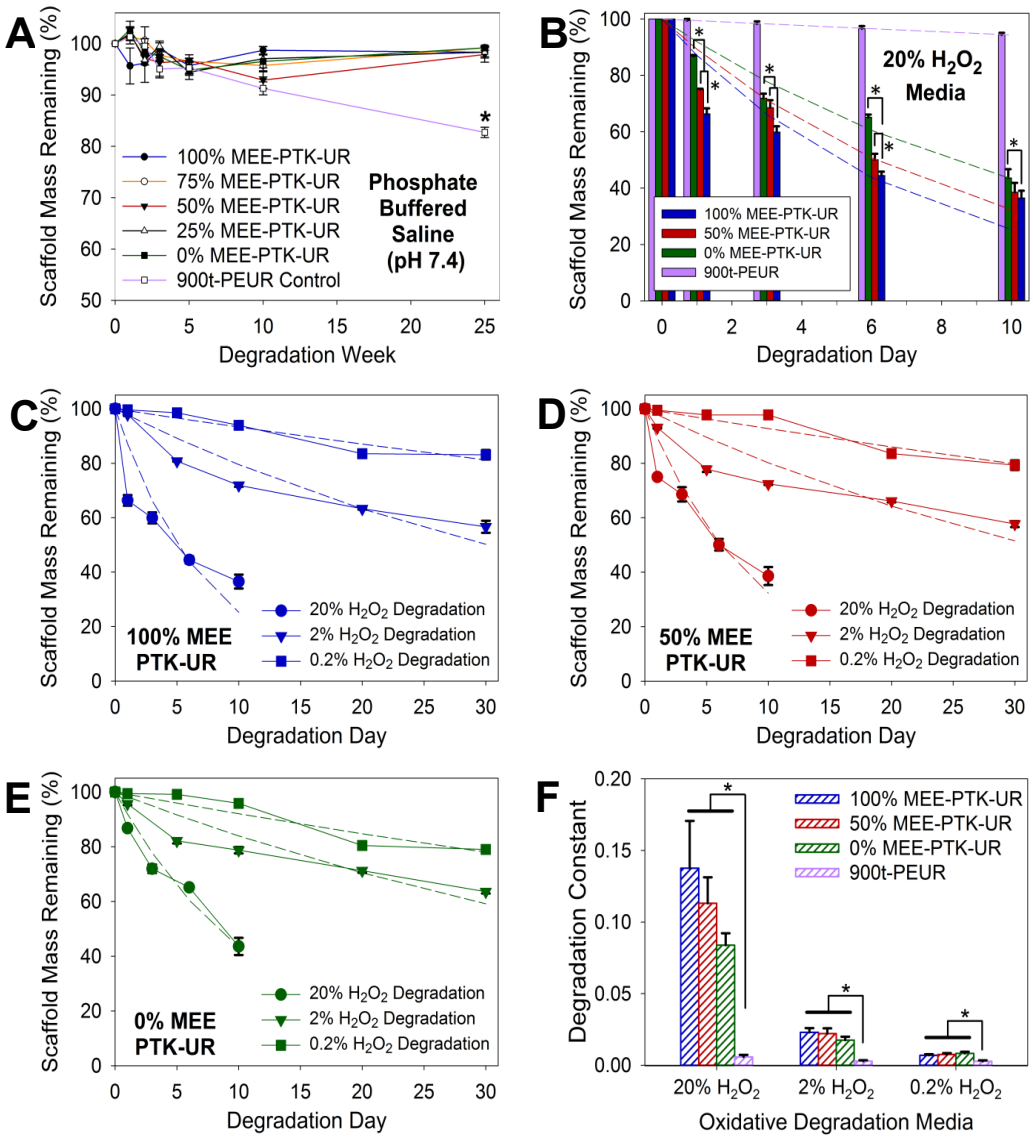

Figure 11. *In vitro* degradation kinetics of PTK-UR scaffolds. Data are presented as mean ± standard error with n = 3. (A) Long-term stability of PTK-UR scaffolds incubated in PBS. (B) Percent degradation of PTK-UR scaffolds incubated in oxidative medium (20% H_2O_2 in 0.1M $CoCl_2$) as a function of PTK composition. Dashed lines represent model-generated curves for first-order degradation kinetics, *$p < 0.05$. Percent mass remaining of (C) 100% MEE-PTK-UR, (D) 50% MEE-PTK-UR, and (E) 0% MEE-PTK-UR scaffolds incubated in oxidative media containing 20%, 2%, and 0.2% H_2O_2. (F) Degradation constants used to generate the best-fit curves in (B-E), as determined by non-linear regression analysis. The PTK-UR but not the PEUR scaffolds exhibited H_2O_2 dose-dependent degradation.

Effect of isocyanate chemistry on PTK-UR and PEUR scaffold degradation

100% MEE-PTK-UR and 900t-PEUR scaffolds made with either HDIt or LTI were incubated in accelerated hydrolytic conditions (PBS at 77°C), high oxidative conditions (20 wt% H_2O_2 in 0.1 M $CoCl_2$ at 37°C), or low oxidative conditions (2 wt% H_2O_2 in 0.01 M $CoCl_2$ at 37°C). PTK-UR scaffolds made with either isocyanate experienced dose-dependent degradation with respect to ROS concentrations (Figure 12A-B), though LTI-based materials degraded significantly faster than HDIt scaffolds. PEUR scaffolds with HDIt were relatively inert to oxidation at either ROS concentration, while PEURs with LTI underwent significant degradation in 20 wt% H_2O_2. Both PTK-UR and PEUR materials made with LTI degraded significantly faster than analogous scaffolds made with HDIt, while PEUR scaffolds were sensitive to hydrolysis with both isocyanate chemistries as seen in Figure 12C. PTK-UR scaffolds with HDIt were completely inert to hydrolysis.

Table 2. Physical properties of PTK-UR and PEUR scaffolds.

Scaffold	Sol Fraction (%)	Core Porosity (vol. %)	M_c (kg mol^{-1})
100% MEE PTK-UR	6.9%±1.6%	90.9%±0.4%	7.6±4.2
75% MEE PTK-UR	8.4%±1.4%	89.0%±1.2%	10.1±4.9
50% MEE PTK-UR	9.7%±6.1%	86.9%±1.4%	13.8±6.5
25% MEE PTK-UR	9.1%±2.7%	90.6%±1.5%	9.0±5.0
0% MEE PTK-UR	8.3%±3.2%	88.8%±1.4%	9.0±5.8
900t PEUR	4.1%±1.6%	89.8%±1.2%	2.5±1.6
1500t PEUR	4.7%±0.1%	91.3%±0.2%	13.2±5.4
1000d PEUR	7.7%±0.1%	92.7%±0.7%	7.7±2.8

*All values presented as mean ± standard deviation

PTK-UR degradation in response to different ROS

100% MEE-PTK-UR scaffolds made with LTI were incubated in media containing either water, H_2O_2, H_2O_2 with hydroxyl radicals, superoxide, or peroxynitrite to test the degradative capacity of each specific ROS with respect to PTK-UR materials as seen in Figure A6. There was virtually no degradation of the scaffold samples in water, while H_2O_2 with hydroxyl radicals produced the most degradation. Samples

incubated in solely superoxide or H_2O_2 underwent slightly less degradation, while scaffolds in peroxynitrite underwent the least degradation.

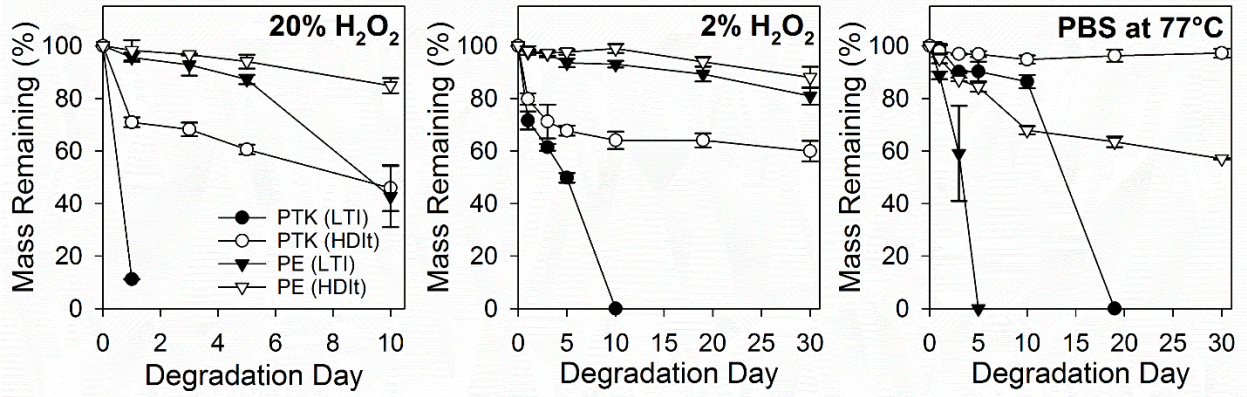

Figure 12. *In vitro* degradation kinetics of PTK-UR and PEUR scaffolds made with either LTI or HDIt isocyanate chemistries. PTK-UR scaffolds made with both LTI and HDIt were sensitive to ROS when incubated in (A) 20% H_2O_2 in 0.1M $CoCl_2$ or (B) 2% H_2O_2 in 0.01M $CoCl_2$, though LTI-based samples were degraded faster than HDIt scaffolds. PEUR (LTI) scaffolds were also more degraded at the high ROS dose than PEUR (HDIt) samples. However, PTK-UR (HDIt) samples were (C) hydrolytically inert while LTI-based scaffolds were sensitive to hydrolysis. PEUR scaffolds with either isocyanate chemistry were degraded by hydrolysis.

In vitro cell-mediated degradation and cytocompatibility of PTK-UR scaffolds

100% and 0% MEE-PTK-UR scaffolds made with HDIt were seeded with murine-derived RAW 267.4 macrophages. Seeded cells were treated with either control culture media or macrophage-activating media containing LPS and IFN-γ. Qualitative SEM imaging of scaffolds after 3 days illustrated potential surface pitting by activated macrophages, but cell-mediated scaffold degradation was not as apparent for the scaffolds seeded with non-activated cells (Figure A7A). NIH 3T3 mouse fibroblasts stably transduced to express luciferase were also seeded onto 100% MEE-PTK-UR, 0% MEE-PTK-UR, and 900t-PEUR scaffolds made with HDIt, and relative cell number was measured based on luciferase activity over 3 days of culture (Figure A7B). Cell-generated bioluminescent signal was constant over the culture period, and there were no significant differences between the scaffold compositions tested.

3.4 Discussion

Most currently utilized tissue engineering scaffolds feature hydrolytically degradable ester bonds that nonspecifically degrade in the presence of water. Cleavage of ester bonds produces free carboxylic acids

which can acidify the local microenvironment and cause autocatalytic degradation [72], with this accelerated scaffold breakdown leading to reduced tissue regeneration [36]. Here, a PTK-based scaffold technology is presented that is specifically degraded by cell-generated ROS while remaining insensitive to hydrolysis (Figure 11A) [45]. Because these PTK-UR materials selectively degrade by cell-mediated activity, they avoid autocatalytic degradation and are anticipated to yield better matched rates of cellular infiltration and scaffold degradation. To this end, PTK copolymers were successfully synthesized with varying chain compositions but similar M_n and PDI values (Figure 7, Table 1). The M_n and PDI values observed here are both lower than for PTK polymers reported by Wilson et al. In this previous study, the authors utilized an excess of the DMP monomer with respect to the dithiol monomers to achieve a higher degree of polymerization [45]. In the current work, an excess of the dithiol monomer was used to ensure that the resulting polymers possessed telechelic dithiol chain ends that could be subsequently converted to hydroxyls and utilized for polyurethane formation. This modification potentially limited the step-wise growth of the PTK chain, leading to lower M_n. As part of the polymer purification in the current studies, the PTK polymers were washed with ethanol which presumably preferentially removed both unreacted monomer and lower molecular weight PTKs, leading to isolation of a larger molecular weight population of PTKs with lower polydispersity relative to the crude product. The resulting dithiol-terminated MEE-PTK polymers were converted into diols to generate telechelic end groups compatible with standard polyurethane synthesis and to provide PTK polyols amenable to direct comparison with polyesters used in PEUR scaffold formation.

The PTK-UR scaffolds were fabricated using HDIt and compared to PEUR scaffolds made from 900t, 1000d, and 1500t polyester-based PEUR scaffolds. The 900t-PEUR represented a biological control that has been successfully used for *in vivo* applications [76, 79, 83] while the 1000d-PEUR and 1500t-PEUR were synthesized for a more direct material comparison to the PTK-URs because they yield PEUR scaffolds with crosslink densities that are more similar to the PTK-UR scaffolds. The PTK-UR scaffolds produced from the PTK macrodiols were approximately 90% porous and were morphologically similar to more conventional PEUR 3D porous scaffolds. This level of porosity is optimal for promoting cellular in-growth,

nutrient exchange, and neo-vascularization in tissue engineering applications [231-233]. The PTK-URs also featured relatively low sol fraction values, indicating that the isocyanates and diols were well matched and efficiently reacted during scaffold formation. As expected, the scaffolds' relative hydrophilicity was influenced by the composition of the PTK polyol, and the contact angle was inversely correlated with the mol% of the more hydrophilic MEE monomer in the PTK copolymer. These data suggest that the 100% MEE-PTK-UR with a contact angle of 66° may be optimal for cellular adhesion and tissue formation *in vivo*, since more hydrophobic surfaces with contact angles > 76° (such as the 50% and 0% MEE-PTK-UR formulations) preferentially adsorb hydrophobic serum proteins such as albumin over cellular adhesion proteins like fibronectin and vitronectin [234, 235].

Thermal analysis of PTK-UR and PEUR scaffolds, along with their polymeric precursors, indicated that the scaffolds are phase-mixed materials since the 3D materials all possessed a T_g exceeding that of the polyol precursor soft segment [75]. The scaffold T_g values determined by DMA also exceeded those measured by DSC by 30 – 50°C, as has been previously reported for similar 3D PEUR materials [63]. Wet compression testing of these materials indicated that although the 1500t-PEUR, 1000d-PEUR, and PTK-UR scaffolds had similar M_c values (Table 2), all of the PTK-UR formulations had significantly higher modulus values than the 1500t-PEUR and 1000d-PEUR materials (Figure 9). However, there was no consistent trend between PTK-UR scaffold composition and modulus. Due to its higher crosslink density, the 900t-PEUR achieved stiffness values closer to the PTK-UR samples, though even this formulation was significantly less stiff than the 100% and 0% MEE-PTK-UR materials.

Previous work has demonstrated the selective, ROS-mediated degradation of poly(thioketal) nanoparticles [45]. The PTK-UR scaffolds were formulated with HDIt because it is more oxidatively stable relative to lysine-derived isocyanates [74, 76, 79], allowing more specific study of the degradation behavior of the polyol component. Degradation of PTK-UR and 900t-PEUR scaffolds was tested in an oxidative degradation medium comprising H_2O_2 and $CoCl_2$ that produces hydroxyl radicals [228]. These radicals destabilize the thioketal bond, leading to chain scission and breakdown into the original constitutive monomers (MEE and BDT) and acetone (Figure A3). It is predicted that these small byproducts would be

rapidly cleared and would not cause cytotoxicity in an *in vivo* environment. This is supported by previous work showing that when incorporated into a similar polyurethane system, MEE monomers cause limited *in vitro* cytotoxicity [236] and a minimal host inflammatory response *in vivo* [237].

The long-term stability of PTK-UR scaffolds made with HDIt over 25 weeks in PBS (Figure 11A) was significantly different than these materials' behavior under accelerated oxidative conditions as seen in Figure 11B, highlighting the ROS-specific degradation mechanism of the PTK-UR scaffolds. Furthermore, there was a relationship between the PTK composition and degradation rate, as the scaffolds with higher MEE content in the PTK polyol degraded faster (Figure 11B). It has been previously reported that ethers are stable in aqueous media but that oxidative radicals can degrade them *in vitro* and *in vivo* [228]. Thus, it is hypothesized that the faster ROS-dependent degradation seen in both the 100% and 50% MEE-PTK-UR materials may result from a combination of oxidative degradation of both thioketals and ethers, while the 0% MEE-PTK-UR scaffolds are degraded solely by thioketal scission. These results indicate that ROS-dependent scaffold degradation rates can be tuned by the composition of the PTK polyol.

For all PTK-UR compositions tested, the degradation rate was dependent on ROS concentrations (Figure 11C-E). This dose-dependent relationship between ROS levels and degradation rate coupled with the agreement between the model and experimental data confirm that the PTK-UR scaffolds degrade by first-order kinetics with respect to ROS concentration. The degradation rate constants derived from the non-linear regression fitting of the experimental data gathered in 20% H_2O_2 media (Figure 11F) also illustrate the relationship between degradation rate and the %MEE-PTK polyol used in PTK-UR scaffold fabrication, though this trend was decreased under lower H_2O_2 concentrations. In contrast, the 900t-PEUR samples incubated in these same oxidative media did not display H_2O_2 dose-dependent degradation (Figure 11F and A4), highlighting the unique degradation mechanism of the PTK-UR relative to PEUR scaffolds. These collective data confirm that PTK-based polyols are selectively cleaved by ROS and that their rate of degradation is first-order with respect to the concentration of radical species in the local environment.

The effect of isocyanate chemistry and specific ROS on scaffold degradation was also explored. PTK-UR and PEUR scaffolds made with either HDIt or LTI were incubated in varying doses of ROS or in

accelerated hydrolytic conditions. Confirming results seen in previous work[76], both PTK-UR and PEUR samples made with LTI were more sensitive to both oxidation and hydrolysis compared to HDIt scaffolds (Figure 12). However, PTK-UR scaffolds were significantly more degraded than PEURs in oxidative conditions and were inert to hydrolysis when fabricated with the non-degradable HDIt, while PEURs were hydrolytically degradable with both isocyanate chemistries as expected. These results indicate that the inclusion of LTI in scaffold formulations greatly increases the degradability of these materials compared to HDIt, presenting another pathway for tuning the degradation kinetics of these scaffolds. The sensitivity of PTK-UR scaffolds to specific ROS was also explored as previous work has shown differential degradation patterns in thioketal-containing materials exposed to different ROS[177]. Similar to previous results, PTK-UR scaffolds underwent the most degradation when exposed to hydroxyl radicals but less degradation when exposed to H_2O_2 or superoxide (Figure A6). This data also demonstrated that thioketal bonds are sensitive to peroxynitrite, a particularly cytotoxic radical species[238], that had not been previously explored as a degrading agent of PTK materials. In all, these degradation data demonstrate the strong effect scaffold chemical composition and different reactive species have on material degradation kinetics.

PTK-UR scaffolds made with HDIt were shown to display low levels of *in vitro* cytotoxicity with both RAW 267.4 macrophages and NIH 3T3 fibroblasts. Seeded macrophages were treated with either control culture media or media containing LPS and IFN-γ to activate the macrophages through the classical pathway [239, 240], which is known to lead to ROS production [76, 187]. Scaffolds with activated macrophages displayed low levels of surface pitting while cell-mediated remodeling of the scaffold surface was less evident for the control cells (Figure A7A), potentially indicating that the PTK-UR scaffolds were degraded by physiologically relevant concentrations of ROS. Further highlighting these materials' limited cytotoxicity, luciferase-expressing fibroblasts seeded on PTK-UR and PEUR scaffolds steadily maintained their bioluminescent signal over the culture period (Figure A7B), similar to cell growth profiles seen in other non-cytotoxic 3D scaffolds [241, 242]. Furthermore, none of the scaffold formulations displayed a significant difference in bioluminescence over time or relative to each other, indicating that PTK-UR

scaffolds had cytotoxicity profiles similar to analogous PEUR scaffolds that have been successfully utilized *in vivo* [76].

3.5 Conclusion

ROS are key mediators of cell function in both health and disease, especially at sites of inflammation and tissue healing. Utilizing these cell-generated species as triggers for selective polymer degradation represents a promising methodology for creating tissue engineering scaffolds with well-matched rates of tissue in-growth and cell-mediated scaffold degradation. Here, poly(thioketal) polymers featuring tunable chain compositions and ROS-mediated degradation rates have been developed towards this end. These PTK polymers were successfully incorporated into 3D porous tissue engineering scaffolds, generating materials with more robust mechanical properties than similar constructs fabricated from standard polyesters. These PTK-UR scaffolds made with HDIt were selectively degraded by ROS but were stable under aqueous conditions, highlighting the specificity of this degradation mechanism. To this end, the *in vitro* oxidative degradation rates of the HDIt-containing PTK-URs followed first-order degradation kinetics and displayed dose-dependent degradation with respect to ROS concentration. The effect of the isocyanate chemistry on scaffold degradation was also determined, as LTI-based materials degraded faster under oxidative conditions than HDIt scaffolds, further expanding the tunability options of these materials. PTK-UR scaffolds also displayed evidence of cell-mediated degradation by activated, ROS-producing macrophages. Finally, PTK-UR materials had cytotoxicity levels similar to analogous PEUR scaffolds, demonstrating the biocompatibility and therapeutic *in vivo* potential of these novel scaffolds. In all, these data provide an effective *in vitro* characterization of PTK-UR scaffolds in comparison to benchmark PEUR biomaterials and support the implementation of novel PTK-URs in *in vivo* studies.

CHAPTER 4

Local Delivery of siRNA from PTK-UR Scaffolds to Promote Diabetic Wound Healing

Text partially adapted from:

Martin JR, Gupta MK, Page JM, Yu F, Davidson JM, Guelcher SA, Duvall CL. A porous tissue engineering scaffold selectively degraded by cell-generated reactive oxygen species. Biomaterials. 2014; 35: 12, 3766-3776.

Martin JR, Nelson CE, Gupta MK, Yu F, Sarett SM, Hocking KM, Pollins AC, Nanney LB, Davidson JM, Guelcher SA, Duvall CL. Local delivery of PHD2 siRNA from ROS-degradable scaffolds to promote diabetic wound healing. Advanced Healthcare Materials. 2016; DOI 10.1002/adhm.201600820

4.1 Introduction

Diabetes mellitus affects 9.3% of the US population and is increasing in prevalence[3], with a doubling of incidence in the US from 1980-2012[2]. Diabetic patients are more prone to peripheral arterial disease and impaired wound healing, often exacerbating simple skin wounds towards chronic ulceration and in the worst cases, limb amputation. Approximately 25% of diabetics develop chronic ulcers[1], and roughly 60% of non-traumatic lower-limb amputations for patients over 20 years old occur in diabetics[3]. Impaired wound healing in diabetic patients is attributable to multiple factors[243], but is especially affected by deterioration in the microvasculature and subsequent development of ischemia[4]. In normal wound healing, injury-associated hypoxia activates the transcription factor hypoxia-inducible factor-1α (HIF-1α), which is primarily regulated by prolyl hydroxylase domain protein 2 (PHD2). PHD2 actively triggers HIF-1α degradation under normoxia[14, 15] but is inactive under hypoxia, thereby stabilizing HIF-1α. Stabilized HIF-1α dimerizes with HIF-1β to promote expression of multiple reparative genes, including vascular endothelial growth factor (VEGF)[11], angiopoietin-1 (ANG-1)[12], stromal cell-derived factor-1 (SDF-1)[13], and others that induce cell proliferation/recruitment and angiogenesis. Despite the presence of ischemia, HIF-1α is destabilized in diabetic wounds of both rodents[20] and human patients[9]. While inhibition of PHD2 through small molecule drugs has shown promise in re-establishing HIF-1α activity and healing skin wounds[20-23], these compounds also inhibit other PHD isoforms (PHD1 and PHD3) and can

result in off-target effects[24-26, 244]. In particular, concurrent inhibition of PHD1 and PHD3 has been shown to increase accumulation of HIF-2α[245]; conversely to HIF-1α, increased HIF-2α may impede wound closure and increase infection[246], further motivating specific reduction of PHD2 activity rather than pan-inhibition of PHDs.

Small interfering RNA (siRNA) holds great potential as a therapeutic due to its precise mode of action (complementary base-pairing and degradation of specific messenger RNA sequences) and ability to effectively silence targeted gene expression[247]. However, the *in vivo* efficacy of siRNA has been limited by substantial delivery barriers, including degradation by endogenous nucleases, inability to access the cytoplasm, and insufficiently sustained bioactivity in the target tissue[211, 212]. Much recent work has focused on the development of nanoparticle carriers that can shield siRNA from degradation[248, 249] while facilitating intracellular payload delivery[130, 250]. Furthermore, local delivery of siRNA avoids many of the challenges associated with systemic administration and helps to ensure that a sufficient siRNA dose reaches the target tissue while lessening the potential for side effects due to off-target gene silencing in healthy tissues[49, 251]. To date, local siRNA delivery strategies for wound healing applications have targeted matrix metalloproteinase-9 (MMP-9)[207], connective tissue growth factor (CTGF)[208], p53[209], and PHD2[27, 29] using a host of biomaterial delivery depots, including layer-by-layer coatings on non-degradable bandages, alginate hydrogels, and acellular dermal matrix. Here we sought to expand our ongoing work to develop cell-degradable synthetic scaffolds that promote robust cellular infiltration and tissue regeneration and that can be also used for sustained, local drug or nanomedicine release.

The available chemistries used for fabrication of synthetic scaffolds offer the opportunity to produce templates for guiding new tissue growth in critically-sized defects with adjustable biodegradation mechanisms and rates; moreover, these materials can serve as a depot for delivering a diversity of therapeutic molecules including growth factors[78, 252], small molecule drugs[23, 84], or nanoparticles[85]. In order to leverage these scaffold properties, we have recently developed strategies for delivering siRNA-carrying nanoparticles (siNPs) from hydrolytically-biodegradable poly(ester urethane) (PEUR) tissue engineering scaffolds[85] and demonstrated *in vivo* knockdown of PHD2 with increased

local angiogenesis in a subcutaneous mouse wound model[28]. Herein, we have applied this system in a more clinically-relevant diabetic rat skin excisional wound model. In addition, we have for the first time explored siNP delivery from a new poly(thioketal urethane) (PTK-UR) scaffold chemistry that features a cell-mediated (i.e. not hydrolytic) degradation mechanism driven by reactive oxygen species (ROS)[45]. Relative to ester-based PEUR materials, the PTK-UR chemistry enables better matched rates of degradation and cell infiltration while more effectively inhibiting wound contraction[30]. Here, we pursued PTK-UR scaffolds to locally deliver siNPs for the *in vivo* knockdown of PHD2 to promote angiogenesis, cell proliferation, and an increased rate of new tissue formation within diabetic excisional skin wounds.

4.2 Materials and methods

Materials

All chemical reagents were obtained from Sigma-Aldrich (Milwaukee, WI) unless otherwise indicated. 2-mercaptoethyl ether (MEE) was purchased from Tokyo Chemical Industry Co (Tokyo, Japan). Glycolide and D,L-lactide were obtained from Polysciences (Warrington, PA). Lysine triisocyanate (LTI) was obtained from Kyowa Hakko USA (New York, NY). Hexamethylene diisocyanate trimer (HDIt, Desmodur N3300A) was received as a gift from Bayer Material Science (Pittsburgh, PA). The tertiary amine catalyst (TEGOAMIN33), composed of 33 wt% triethylene diamine in dipropylene glycol, was obtained from Goldschmidt (Hopewell, VA). Tegaderm was obtained from 3M (St. Paul, MN) and the hydrogel dressing was obtained from ReliaMed (Fort Worth, TX). Lipofectamine 2000 was obtained from Life Technologies (Grand Island, NY), and all cell culture reagents, including Dulbecco's Modified Eagle Medium (DMEM), fetal bovine serum (FBS), and penicillin/streptomycin were supplied by Gibco Cell Culture (Carlsbad, CA). Dicer substrate siRNAs were obtained from Integrated DNA technologies (IDT, Coralville, IA).

siNP Synthesis and Characterization

A diblock copolymer composed of 2-(dimethylamino) ethyl methacrylate (DMAEMA), 2-propylacrylic acid (PAA), and butyl methacrylate (BMA) was synthesized by reversible addition-

fragmentation chain transfer (RAFT) polymerization as previously described[85, 130]. The final polymer, DMAEMA-*block*-(DMAEMA-*co*-BMA *co*-PAA), was characterized by gel permeation chromatography (GPC, Agilent Technologies, Santa Clara, CA) with an inline Wyatt mini-DAWNTREOS light scattering detector (Wyatt Technology Corp., Santa Barabara, CA) and ^{1}H nuclear magnetic resonance spectroscopy (NMR, Bruker 400 MHz Spectrometer) for molecular weight, polydispersity, and polymer composition. For the formation of NPs, the polymer was dissolved in a minimal volume of ethanol in a 2 mL RNAse free polypropylene tube followed by slow addition of deionized water to trigger spontaneous micelle formation (final polymer concentration 1 mg in 1 mL). Micellar size and polydispersity was characterized by Dynamic Light Scattering (DLS, Zetasizer nano-ZS Malvern Instruments Ltd, Worcestershire, U.K.). 5 nmol (0.08 mg) siRNA was added to the NP solution and allowed to electrostatically complex for 30 min to form siNPs. 5 mg of trehalose (60:1 weight ratio to siRNA), a lyophilization excipient, was added to the siNP solution and allowed to dissolve for 30 min. The siNP solutions were then frozen and lyophilized.

Polyester Polyol and PTK Diol Synthesis and Characterization

A trifunctional polyester polyol (PE) was synthesized as previously described[63]. Briefly, glycerol was vacuum dried for 48h at 80°C and then added to a 100mL three neck flask. By molar amount, 60% ε-caprolactone, 30% glycolide, and 10% D,L-lactide were added to the glycerol starter with a stannous octoate catalyst to yield a 900 g mol^{-1} triol. 100% MEE-PTK or 0% MEE-PTK diol polymers were synthesized as previously documented[30], as adapted from Wilson et al.[45]. P-toluenesulphonic acid monohydrate was dried by azeotropic distillation with toluene, dissolved in 60°C hydrochloric acid, and then recrystallized at -20°C. Crystals were extracted, rinsed with cold HCl, and dried under vacuum for 1 h. The catalyst was added to a tri-neck boiling flask with an attached addition funnel. Both vessels were put under positive nitrogen pressure and charged with anhydrous acetonitrile. MEE or 1,4 butanedithiol (BDT) was added to the boiling flask (1*x* molar eq), while 1*x* molar eq of 2,2 dimethoxypropane (DMP) was added to the addition funnel. The solutions in both the addition funnel and boiling flask were purged with flowing nitrogen for 30 min before submerging the boiling flask into an oil bath at 80°C. After 15 min of temperature

equilibration, the acetonitrile-DMP solution was added drop-wise into the continuously–stirring, boiling flask for 1 h and allowed to mix for an additional 16 h. Post synthesis, the acetonitrile was removed by rotary evaporation, and the resultant PTK polymer was isolated by precipitation into cold ethanol and dried under vacuum. The resulting dithiol precursor was analyzed by GPC using poly(ethylene glycol) (PEG) standards (400 – 4000 g mol^{-1}) to determine molecular weight. To convert the thiol end-groups to hydroxyl groups, the PTK dithiol polymers was transferred to a boiling flask and put under positive nitrogen pressure, dissolved in anhydrous dichloromethane (DCM), and treated with a 5× molar excess of b-mercaptoethanol to reduce any disulfide bonds and recover the reactive thiol end groups. After 2 h of stirring, the DCM was evaporated and the residue was washed three times in cold ethanol under nitrogen to remove residual b-mercaptoethanol. The reduced PTK polymers were dissolved in anhydrous tetrahydrofuran (THF) before adding a 5× molar excess of cesium carbonate ($CsCO_3$) under nitrogen and stirring for 30 min at room temperature. A 4× molar excess of 2-bromoethanol was next added to the solution and stirred for 18 h under nitrogen at room temperature. After stirring, the solution was added to a separation funnel with an excess of deionized water to effectively separate the respective PTK-containing THF layer from the water-soluble $CsCO_3$ catalyst. The hydroxyl-functionalized PTKs were extracted in THF before removing the solvent by rotary evaporation, followed by dissolving the product in water-immiscible DCM to remove any residual water. Finally, the PTK diol polymers was analyzed by GPC and NMR before vacuum drying for 24 h.

PEUR and PTK-UR Synthesis

100% MEE-PTK-UR, 0% MEE-PTK-UR, and PEUR scaffolds (100 mg) were prepared using reactive liquid molding with or without lyophilized siNPs. The respective polyol was added to a micro-centrifuge tube along with water, TEGOAMIN33 catalyst, and calcium stearate pore opener. These components, with or without the lyophilized siNPs, were first mixed for 30 s at 3300 rpm in a Hauschild DAC 150 FVZ-K SpeedMixer (FlackTek, Inc., Landrum, SC). After a homogenous mixture was obtained, the respective isocyanate (HDIt or LTI) was added and mixed for an additional 30 sec before allowing the liquid mixture to freely rise and harden for at least 2 hrs. The targeted index (ratio of isocyanate to hydroxyl equivalents

times 100) was 115, where the number of OH equivalents is calculated from the respective polyol's molecular weight. The amounts of each component for the respective scaffold formulations, given as equivalent amounts in parts per hundred parts polyol (PPHP), are given in Table A2.

In vivo degradation of PTK-UR and PEUR scaffolds in diabetic and non-diabetic rats

All surgical procedures were reviewed and approved by Vanderbilt University's Institutional Animal Care and Use Committee. 100% MEE-PTK-UR, 0% MEE-PTK-UR, and PEUR scaffolds made with HDIt were cut into 10 × 2.5 mm discs, sterilized with ethylene oxide, and implanted into ventral subcutaneous sites in adult male (non-diabetic) Sprague-Dawley rats. Scaffolds were excised from euthanized animals at weeks 1, 3, 5 and 7 to evaluate new granulation tissue formation in the implants. The excised tissues were fixed in formalin, processed, sectioned, and stained with hematoxylin & eosin. Histological sections were evaluated with Metamorph Imaging Software (Molecular Devices Inc., Sunnyvale, CA) to assess wound dimensions and scaffold degradation. The wound area was defined as the cross-sectional area occupied by the scaffold and new tissue growth. Values for the percentage of scaffold area occupying the wound area were normalized to week 1 values to eliminate the effect of scaffold compression over time, and 100% MEE-PTK-UR degradation was fit to the first-order degradation kinetics model seen in Equation 1. 100% MEE-PTK-UR scaffolds were also made with LTI, sterilized, and implanted subcutaneously in rats for 1 week before analyzing the tissue explants as previously described.

To evaluate scaffold degradation in diabetic animals, male Sprague-Dawley rats were injected with streptozotocin (STZ, 45 mg kg^{-1}) and allowed to develop hyperglycemia for 10 days. Pre-implantation, scaffold sections were sterilized with ethylene oxide and allowed to ventilate for 3 days. 10 mm diameter × 2.5 mm thickness 100% MEE-PTK-UR scaffolds made with HDIt were implanted subcutaneously in diabetic and non-diabetic rats (four scaffolds per rat), and the subcutaneous tissue samples (skin and muscle surrounding the scaffold) were excised from euthanized animals at 1 and 7 weeks post-surgery and transferred into PBS. To quantify the tissue's background autofluorescent signal, the tissue sections (muscle-side facing upwards) were imaged with a Xenogen IVIS 200 (ex: 640 nm, em: 735 nm). The tissue

sections were then incubated with an ROS-sensitive fluorescent dye (ROSstar 650, Li-Cor Biosciences, Lincoln, NE) at 100 μM for 45 min in the dark before being imaged again with the IVIS 200 using the same fluorescent filter settings[144, 253]. The excised tissues were fixed in formalin, processed, sectioned, and stained with hematoxylin & eosin (H&E). Histological sections were evaluated with Metamorph Imaging Software (Molecular Devices Inc., Sunnyvale, CA) to assess scaffold degradation.

In Vitro Screen of PHD2 siRNA

Dicer substrate siRNA designed against rat PHD2 messenger RNA (mRNA) was obtained from IDT (sequence modified from well-validated mouse PHD2 siRNA[28]) and screened for mRNA silencing in A7r5 rat smooth muscle cells. Cells were seeded at 24,000 per well in a 12-well plate and allowed to adhere for 24 h in DMEM media supplemented with 1% FBS and 1% penicillin/streptomycin. After 24 h of incubation, cells were treated with fresh media, scrambled siRNA at 50 nM, or PHD2 siRNA at 50 nM. The respective siRNA treatments were pre-complexed with Lipofectamine 2000 in OptiMEM and diluted into culture media following the manufacturer's protocol. After 24 h of incubation with the siRNA, the media was removed and replaced with fresh media. After another 24 h (48 h following original siRNA treatment), cells were washed, lysed, and processed using a QiaShredder kit (Qiagen, Venlo, Netherlands). RNA was extracted using a Qiagen RNeazy column following the manufacturer's protocol and quantified for quality and concentration using a NanoQuant plate on a Tecan microplate reader. cDNA was synthesized using an iScript cDNA Synthesis Kit (Bio-Rad, Hercules, CA), and quantitative real-time polymerase chain reaction (qRT-PCR) was performed using Bio-Rad iQ SYBR Green Supermix. Relative PHD2 expression levels were normalized to glyceraldehyde 3-phosphate dehydrogenase (GAPDH) using the ΔΔCt method. Primer sequences are given in Table A3.

In Vitro Nanoparticle Release from PTK-UR Scaffolds

1 mg of the nanoparticle-forming polymer was dissolved in a minimal volume of ethanol in a 2 mL RNAse free polypropylene tube followed by slow addition of deionized water to trigger spontaneous

micelle formation (final polymer concentration 1 mg in 1 mL). 5 nmol (0.08 mg) of Cy5-labeled, double-stranded DNA, similar to siRNA molecular weight, was added to the NP solution and allowed to electrostatically complex for 30 min to form fluorescently-labeled DNA-NPs. 5 mg of trehalose (60:1 weight ratio to DNA), a lyophilization excipient, was added to the siNP solution and allowed to dissolve for 30 min. The siNP solutions were then frozen and lyophilized. 100 mg PTK-UR (LTI) scaffolds were made with the lyophilized DNA-NPs, allowed to harden, and cut into six sections. The individual scaffold sections were incubated in 1 mL of phosphate buffered saline (PBS), with the PBS being removed at designated time points and evaluated for Cy5 fluorescence using a microplate reader (Tecan Infinite F500, Männedorf, Switzerland). The concentration of labeled nanoparticles in solution, and therefore the drug release rate, was determined based on fluorescence measurement of Cy5-labeled DNA-NPs.

Diabetic Excisional Wound Healing with PTK-UR and PEUR Scaffolds

To evaluate diabetic wound healing in rats, male Sprague-Dawley rats with STZ-induced diabetes were shaved and sterilized with iodine. Six full-thickness excisional wounds were made on the rats' dorsal skin with an 8-mm biopsy punch. Ethylene oxide-sterilized PEUR or PTK-UR scaffolds (8 mm diameter × 1.5 mm thickness) made with LTI or HDIt were placed in the wounds, covered with a non-adherent, absorbent ReliaMed hydrogel dressing, and then covered with an adherent Tegaderm outer dressing which was stapled to non-wounded skin to provide additional stability. Finally, each rat was fitted with a velcro-fastened jacket (Lomir Biomedical, Inc., Malone, NY) to prevent self-tampering with the dressings[254] and singly housed in the rodent facility. Rats were euthanized at 4, 7, and 14 days post-surgery and excised scaffold/tissue sections were processed for histology with H&E staining. Stained tissue sections were analyzed for scaffold tissue infiltration (% scaffold wound area containing tissue), thickness of tissue in-growth (distance tissue has infiltrated from bottom of scaffold upwards into the scaffold interior), and macrophage presence in the scaffold tissue (% CD68-positive pixel area per cross-sectional scaffold pixel area stained) with ImageJ 1.48v software (National Institute of Health, Bethesda, MD).

In Vivo Silencing of PHD2 in Diabetic Excisional Wounds

PEUR and PTK-UR scaffolds were fabricated with or without lyophilized siNPs plus trehalose (1 mg NP polymer, 5 nmol siRNA, and 5 mg trehalose per 100 mg scaffold). Scaffold implants were designated by their siNP payload: no treatment (NT), scrambled siRNA (SCR-siNP), and anti-PHD2 siRNA (PHD2-siNP). siRNA sequences are given in Table A3. Ethylene oxide-sterilized scaffold sections were implanted in excisional wounds in diabetic rats as described previously. As an initial screen to measure the effects of PHD2-siNP delivery from PEUR vs PTK-UR scaffolds, both scaffold formulations with NT, SCR-siNP, and PHD2-siNPs were implanted into diabetic rats which were euthanized at day 7 post surgery for blood vessel analysis. Vessel area per scaffold was measured from H&E stained tissue sections. A follow-up study was completed using only using the better-performing PTK-UR scaffolds with NT, SCR-siNP, and PHD2-siNP treatments. At days 4 and 7 post-surgery, scaffold/tissue sections were extracted from euthanized rats and processed for histology with H&E and trichrome blue staining. Small pieces of tissue-infiltrated scaffolds (~20mg) from all three time points were also extracted and saved in RNAlater (ThermoFisher Scientific, Grand Island, NY). Tissues were put into 2 mL microcentrifuge tubes with 5 mm stainless steel beads and Qiazol (Qiagen, Venlo, Netherlands) and pulsed at 300 Hz for 2 min in a Qiagen Tissuelyser II to completely disrupt the tissue and extract RNA. Extracted RNA was purified with RNeasy spin columns, including on-column genomic DNA elimination using a Qiagen RNase-free DNase kit, and quantified for quality and concentration using a NanoQuant plate on a Tecan microplate reader. cDNA was synthesized using an iScript cDNA Synthesis Kit, and qRT-PCR was performed using Bio-Rad iQ SYBR Green Supermix. Relative gene expression levels were normalized to glyceraldehyde 3-phosphate dehydrogenase (GAPDH) and cyclophilin B (PPIB) using the ΔΔCt method. Primer sequences are given in Table A3.

Western blot analysis of extracted tissues

Western blot analysis was also performed on scaffold/tissue samples extracted from day 4 animals. Frozen samples were extracted with UDC buffer (8 M urea, 10 mM dithiothreitol (DTT), 4% CHAPS containing Phosphatase I and II protease inhibitor cocktail (Sigma, St. Louis, MO)) by vortexing at room

temperature overnight and centrifugation at 14,000 rpm for 15 min at 4°C. Soluble protein concentrations were determined using the Bradford assay (Pierce Chemical, Rockfort, IL). Equal amounts (30 μg) of proteins were added to Laemmli sample buffer (Bio-Rad), heated for 5 min at 100°C, and separated on 12% SDS polyacrylamide gels. Proteins from the gels were transferred onto nitrocellulose membranes (Li-COR Biosciences, Lincoln, NE) and blocked with blocking buffer for 1 hour at room temperature (Li-COR Biosciences) prior to incubation overnight at 4°C with antisera against VEGF (1:1000, Santa Cruz Biotechnology), HIF-1α (1:1000, Santa Cruz Biotechnology), and GAPDH (1:1000, Millipore). Membranes were washed three times with TBS containing Tween 20 (0.1%) (TBST) and incubated with 680 nm and 800 nm infrared-labeled secondary antibodies (Li-Cor, Lincoln, NE) for 1h at room temperature. The membranes were subsequently washed with TBST, and protein-antibody complexes were visualized and quantified using an Odyssey direct infrared fluorescence imaging system (Li-Cor).

Immunohistochemical staining of tissue sections

Immunohistochemical staining was performed using commercial antibodies specifically directed against rat CD68 (MCA341GA, Bio-Rad), collagen IV (ColIV) (ab6586, Abcam, Cambridge, MA), α-smooth muscle actin (α-SMA) (RB-9010, Labvision, Freemont, CA), Ki67 (ab16667, Abcam) and S100A4 (ab197896, Abcam). Formalin-fixed paraffin embedded tissues were sectioned at 5 μm, placed on slides and warmed overnight at 60°C. Slides were deparaffinized and rehydrated with graded alcohols ending in Tris buffered saline (TBS-T Wash Buffer, LabVision, Freemont, CA). Heat mediated target retrieval was performed in 1X Target Retrieval Buffer (Citrate, pH 6.0, DAKO, Carpenteria, CA). Endogenous peroxidases and non-specific background were blocked by subsequent incubations in 3% H_2O_2 (Fisher, Suwanee, GA) in TBS-T and protein block (DAKO). For CD68, primary antibody was used at 1:800 for 1hr, followed by secondary incubation in biotinylated rabbit anti-mouse IgG (1:200; Vector, Burlingame, CA) and subsequent tertiary incubation in SA-HRP (RTU, BD Pharmingen, San Jose, CA). For Col IV, primary antibody was used at 1:600 for 1 hr, with the Bond Refine Polymer detection system used for

visualization. For α-SMA, primary antibody was used at 1:1000 for 1 hr, with the Bond Refine Polymer detection system used for visualization. For Ki67, primary antibody was used at 1:100 for 1 hr, with the Bond Refine Polymer detection system used for visualization. For S100A4, primary antibody was used at 1:2000 for 1 hr, followed by secondary incubation in anti-rabbit EnVision + labeled polymer (DAKO). Slides were rinsed with TBS-T between each reagent treatment and all steps were carried out at room temperature. Visualization was achieved with DAB+ chromogen (DAKO). Slides were counterstained with Mayer's hematoxylin, dehydrated through a series of alcohols and xylenes, and then coverslipped with Acrytol Mounting Media (Surgipath, Richmond, IL).

Histological analysis of wound healing outcomes

Quantitative analysis of healing outcomes between scaffold formulations and siNP treatments was determined histologically from day 7 tissue samples. The excised tissues were fixed in formalin, processed, embedded in paraffin, sectioned, and prepared for staining or immunohistochemistry (IHC). IHC using CD68, Col IV, α-SMA, Ki67, and S100A4 antibodies was performed on scaffold/tissue sections and quantified using ImageJ. Macrophage presence between PEUR and PTK-UR scaffolds was quantified as the CD68-positive pixel area per cross-sectional scaffold pixel area. Overall blood vessel counts per cross-sectional scaffold area were determined from Col IV IHC sections, while more mature vessels were similarly quantified from α-SMA IHC sections. Ki67-positive pixel area per cross-sectional scaffold pixel area was quantified for the presence of proliferating cells, and concurrent S100A4 IHC tissue sections were compared to Ki67 sections to broadly verify if the proliferating cells positively expressed the S100A4 marker. Trichrome blue-stained sections were analyzed for tissue infiltration differences between SCR-siNP and PHD2-siNP as previously described.

Statistical Analysis

All data are reported as the mean and standard error of the mean unless otherwise indicated. Statistical analysis was performed using single factor analysis of variance (ANOVA) and Tukey post-hoc comparison

tests for multiple comparisons, and the Student's t-test was used for single comparisons. P-values less than 0.05 were considered statistically significant.

4.3 Results and discussion

The PTK-UR scaffolds' lack of cytotoxicity and compatibility with cellular infiltration (Chapter 1) were confirmed *in vivo* by histological analysis of subcutaneous implants. The biocompatibility and degradability of PTK-UR scaffolds made with HDIt was confirmed after implanting 100% MEE-PTK-UR, 0% MEE-PTK-UR, and 900t-PEUR scaffolds subcutaneously into male, non-diabetic Sprague-Dawley rats. The 100% MEE-PTK-UR, and 900t-PEUR scaffolds demonstrated robust cellular infiltration, a minimal inflammatory response, and granulation tissue formation by 3 weeks post implantation (Figure 13A). However, the 0% MEE-PTK-UR scaffolds supported much less robust tissue infiltration into the scaffold interior relative to the 100% MEE-PTK-UR or 900t-PEUR scaffolds. One possible explanation for this result is that the relative hydrophobicity of the 0% MEE-PTK-UR scaffolds (80° contact angle) did not allow cells to properly adhere and migrate into the scaffold interior. As a result, only the 100% MEE-PTK-UR and 900t-PEUR histology samples were quantitatively analyzed. Both of these formulations supported new tissue growth and displayed significant biodegradation over 7 weeks (Figure 13B). The 900t-PEURs experienced accelerated degradation after 3 weeks as expected from previous work with these materials [76], while the 100% MEE-PTK-UR scaffolds displayed first-order degradation over time. This finding confirms the initial hypothesis that PTK-UR scaffolds degrade by a cell-mediated mechanism compared to the hydrolytic degradation of the more conventional PEUR materials, which have been shown to undergo autocatalytic degradation *in vivo* resulting in a reduced wound healing response [36].

Furthermore, the PTK-UR samples were more mechanically resilient and were more effective in maintaining implant geometry as seen in Figure 13A and C. Though all scaffolds initially possessed 90% porosity and were cut to the same dimensions pre-implantation, the PEUR materials were significantly more compressed than the PTK-UR scaffolds by week 1. As the wound length was relatively consistent between PTK-UR and PEUR scaffolds (Figure A8), the total wound area values closely mirrored the trends seen in

the scaffold thickness measurements (Figure A9). This *in vivo* compression of PEUR scaffolds can be potentially attributed to both the significantly higher modulus of the 100% MEE-PTK-UR samples relative to the 900t-PEUR formulation (Figure 9) and also to the 900t-PEUR T_g value (34.4 °C) which is close to body temperature (Table A1). This relatively high T_g predicts that the PEUR scaffolds would be less mechanically resilient at body temperature because they would be in their glass transition viscoelastic region. The stenting effect seen in these PTK-UR scaffolds is advantageous because it ensures that the scaffold pores remain open, maximizing cell infiltration and new tissue formation and potentially decreasing scarring in clinical applications [255].

As PTK-UR materials exhibited dose-dependent degradation with respect to ROS concentrations *in vitro*, animal experiments were carried out to confirm ROS-dependent degradation kinetics *in vivo*. PTK-UR scaffolds made with HDIt were subcutaneously implanted in non-diabetic and streptozotocin-induced diabetic rats and allowed to integrate for 1 or 7 weeks. Chronic diabetic wounds have elevated oxidative stress compared to acute wounds[256, 257], signifying that diabetic wounds could increase the degradation rate of PTK-UR scaffolds *in vivo.* After incubating tissue/scaffold explants in an ROS-responsive dye (Figure 14A), samples from diabetic and non-diabetic rats did not possesses statistically different levels of ROS at 1-week post-surgery (17 days post STZ injection). However, tissue-level ROS signal was significantly different at 7 weeks with the diabetic rats exhibiting higher levels of ROS as predicted (Figure 14B). The 100% MEE-PTK-UR scaffolds implanted in these tissue sections exhibited corresponding levels of degradation, with scaffolds implanted for only 1 week exhibiting no difference between diabetic and non-diabetic rats and scaffolds implanted for 7 weeks being significantly more degraded in diabetic rats (Figure 14C). These findings further confirm that ROS concentrations significantly impact degradation of PTK-based materials both *in vitro* and *in vivo*.

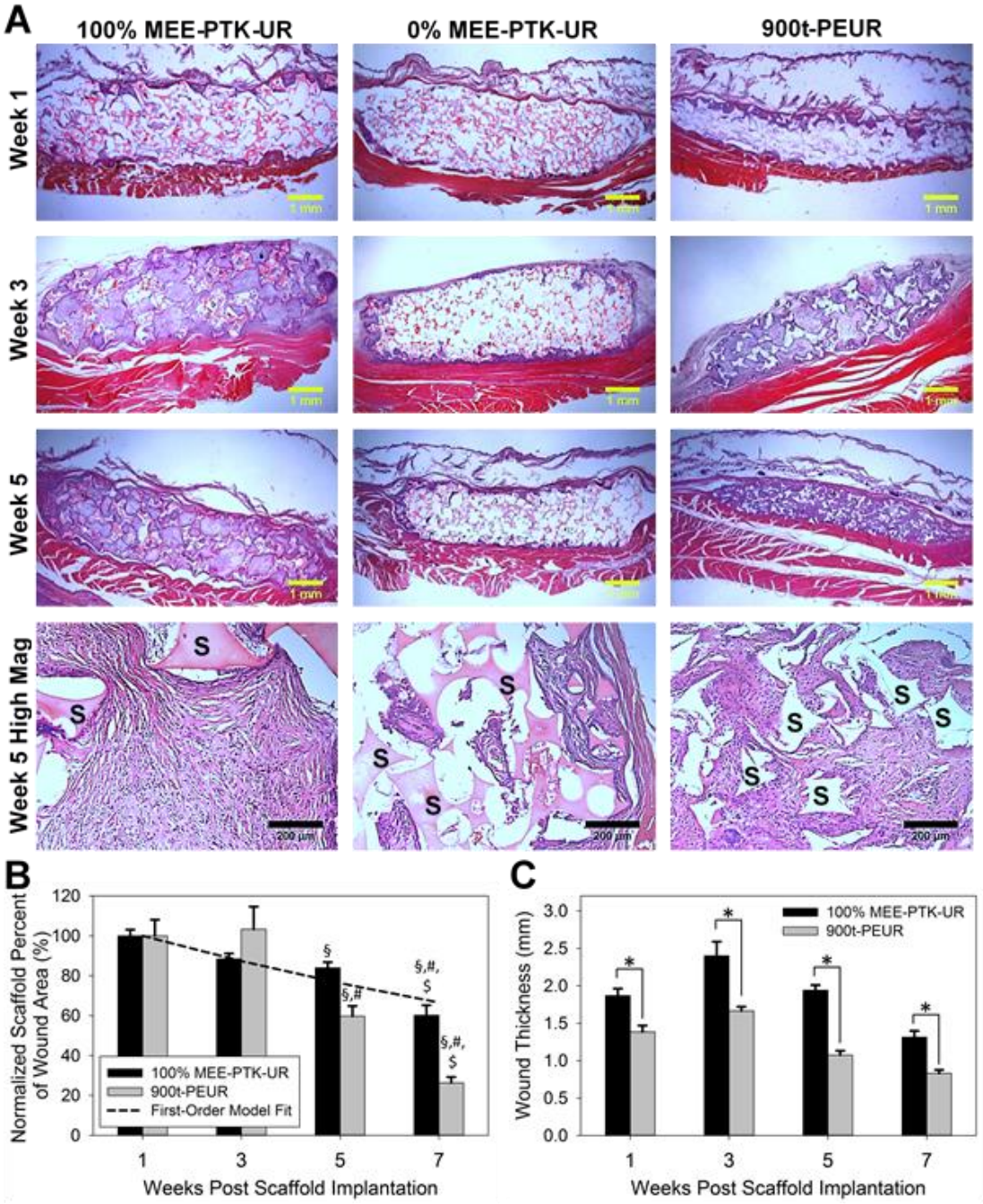

Figure 13. *In vivo* response of subcutaneous PTK-UR scaffolds in Sprague-Dawley rats. (A) Histological illustration of cellular infiltration into PTK-UR and control PEUR scaffolds (residual scaffold material is designated with '*S'* in the week 5 high magnification panels). The 100% MEE-PTK-URs supported robust tissue in-growth, but the 0% MEE-PTK-UR formulation did not. (B) *In vivo* scaffold degradation normalized to week 1. Though initially 90% porous, the PEURs were compressed post-implantation and experienced more accelerated degradation after 3 weeks, while the PTK-URs degraded more slowly and with more temporally-constant first-order degradation kinetics (dashed line represents model-generated curve). $^{\S}p < 0.05$ compared to week 1, $^{\#}p < 0.05$ compared to week 3, $^{\$}p < 0.05$ compared to week 5. (C) Compression of PTK-UR vs. PEUR scaffolds *in vivo*. The PTK-UR scaffolds maintained their mechanical integrity/thickness and provided a greater stenting effect relative to the PEUR implants, $*p < 0.05$.

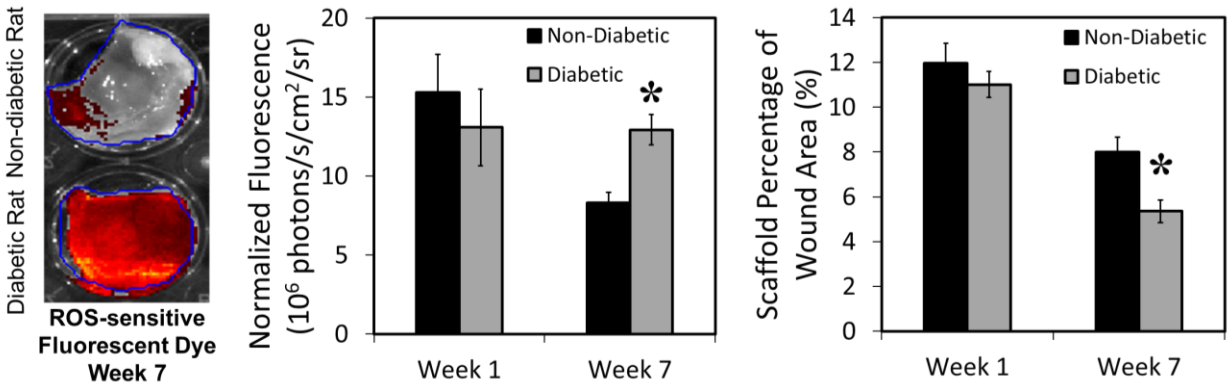

Figure 14. *In vivo* degradation of subcutaneous PTK-UR (HDIt) scaffolds in diabetic and non-diabetic Sprague-Dawley rats. Tissue/scaffold explants from diabetic rats after 7 weeks (A) soaked in an ROS-responsive fluorescent dye have (B) higher levels of ROS than non-diabetic animals. These higher levels of tissue ROS also correspond with significantly greater degradation of ROS-sensitive PTK-UR scaffolds after 7 weeks (*$p<0.05$).

As determined from histological sections with hematoxylin and eosin (H&E) staining (Figure 15A), both implanted scaffold formulations had substantial tissue infiltration throughout the scaffold at day 4 post implantation. Tissue infiltration was defined as the cross-sectional area of the scaffold wound site that was occupied by granulation tissue (i.e. area not occupied by scaffold, intact dermis, or blank space). At day 7, both material formulations had significantly more tissue infiltration compared to day 4 levels, but the PTK-UR implants had both significantly greater infiltration (Figure 15B) and (similar to previous *in vivo* observations)[30] significantly greater stenting of the wound leading to a thicker layer of tissue growth within the PTK-UR scaffolds than within analogous PEURs (Figure 15C). The newly formed tissue was also evaluated in day 7 tissue sections by CD68 immunohistochemistry (IHC) to determine the presence of inflammatory cells. Quantification of IHC staining for this macrophage marker[258] revealed that there was no significant difference in macrophage presence between tissues surrounding PEUR and PTK-UR implants (Figure A12), suggesting that these materials elicited a similar inflammatory response. Both scaffold types were nearly fully resorbed by day 14, indicating that the use of LTI in the material formulation significantly increased the *in vivo* degradation rate of these scaffolds compared to similar implants made with minimally-degradable HDIt[30, 76]. However, PTK-UR scaffolds promoted a highly favorable regenerative response with enhanced tissue infiltration, thicker tissue ingrowth, and similar

presence of macrophages compared to conventional PEUR materials. These results supported the use of PTK-UR implants in subsequent studies.

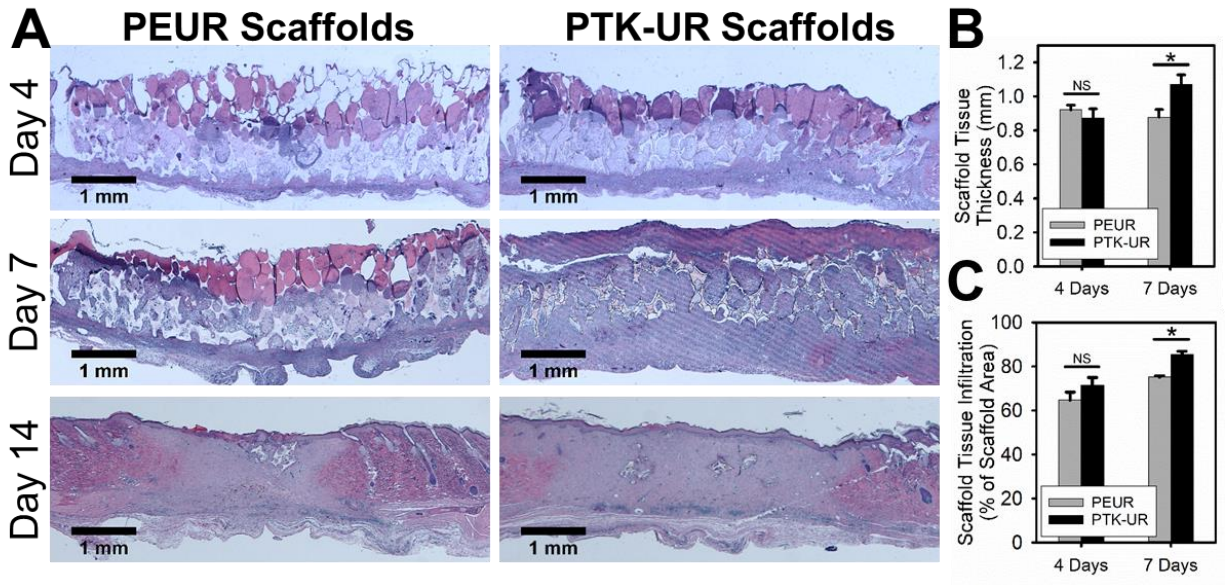

Figure 15. PEUR and PTK-UR scaffolds made with LTI and implanted into diabetic excisional wounds (A) were largely degraded by 14 days and covered by new epidermis. Implanted PTK-URs promoted (B) greater wound stenting/thicker granulation tissue formation and (C) supported more robust tissue infiltration over 7 days (mean ± SEM, n = 7 independent animals, *$p<0.05$).

To demonstrate the therapeutic potential of localized, scaffold-based siRNA delivery to clinically-relevant diabetic wounds, siRNA-carrying micellar nanoparticles (siNPs) were formulated with siRNA targeting PHD2 (PHD2-siNPs) or scrambled control siRNA (SCR-siNPs) and incorporated into PEUR and PTK-UR scaffolds. Both the scrambled and PHD2 siRNA sequences (Table A3) were pre-screened *in vitro* to ensure effective PHD2 gene silencing in rat cells as seen in Figure A13. The self-assembling, siRNA-condensing nanoparticles were composed of a diblock copolymer synthesized by reversible addition-fragmentation chain transfer (RAFT) polymerization, containing 2-(dimethylamino) ethyl methacrylate (DMAEMA), 2-propylacrylic acid (PAA), and butyl methacrylate (BMA) as previously described[28, 85, 130, 250]. As depicted in Figure 16B, the final polymer, $DMAEMA_{67}$-*b*-($DMAEMA_{29}$-*co*-BMA_{75}-*co*-PAA_{40}), achieved a final molecular weight of 30,500 Da and was self-assembled into micellar nanoparticles. The addition of siRNA (5 nmol) to the micelle solution (1 mg polymer in 1 mg water) formed stable siNPs

(D_h = 31 nm, ζ-potential = +20.2 mV), which were optimized to achieve pH-dependent endosomal escape and intracellular siRNA delivery[130, 250]. After loading of the siRNA cargo, the excipient trehalose (60:1 weight ratio to siRNA) was added to the siNP solution to both stabilize the nanoparticles through lyophilization[86, 259] and to increase *in vivo* siNP release from implanted scaffolds[28]. After lyophilization, the siNP-trehalose powder was mixed into the liquid PEUR or PTK-UR reaction (100 mg prepolymer), leading to homogenous distribution throughout the final 3D polymer structure following scaffold hardening. Corresponding to the rapid cellular infiltration seen in Figure 15, the specific dose of trehalose (5 wt% of the final scaffold weight) was chosen to facilitate relatively fast siNP release from implanted scaffolds with the aim of transfecting these early infiltrating cells. Initial testing of *in vitro* nanoparticle release from PTK-UR scaffolds using fluorescently-labeled double stranded DNA as a model for siRNA indicated that, similarly to *in vitro* siNP release data from PEUR scaffolds with the same dose of trehalose[28], much of the siRNA payload was released over a two-day time course (Figure A14).

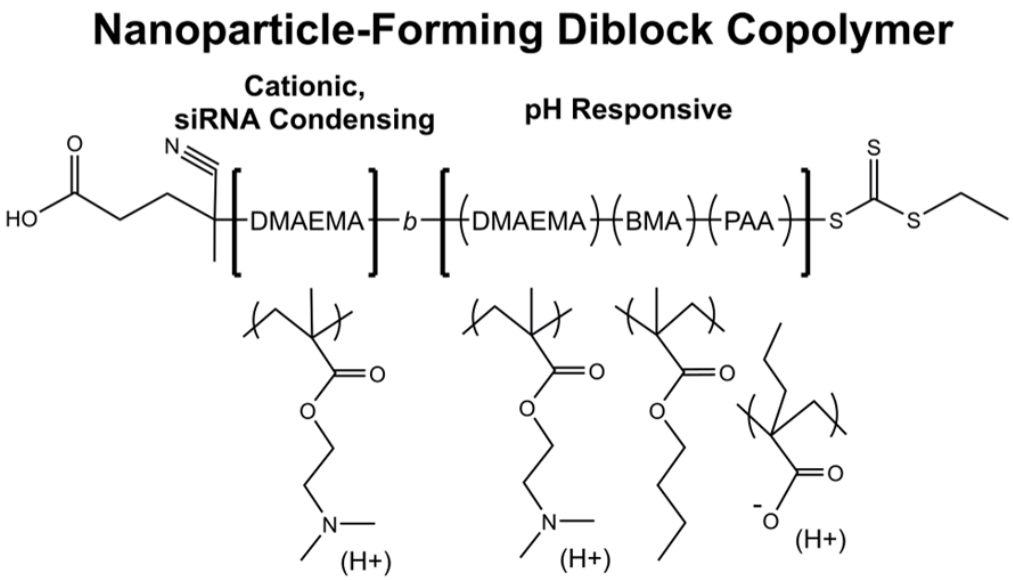

Figure 16. Structure of the micelle-forming diblock copolymer DMAEMA-*block*-(DMAEMA-*co*-BMA-*co*-PAA).

As an initial screen of the effectiveness of siNP delivery from PEUR and PTK-UR implants, no treatment scaffolds (NT) along with PHD2 and SCR siNP-loaded scaffolds were implanted into excisional wounds in STZ-diabetic rats and histologically evaluated after 7 days. Blood vessel area in H&E sections was quantified for PEUR and PTK-UR scaffolds with NT, SCR-siNP, and PHD2-siNP treatments. As seen

in Figure A15, pilot *in vivo* data indicated that loading with PHD2-siNPs tended to cause increased vessel area in both PEUR and PTK-UR scaffolds. However, the NT PTK-UR scaffolds had a statistically higher vessel cross-sectional area than the NT PEUR scaffolds (Figure A15), indicating that PTK-UR scaffolds promoted more blood vessel growth than PEURs even without siNP treatment. Because PTK-URs encouraged both a more robust healing response (Figure 15) and enhanced baseline blood vessel formation (Figure A15) compared to the more conventional PEUR materials, a larger diabetic rat study was carried out using only the better-performing PTK-UR scaffolds loaded with siNPs.

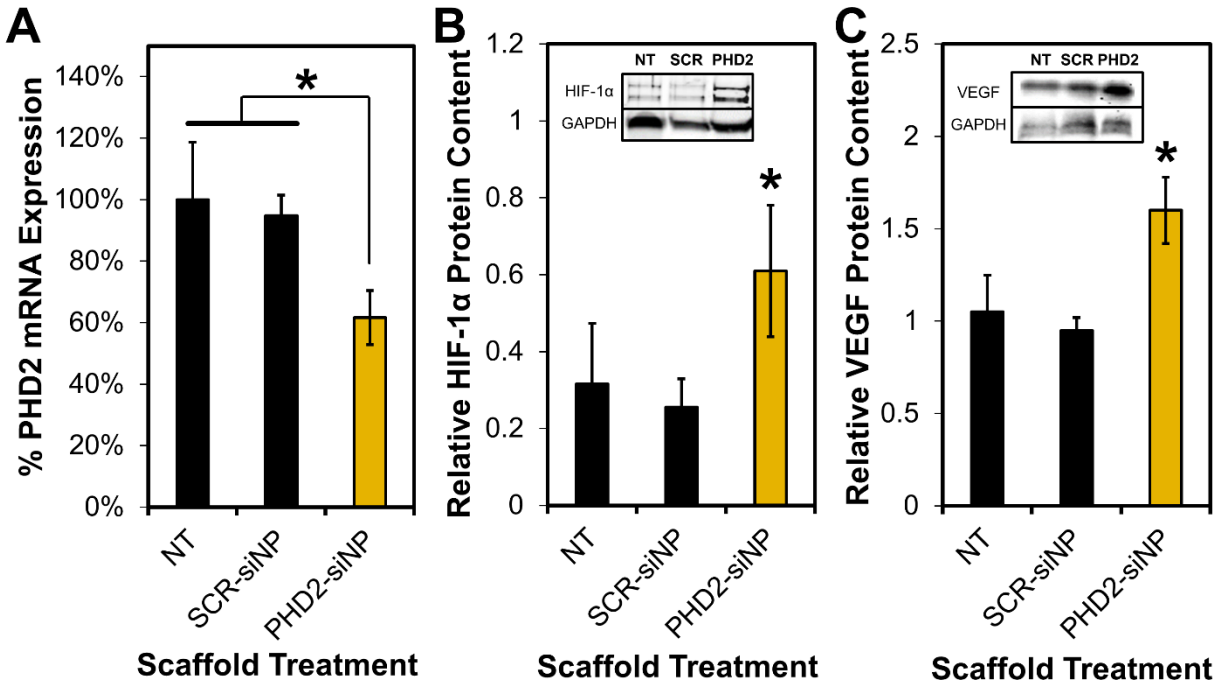

Figure 17. PTK-UR scaffolds loaded with PHD2-siNPs (A) significantly decrease PHD2 mRNA within the wound tissue scaffolds compared to NT and SCR-siNP implants, leading to (B) increased HIF-1α and (C) increased VEGF protein levels compared to SCR-siNP implants at day 4 post-implantation (mean ± SEM, n = 6 independent animals, *$p<0.05$).

In the scaled up study, excisional wounds in STZ-diabetic rats were implanted with sterilized PTK-UR scaffolds made with LTI (NT, SCR-siNP, or PHD2-siNP treatments, 0.5 nmol siRNA per SCR or PHD2-siNP scaffold). Tissue/scaffold samples from day 4 post implantation revealed 40% knockdown of PHD2 messenger RNA in PHD2-siNP scaffolds compared to NT and SCR-siNP implants (Figure 17A) as determined by quantitative real-time polymerase chain reaction (qRT-PCR, primer sequences listed in Table A3). The downstream transcriptional impact of PHD2 silencing was also confirmed, since both HIF-

1α and VEGF protein levels were also significantly increased in the treatment group as quantified by western blot analysis compared to SCR-siNP scaffolds (Figure 17B-C). qRT-PCR of day 7 tissue samples did not show a significant decrease in PHD2 expression compared to NT or SCR-siNP implants (data not shown), potentially due to the relatively fast *in vivo* release of siNPs with added trehalose[28]. However, day 7 histological sections immunostained for collagen IV (Col IV), a marker of vascular basement membranes[87], indicated a persistent increase in blood vessel density in PHD2-siNP scaffolds compared to SCR-siNP implants (Figure 18A). Enhanced vessel formation is a hallmark effect of PHD2 inhibition[18, 19, 27, 29] and is heavily implicated in improved wound healing outcomes. Furthermore, there was a higher density of vessels in PHD2-siNP scaffolds expressing α-smooth muscle actin (α-SMA), a marker of vessel maturation[198], as visualized by α-SMA IHC in Figure 18B. These data collectively demonstrate that a higher density of both immature and mature blood vessels form within the PHD2-siNP scaffolds compared to control materials. This animal experiment was also repeated with siNP-loaded PTK-UR scaffolds made with HDIt to assess the effect of scaffold chemistry on the longevity of PHD2 silencing *in vivo*. As demonstrated in Figure A16, the HDIt scaffolds also promoted significant knockdown of PHD2 expression at day 4 post implantation but did not have significant silencing at day 7 (data not shown). However, the tissue infiltration response to HDIt materials in excisional wounds was significantly diminished compared to LTI scaffolds (Figure 15). These results indicate that though PTK-UR scaffolds made with HDIt achieve similar results *in vivo* silencing of PHD2 with scaffold-delivered siNPs, the relatively negative tissue response to HDIt materials limits the utility of these materials for wound healing applications.

Immunostaining for Ki67, a marker for cell proliferation[87], also indicated that there was a significant increase in proliferating cells throughout the PHD2-siNP scaffolds (Figure 18C). Decreased PHD2 expression in cutaneous tissue is known to increase cell proliferation and migration while enhancing overall wound closure in mouse skin lesions[17]. Closer inspection suggested that the proliferating cells were largely granulation tissue-forming fibroblasts. To confirm cellular identity, tissue sections immunostained for S100A4, a fibroblast marker[260], were compared to Ki67 IHC sections. As seen in representative images in Figure A17, comparing serial tissue sections immunostained for both markers indicated that

regions of dense Ki67-positive proliferating cells also had high levels of expression of S100A4. These data suggest that PHD2-siNP mediated cellular proliferation is generating fibroblasts that can aid wound restoration[261].

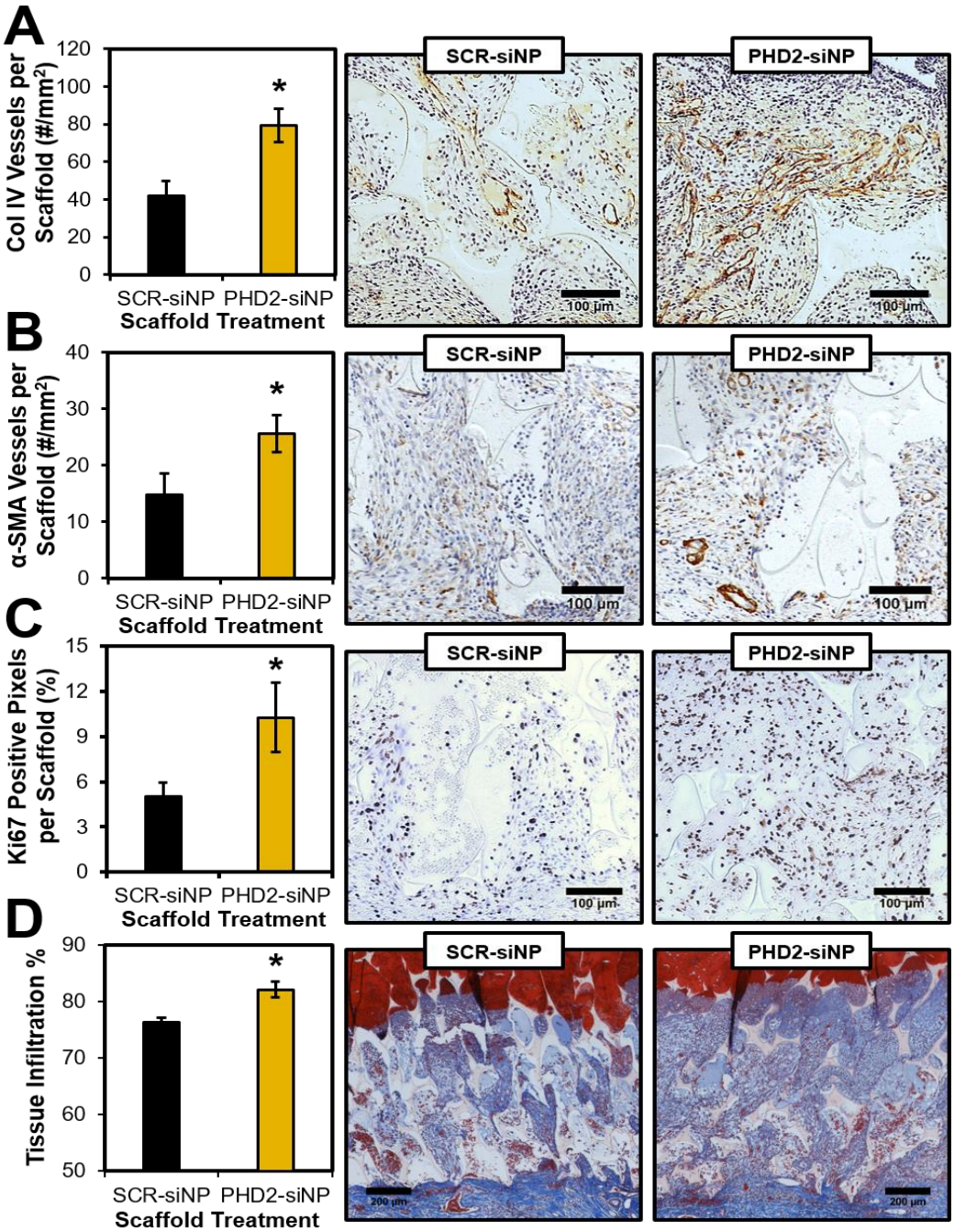

Figure 18. PHD2-siNP scaffolds featured (A) improved overall tissue vascularization as visualized by Col IV IHC, along with (B) more mature vessel formation as denoted by α-SMA IHC. PHD2-siNP scaffolds also (C) had increased cellular proliferation as visualized by Ki67 IHC, leading to (D) an overall increase in tissue infiltration into implanted scaffolds (mean ± SEM, n = 7 independent animals, *$p<0.05$).

Although much past work has used surface wound closure percentage as a marker for overall healing in rodent models[17, 27], these biodegradable polyurethane scaffolds are designed to stent open contracting skin to decrease collagen alignment and scarring and improve the quality of new tissue formed[79, 80, 255, 262], thus making topical measurements of wound closure a less relevant measure of healing in this system. This is highlighted in the macroscopic wound images in Figure A11, as wounds at day 7 are all roughly the same size between PEUR and PTK-UR implants due to the stenting effect of the scaffolds. Despite the similarity in apparent wound size, the amount of new tissue growth as gauged by histological evaluation was significantly different between the two formulations (Figure 15) thereby demonstrating the better sensitivity by measuring tissue growth within the wound histologically. To gauge overall wound healing of PHD2-siNP against SCR-siNP scaffolds at day 7, histological sections stained with Masson's trichrome blue were evaluated for the level of tissue infiltration into the scaffold. PHD2-siNP scaffolds had a statistically significant increase in tissue infiltration compared to SCR-siNP scaffolds as depicted in Figure 18D, indicating that the local delivery of PHD2 siRNA from biodegradable scaffolds increased the amount of tissue within scaffolds and improved refilling of the diabetic wounds with vascularized, reparative granulation tissue.

4.4 Conclusion

In conclusion, PTK-UR scaffolds support cell infiltration and granulation tissue formation *in vivo*, and their superior mechanical properties produced significantly greater stenting of subcutaneous implants compared to more standard PEUR scaffolds. Furthermore, the PTK-URs experienced controlled, first-order kinetics of biodegradation *in vivo*, in contrast to the PEUR scaffolds which experienced accelerated rates of degradation over time. PTK-UR scaffolds also represent a promising biomaterial technology for the healing of chronic diabetic wounds both as a regenerative tissue engineering scaffold and as a drug depot for localized therapeutic delivery. Implanted PTK-UR scaffolds promote more robust tissue regeneration in diabetic wounds than benchmark PEUR scaffolds. Furthermore, the local, scaffold-based delivery of siNPs to silence PHD2 expression is an effective and potent strategy for improving vascular development,

cellular proliferation, and new tissue growth in diabetic wounds. These results represent a promising, clinically translatable approach to treat non-healing skin wounds, and ongoing work will further elucidate the impacts of PHD2 knockdown kinetics in this diabetic wound healing model and in more advanced pre-clinical settings.

CHAPTER 5

Enhanced Cell Viability and In Vivo Degradation of PTK-Crosslinked PEG Hydrogels

Text partially adapted from:

Martin JR, Prarthana P, Gupta MK, Duvall CL. Enhanced Cell Viability and *In Vivo* Degradation of Injectable, Reactive Oxygen Species-Sensitive PEG Hydrogels. In preparation.

5.1 Introduction

Synthetic hydrogels have emerged as promising materials in regenerative medicine applications due to their highly hydrated nature and robust cross-linked polymer networks that mimic the natural three-dimensional extracellular matrix[88]. Importantly, when compared to naturally derived materials such as collagen or gelatin, artificial matrices offer the advantages of much higher degrees of control over cellular adhesion molecule presentation, manufacturability, and material mechanical properties[89]. Due to their intrinsically low protein-adsorption[90], precedent for safe *in vivo* usage, and ease of functionalization[91], hydrogels fabricated from poly(ethylene glycol) (PEG) remain the most heavily investigated matrix-mimicking class of synthetic biomaterials. These hydrogels are most commonly formed by the covalent cross-linking of PEG macromers, which swell upon exposure to water due to PEG's hydrophilic nature but do not dissolve due to the covalently linked polymer network. Recent work in the area has focused on *in situ* cross-linking PEG hydrogels that can be delivered in a minimally invasive manner in the clinic while maintaining an active depot of living cells[92-94], proteins[95], or drugs[96].

Strategies for inducing *in situ* hydrogel formation include UV cross-linking of acrylate or ene-terminated units in the presence of a photo-initiator[92, 95, 97], enzyme-mediated cross-linking with horseradish peroxidase[98-100], covalent cross-linking induced by click reactions[101, 102], or Michael-type addition[103-105]. In particular, Michael-type addition does not require an exogenous light source or free radicals to achieve polymerization, but instead uses a nucleophilic reagent to catalyze the addition

reaction between a branched, end-functionalized PEG macromer and a multi-functional nucleophilic cross-linker[111]. PEG macromers end-functionalized with acrylate and vinyl-sulfone groups have been previously investigated[103, 105, 112], and recently, García et al. have explored the use of maleimide-functionalized PEG (PEG-MAL) macromers as precursors for injectable hydrogels formed by Michael-addition cross-linking[93, 94, 263]. Maleimide groups have been extensively used in peptide biochemistry as they quickly and efficiently react with thiol groups with very high specificity at physiological pH levels[113]. When compared to more conventional Michael-addition hydrogel systems featuring acrylate or vinyl-sulfone groups, these PEG-MAL materials possess superior cytocompatibility, increased cross-linking efficiency, and appropriate *in situ* gelation kinetics that make this system ideal for *in vivo* delivery applications[93]. Furthermore, PEG-MAL macromers demonstrate limited cytotoxicity and inflammation *in vivo* while possessing rapid renal clearance of the hydrogel degradation products[94]. In a therapeutic capacity, PEG-MAL hydrogels have shown promise as delivery vehicles for both bioactive proteins[94, 263-265] and viable cells[94, 266].

Importantly for their *in vivo* translatability, these PEG-MAL hydrogels are also fabricated with protease-cleavable peptide linkers specifically tailored to degrade in response to cell-produced matrix metalloproteinase (MMP) enzymes, providing these materials with a cell-mediated biodegradation mechanism[120]. The MMP-cleavable sequence is flanked by cysteine residues that provide free thiol groups that can participate in the Michael-addition crosslinking with PEG-MAL macromers to form 3D constructs. However, establishing peptide-crosslinked hydrogels as a generalizable tissue engineering platform suffers from a number of difficulties. These peptide sequences are cleaved by specific MMPs that are upregulated to different degrees across diverse pathological environments[120], and also feature highly variable levels across cellular subtypes[121] and patient populations[122]. Moreover, manufacturing peptides on the scale necessary to fabricate large tissue scaffolds is both inefficient and expensive with current strategies[37, 38]. This has motivated the development of synthetic biodegradable polymers to replace MMP-cleavable peptides in the formation of PEG-MAL hydrogels. The development of scalable,

affordably synthesized degradable polymers that target an abundant cell-mediated signal for polymeric degradation may provide a more translationally viable platform for cell delivery technologies.

To this end, we have developed polymers that are selectively degraded by cell-generated reactive oxygen species (ROS). Though produced in many normal biological signaling cascades[39], elevated ROS, or "oxidative stress", is a hallmark of disease states[40] and biomaterial implantation[44], making oxidative stress a promising candidate as a precise, cell-generated signal for triggering material degradation. This has motivated the recent emergence of new classes of ROS-responsive polymers[41], including poly(propylene sulfide) (PPS)[123, 142, 147, 150, 151], selenium-containing polymers[155, 267], arylboronic esters (ABEs)[171, 172], oligo(proline) peptide cross-linkers[187], and poly(thioketal) (PTK) polymers[30, 45, 124, 177, 178, 268]. Of these ROS-degradable systems, PTK polymer chemistry in particular possesses many ideal attributes for synthesizing large-scale tissue engineering materials, though until recently had solely been utilized in targeted nanoparticle formulations for drug delivery applications[45, 124, 177]. PTK polymers are synthesized by simple condensation polymerization of low-cost, low-toxicity precursors to form polymer chains that are inert to hydrolysis but specifically degraded by ROS[45]. Due to their ROS-specific degradation mechanism, PTK-based biomaterials more effectively match *in vivo* material degradation with tissue regeneration and foster more successful healing outcomes when compared to conventional polyester-based biodegradable implants[30, 268].

Further highlighting the utility of PTK materials as components of tissue engineering constructs, PTK polymer synthesis can be easily tuned to produce homobifunctional thiol end groups which can selectively react with the maleimide groups on PEG-MAL macromers. However, similarly to most ROS-degradable polymers currently in use, previously developed PTK polymers are relatively hydrophobic due to the non-polar units in the chemical backbone. This inherent polymer hydrophobicity hinders the employment of these PTK polymers in hydrogels since the water-insoluble PTK component cannot fully engage with the water-soluble PEG-MAL to form an effective covalent network. Herein, we have developed a fully water-soluble, thiolated PTK component that readily reacts with PEG-MAL macromers for the fabrication of hydrogels. These novel, covalently-linked PEG-MAL-PTK hydrogels are specifically degraded by cell-

generated ROS while retaining the benefits of previously reported PEG-MAL gels, serving to create a material platform with enhanced translational potential compared to conventional peptide-linked hydrogels.

5.2 Materials and methods

Materials

All chemicals and reagents were purchased from Sigma-Aldrich (Milwaukee, WI) except the following. Cobalt chloride hexahydrate, TCEP Disulfide Reducing Gel, calcein-AM, ethidium homodimer, and Tissue-Tek O.C.T. Compound were purchased from ThermoFisher Scientific (Waltham, MA). 10kDa four-arm PEG-maleimide (PEG-MAL) was obtained from Laysan Bio, Inc. (Arab, AL). The cysteine-terminated adhesive peptide GRGDSPC (RGD) was obtained from Genscript (Piscataway, NJ), while a GCRDVPMSMRGGDRCG peptide (VPM) was custom synthesized by Advanced Automated Peptide Protein Technologies (Louisville, KY). The fluorescent dye MTS-CF640R was purchased from Biotium (Fremont, CA). Cell culture reagents, including Dulbecco's Modified Eagle Medium (DMEM), fetal bovine serum (FBS), and penicillin/streptomycin were supplied by Gibco Cell Culture (Carlsbad, CA). Primary bone marrow-derived mouse mesenchymal stem cells (mMSCs) from C57BL/6 mice were obtained from Cyagen Biosciences, Inc. (Santa Clara, CA). CellTiter-Glo Luminescent Cell Viability Assay was purchased from Promega (Madison, WI). Male BALB/c mice were supplied by The Jackson Laboratory (Bar Harbor, ME).

EDDT-PTK Dithiol Synthesis

The protocol for PTK dithiol polymer synthesis has been previously outlined by our group[30, 43] and was adapted from Wilson, et al[45]. Briefly, 1 g of p-toluenesulphonic acid monohydrate (PTSA) was re-crystallized in HCl at -20°C, extracted and dried, and then added to a tri-neck boiling flask and put under positive nitrogen pressure. 1*x* molar equivalent (9.8mL) of 2,2'-(Ethylenedioxy) diethanethiol (EDDT) was added to the flask, while 0.83*x* molar equivalent (6.2mL) of 2,2-dimethoxy propane (DMP) was added to an additional funnel attached to the boiling flask. Anhydrous acetonitrile was charged into the flask

(100mL) and the addition funnel (50mL), and both were purged with flowing nitrogen for 30min at room temperature. Next, the flask was placed in an oil bath at 80°C, allowed to equilibrate for 15min, and the addition funnel was set so that the acetonitrile-DMP solution was added drop-wise into the continuously stirring boiling flask and allowed to react for 18h. Post synthesis, the acetonitrile was removed by rotary evaporation and the EDDT-PTK polymer was isolated by precipitation into cold ethanol and dried under vacuum. Polymer molecular weight was analyzed by gel permeation chromatography (GPC, Agilent Technologies, Santa Clara, CA) using a mobile phase of *N*,*N*-dimethylformamide (DMF) with 100mM LiBr and quantified using a calibration curve generated from poly(ethylene glycol) (PEG) standards (400 – 4000g/mol). The polymer composition was analyzed with ^{1}H nuclear magnetic resonance spectroscopy (NMR, Bruker 400 MHz Spectrometer). ^{1}H NMR chemical shifts were reported as δ values in ppm relative to the deuterated $CDCl_3$ (δ = 7.26): δ = 1.60 (6H), δ = 2.72 (2H), δ = 2.84 (4H), δ = 3.59-3.78 (8H).

PEG-MAL-PTK Macromer Synthesis

To improve the water-solubility of the synthesized EDDT-PTK polymer, a 4-arm PEG-MAL-PTK macromer was synthesized by combining thiolated PTK polymers with thiol-reactive PEG-MAL units. Briefly, 370mg of EDDT-PTK (8*x* molar equivalent) was added to a boiling flask and put under nitrogen. The PTK was dissolved in 25mL of anhydrous acetonitrile and then supplemented with 350µL of triethylamine (TEA) to deprotonate the polymer's thiol groups and increase the efficiency of the Michael addition reaction with the maleimide groups on PEG-MAL[111]. 500mg of 10kDa four-arm PEG-MAL (1*x* molar equivalent) was dissolved in 60mL of anhydrous acetonitrile and then slowly added to the stirring PTK solution at room temperature and allowed to react for 16h. Following synthesis, acetonitrile was removed by rotary evaporation and the crude product was dissolved in a small amount of dichloromethane (DCM) and precipitated into -80°C diethyl ether to remove unreacted EDDT-PTK. The precipitant was spun down at 3000 × g, after which the ether was removed and the precipitant was collected and dried. The final molecular weight of the PEG-MAL-PTK macromer was determined by GPC, and the chemical composition was determined by ^{1}H NMR in deuterated $CDCl_3$. The thiol content of the PEG-MAL-PTK

was determined by Ellman's assay to calculate the actual number of thiol groups per mass of polymer against the theoretical thiol content determined from GPC analysis of the macromer's molecular weight.

PEG-MAL Hydrogel Synthesis

Hydrogels formed from 10kDa 4-arm PEG-MAL macromers were fabricated by first separately pre-dissolving the PEG-MAL and respective thiolated crosslinking component (1:1 ratio of free thiols to maleimide groups) in phosphate buffered saline (PBS) supplemented with 4mM triethanolamine (TEOA)[93]. Three different thiolated crosslinkers were used in experiments: the synthesized PEG-MAL-PTK macromer, a commercially-available 1000Da PEG dithiol (PEG-dt), and an enzymatically-degradable VPM peptide (molecular weight 1697g/mol)[93, 120]. The PEG-MAL and the thiolated component solutions were then combined and allowed to solidify for 15min, though gelation began immediately following component mixing. The polymer weight percent (wt%) of these hydrogels was also varied (7.5 or 5 wt% in solution) to create hydrogels with different mechanical properties and swelling ratios.

Physical Characterization of PEG-MAL Hydrogels

Mechanical properties of PEG-MAL hydrogels fabricated with PTK or PEG-dt crosslinkers at both 7.5 and 5wt% were determined using parallel plate rheometry. Hydrogels were formed at a volume of 200μL per gel using chambers of a 24-well plate as a mold and allowed to solidify for 15min; after hardening, the hydrogels were incubated in deionized water for 16h to fully swell. Gels were removed from the plate and then placed between stainless steel 25mm plates on an AR-G2 rheometer (TA Instruments, New Castle, DE) using a plate gap of 500 μm. The shear storage modulus (G′) was determined over a frequency sweep from 0.1 to 10Hz at a strain of 1%. To determine the swelling ratio of PEG-MAL materials, 50μL hydrogels made at 7.5 and 5wt% from both PTK and PEG-dt crosslinkers were fabricated in the wells of 96-well plates, hardened for 15min, and then allowed to swell in deionized water for 16h. The incubating liquid was removed from each hydrogel before weighing each sample to determine the swollen wet weight. Gel samples were then frozen and lyophilized; the dried gel samples were weighed

again to determine the dry weight, with the ratio of wet weight to dry weight determining the swelling ratio values. This metric is given in Equation 2.

$$Hydrogel\ Swelling\ Ratio\ (SR)\ = \frac{Weight_{WET}}{Weight_{DRY}}$$

Equation 2. Swelling ratio determination for PEG-MAL hydrogels.

In Vitro Degradation of PEG-MAL Hydrogels

50μL hydrogels made at 7.5 and 5wt% from both PTK and PEG-dt crosslinkers were fabricated and incubated in deionized water or varying concentrations of hydrogen peroxide (H_2O_2) with added cobalt chloride ($CoCl_2$) to spur the generation of hydroxyl radicals[228]. Hydrogel samples were incubated in 1mL of 65mM H_2O_2 (1mM $CoCl_2$), 25mM H_2O_2 (0.39mM $CoCl_2$), 5mM H_2O_2 (77μM $CoCl_2$), or deionized water with daily degradation media changes for up to seven days. Three independent gel samples per formulation were used for each time point. At each final time point, the degradation media was removed from each hydrogel sample before determining each sample's wet and dry weights and subsequent swelling ratio value. To corroborate the swelling ratio data for hydrogel degradation, 200μL hydrogel samples were also fabricated and incubated in the same degradation media and characterized by rheometry as previously described.

Cell Encapsulation in PEG-MAL Hydrogels

Hydrogel precursor components (PEG-MAL, PEG-dt, PEG-MAL-PTK, and VPM peptide) for 50μL gels at both 7.5 and 5wt% were all dissolved in sterile PBS supplemented with 4mM TEOA. All components were dissolved at 2*x* their normal concentration for hydrogel formation to allow for the addition of RGD peptide and cell suspension solutions to give a final 50μL hydrogel volume. The PEG-MAL was reacted with cysteine-terminated RGD peptide (dissolved in sterile PBS) for 15min; to give a final RGD concentration of 2mM in each gel sample, 69μg of RGD (dissolved at 7mg/mL) was added per hydrogel. This RGD concentration theoretically consumes 9% and 14% of MAL groups in 7.5 and 5wt% gels,

respectively, and the complete reaction of these two groups had been previously validated using an Ellman's assay to check for free thiols after component mixing. Next, minimally-passaged mouse MSCs seeded in cell culture flasks (less than 80% confluence) were trypsinized and concentrated to $7e^6$ cells/mL in order to minimize the liquid volume that must be added to the hydrogel precursor solutions. An aliquot of this cell suspension (enough to give $7e^4$ cells per 50μL gel) was then mixed with each thiolated component solution and added to its respective RGD-PEG-MAL solution in a 96-well plate and allowed to solidify in a cell culture incubator for 20min. After complete gelation was achieved, 200μL of cell culture medium comprised of DMEM with 1g/L glucose, 20% FBS, and 1% penicillin/streptomycin was added on top of each gel. The hydrogel-encapsulated cells were cultured for 72h with daily media changes. To evaluate the morphology and relative viability of encapsulated cells, the culture media was removed from the gels and they were washed three times with PBS before being stained with PBS containing 2μM calcein-AM and 4μM ethidium homodimer for 40min. Hydrogels with live/dead stained cells were removed from their plate, sandwiched between glass coverslips, and then imaged with a Zeiss LSM 710 confocal microscope (Oberkochen, Germany) across multiple z-slices and represented with a maximum intensity projection across the z-planes. Finally, to quantify the overall number of viable cells encapsulated in all the hydrogel formulations after 72h of culture, 50μL gels with incorporated cells were incubated in 100μL PBS and treated with 100μL of CellTiter-Glo reagent for 10min while being vigorously disrupted with a pipette tip to ensure complete diffusion of the CellTiter-Glo throughout each gel sample. The luminescent signal per hydrogel sample, corresponding with the number of encapsulated viable cells, was then quantified with an IVIS Lumina III (Xenogen, Alameda, CA).

In Vivo Degradation and Tissue Response of PEG-MAL Hydrogels Implanted Subcutaneously in Mice

50μL hydrogels made at 7.5wt% using PEG-MAL and the three thiolated crosslinkers (VPM peptide, PEG-dt, and PEG-MAL-PTK) were fabricated with a covalently conjugated fluorescent dye to allow for *in vivo* quantification of hydrogel persistence. The fluorescent probe MTS-CF640R, which features a methanethiosulfonate (MTS) group connected to the fluorescent molecule CF640R by a disulfide bond,

was dissolved in sterile water (2.5mg/mL) and incubated with TCEP disulfide reducing gel for 1h following the manufacturers protocol to cleave the disulfide-conjugated MTS group from the probe molecule. Following incubation, the dye/TCEP slurry was transferred to a centrifugal spin cup and centrifuged at 50 × g for 1min to remove the dye solution from the TCEP gel. The slurry was re-suspended in sterile water and the centrifugation dye extraction was repeated 5*x* to remove the majority of the fluorescent probe from the TCEP gel. The disulfide-reduced CF640R dye was then frozen, lyophilized, and reconstituted in sterile PBS with 4mM TEOA. An Ellman's assay was performed on the CF640R dye solution to confirm that free thiol group had been generated from the MTS disulfide reduction.

To prepare dye-conjugated hydrogels, the PEG-MAL component was dissolved at 4*x* the normal concentration in sterile PBS with 4mM TEOA for gel fabrication. Next, CF640R dye (0.75mg/mL to create a final dye concentration of 85μM dye per 50μL hydrogel sample) was mixed with the PEG-MAL solutions and allowed to react for 15min. As previously described, dissolved RGD (2mM RGD per 50μL gel) then was added to the CF640R/PEG-MAL solution and reacted for an additional 15min. Finally, each thiolated crosslinker was dissolved in sterile PBS with 4mM TEOA and added to its respective RGD/CF640R/PEG-MAL solution in the chambers of a 96-well plate and allowed to solidify for 20min. Once the dye-conjugated hydrogels were successfully fabricated, they were removed from the plate and implanted subcutaneously in male BALB/c mice (n=6 mice, overall n=8 individual gels per formulation). Following implantation, the mice were imaged with an IVIS system using 620/670 emission/excitation for a baseline measurement of hydrogel fluorescence and subsequently imaged over time. Half the mouse cohort was euthanized at 15 post-surgery while the other half were euthanized at day 35.

Statistical Analysis

All data are reported as the mean and standard error of the mean unless otherwise indicated. Statistical analysis was performed using Student's t-test for single comparisons or single factor analysis of variance (ANOVA) and Tukey post-hoc tests for multiple comparisons. *P*-values less than 0.05 were considered statistically significant.

5.3 Results

EDDT-PTK and PEG-MAL-PTK Synthesis and Characterization

An EDDT-PTK dithiol polymer was successfully synthesized from the condensation polymerization of EDDT and DMP using a PTSA catalyst (Figure 19) and characterized by GPC and NMR as shown in Figure 20 and Table 3. Following purification, the EDDT-PTK dithiol polymer was combined with a thiol-reactive 10kDa 4-arm PEG-MAL to conjugate PTK polymers onto each arm of the branched PEG as demonstrated in Figure 19. The final product was purified and then characterized by GPC and NMR (Figure 20 and Table 3). GPC chromatograms indicate an increase in molecular weight for the PEG-MAL-PTK compared to the parent PEG-MAL, and NMR spectra of both the precursor components and the final product further confirm successful conjugation as both EDDT-PTK and PEG-MAL characteristic peaks are present in the PEG-MAL-PTK spectra (Figure 20). GPC quantification of these polymers' number average molecular weights (M_n, g/mol) strongly agree with theoretical values (Table 3), and Ellman's assay quantification of the thiol content of the final PEG-MAL-PTK product further indicates that a 4-arm tetrathiol macromer was produced.

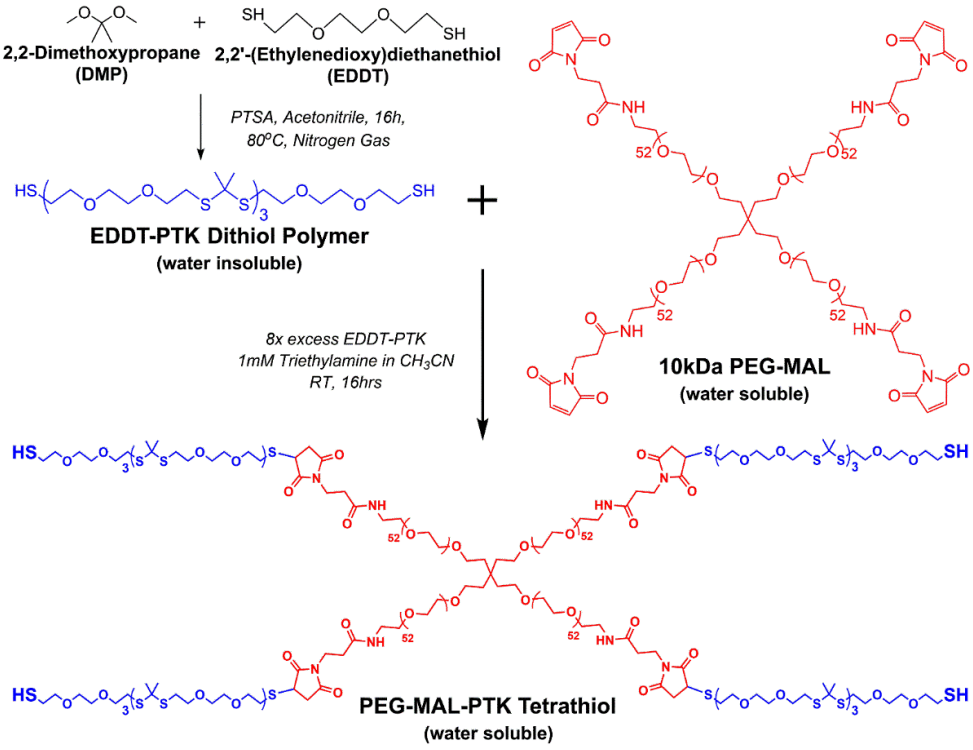

Figure 19. Synthesis schemes for the EDDT-PTK dithiol polymer and the PEG-MAL-PTK macromer.

Physical Characterization of PEG-MAL Hydrogels

Hydrogels made from PEG-MAL and either a 1000Da PEG dithiol polymer (PEG-dt) or the PEG-MAL-PTK macromer were fabricated at both 7.5 and 5wt%. The swelling ratio of hydrogel samples was evaluated from the ratio of each gel's water-swollen weight divided by the weight of only the dried solid components (Equation 2). The 5wt% hydrogel samples were significantly more swollen than 7.5wt% gels for both formulations (Figure A18A), though PTK-based gels were less swollen than hydrogels made with PEG-dt. The mechanical properties of PEG-dt and PTK hydrogel formulations at both 7.5 and 5wt% were also measured by rheometry. Taken from a frequency sweep of the storage modulus G′, the stiffness of 7.5wt% PEG-dt gels was nearly 1000Pa while 7.5wt% PTK gels were closer to 700Pa (Figure A18B). The lower wt% samples had correspondingly lower modulus values with 5wt% PEG-dt gels around 500Pa and 5wt% PTK gels near 300Pa as shown in Figure A18C.

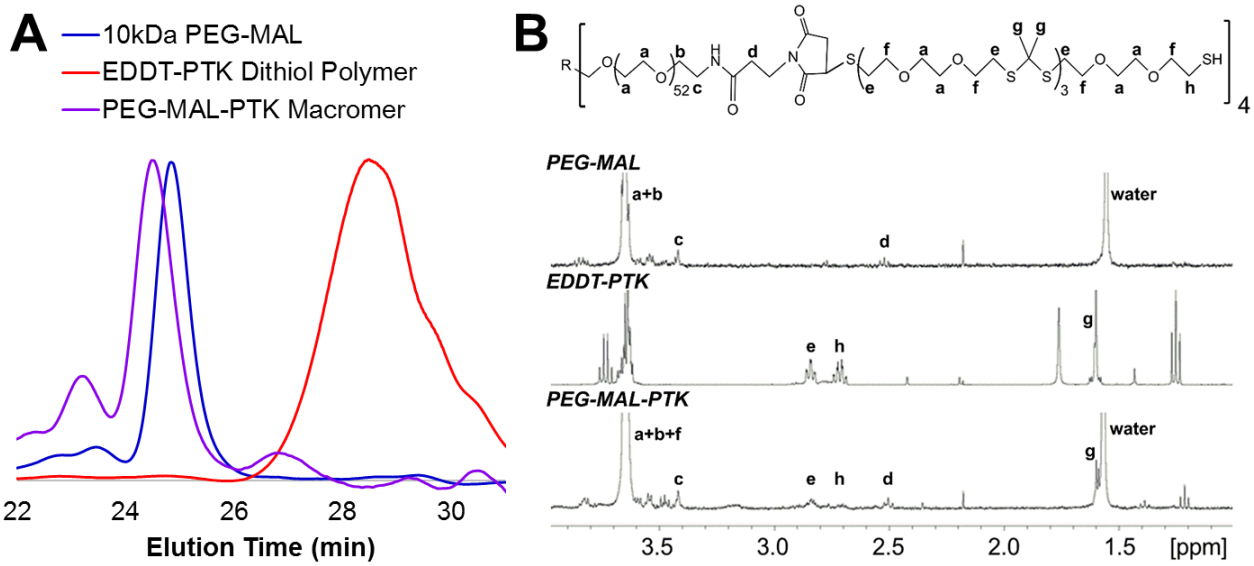

Figure 20. Polymer characterization by GPC and NMR. (A) GPC chromatograms indicating a shift towards higher molecular weight with PTK conjugation to PEG-MAL. (B) NMR spectra of PEG-MAL-PTK shows the appearance of characteristic peaks from both PTK and PEG-MAL polymers, indicating successful conjugation.

In Vitro Degradation of PEG-MAL Hydrogels under Oxidative and Non-Oxidative Conditions

PEG-MAL hydrogels made with PEG-dt or PEG-MAL-PTK crosslinkers at both 7.5 and 5wt% were incubated in media containing different concentrations of ROS to assess *in vitro* degradation of these materials. Gel samples were treated with either deionized water, 5mM H_2O_2 with 77μM $CoCl_2$, 25mM H_2O_2 with 0.39mM $CoCl_2$, or 65mM H_2O_2 with 1mM $CoCl_2$ for up to seven days and then weighed (wet and dry) to assess their swelling ratios as an indicator of degradation[67]. As shown in Figure 21, both 7.5 and 5wt% PTK-based hydrogels have significantly greater swelling after treatment with varying doses of the H_2O_2 compared to H_2O_2-treated samples made with the PEG-dt crosslinker. PTK gels in 65mM H_2O_2 were only taken out to day 3 as samples incubated for longer times were completely degraded past this time point. Hydrogel samples made with PEG-dt were also minimally susceptible to ROS-mediated degradation as samples incubated in the 25mM H_2O_2 did have increased swelling ratio values at day 7 compared to samples incubated in water. Additionally, PTK gels at both 7.5 and 5wt% display dose-responsive degradation as their swelling ratios increase at a faster rate in higher concentrations of H_2O_2, though 5wt% samples were minimally responsive at the lowest 5mM H_2O_2 concentration compared to PEG-dt samples. To confirm these degradation results seen with swelling ratio assessment, hydrogels made with both crosslinkers at 7.5 and 5wt% were incubated in the 65mM H_2O_2 media for three days and then characterized by rheometry. Both PEG-dt and PTK gel samples had decreased G′ values after incubation with the ROS media compared to day 0 values (Figure A18B-C), but PTK samples had a more substantial decrease in modulus values and mechanical integrity.

Table 3. Polymer characterization values.

Polymer	***Theoretical M_n***	***GPC M_n***	***Thiol Content M_n***
EDDT-PTK	850	875	-
10kDa PEG-MAL	11000	10595	-
PEG-MAL-PTK	14400	15890	14000

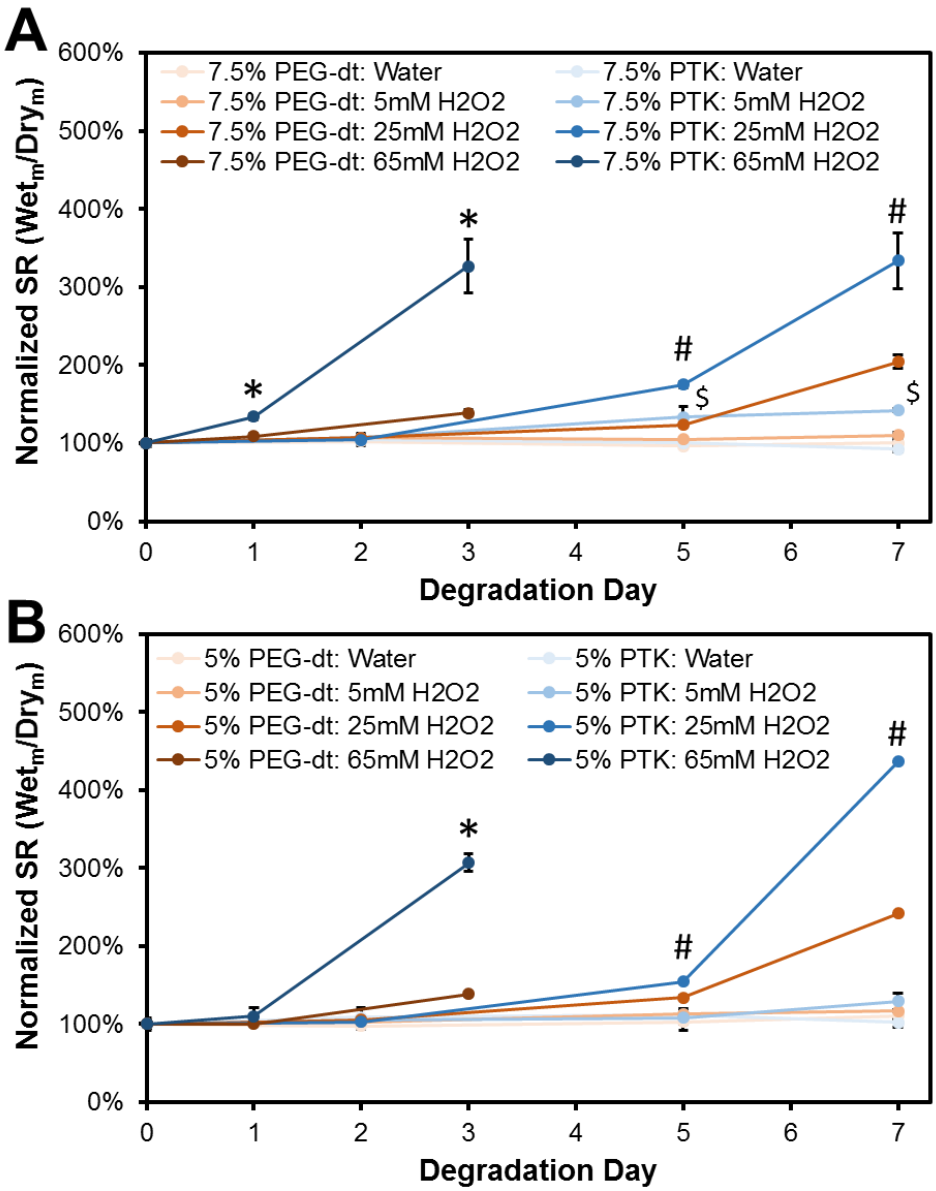

Figure 21. *In vitro* degradation of PEG-MAL hydrogels formed with PEG-dt or PTK crosslinkers. As assessed by the gel swelling ratio, (A) 7.5wt% PTK hydrogel samples display significantly more dose-responsive H_2O_2 degradation compared to PEG-dt hydrogels. (B) 5wt% PTK hydrogels also degrade in response to H_2O_2 levels but are not significantly different at 5mM unlike 7.5wt% samples. *65mM H_2O_2, $^{\#}$25mM H_2O_2, $^{\$}$5mM H_2O_2 denotes $p<0.05$ significance for PEG-dt vs. PTK comparison, n=3 samples per treatment.

Encapsulation and Cytocompatibility of MSCs in PEG-MAL Hydrogels

Mouse mesenchymal stem cells (mMSCs) were encapsulated in 7.5 and 5wt% PEG-MAL hydrogels made with either PEG-dt, PEG-MAL-PTK, or VPM peptide crosslinkers and cultured for three days. All hydrogels were also covalently tethered with 2mM RGD adhesive peptide to encourage cell attachment to the materials. As shown in Figure 22A, maximum intensity projections of multiple z-slices

from fluorescent confocal microscopy demonstrate that mMSCs were successfully encapsulated into the different hydrogel formulations and maintained their viability over three days in culture as indicated by characteristic calcein-AM green staining. Furthermore, the encapsulated mMSCs were evenly distributed in the 3D matrix and demonstrated significant spreading in all the different hydrogel formulations. In particular, cells in the 5wt% VPM and PTK hydrogels demonstrate high levels of cell spreading compared to the other gel formulations, and this finding is validated in a whole-sample measurement of viable cell number as shown in Figure 22B. The 5wt% VPM and PTK hydrogels contain a significantly higher number of viable cells than 5wt% PEG-dt samples, even as the 5wt% PTK hydrogels also contain a significantly higher number of cells than the gel samples featuring the well-validated VPM crosslinking peptide (Figure 22B). The 7.5wt% formulations had statistically similar numbers of viable mMSCs encapsulated as shown in Figure 22B.

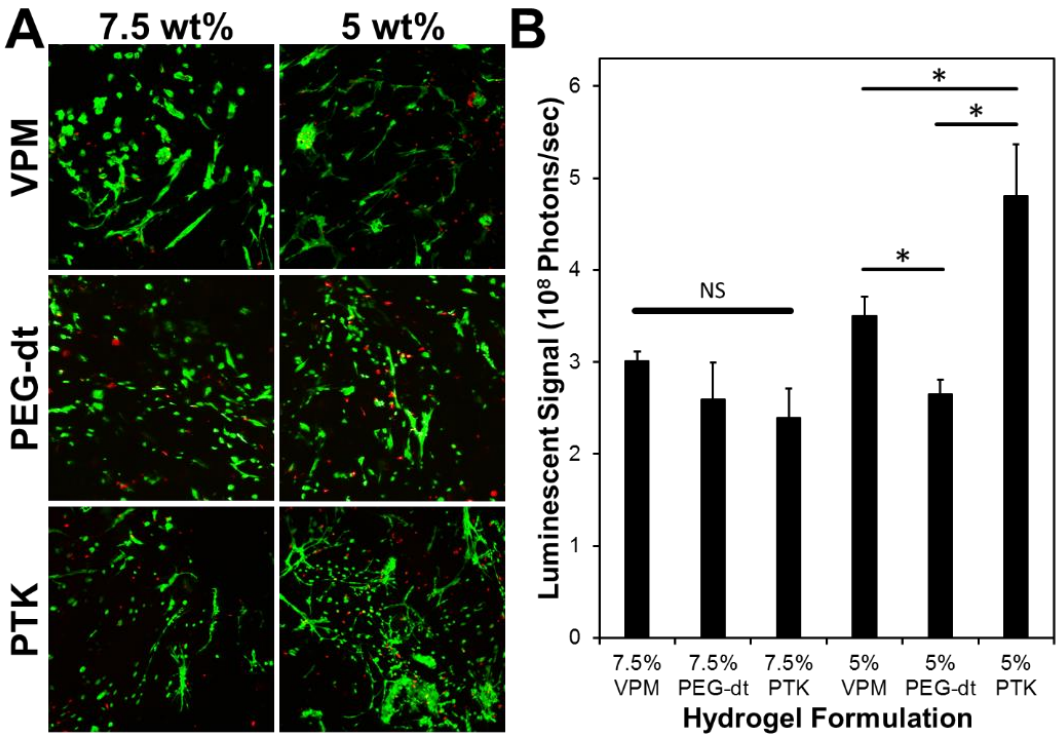

Figure 22. Mouse MSCs encapsulated in both 7.5 and 5wt% PEG-MAL hydrogels (A) maintain a high level of viability and cell spreading as assessed by live/dead staining, though spreading is particularly enhanced in 5wt% samples made with degradable VPM and PTK crosslinkers. (B) Quantification of total viable cell number per gel sample, as assessed through a CellTiter-Glo luminescent readout, indicates that cell viability is not significantly different between formulations at 7.5wt%. But, 5wt% VPM gels have significantly more viable cells than PEG-dt gels while 5wt% PTK gels have significantly more viable cells than both 5wt% VPM and PEG-dt samples. N=3 samples per formulation, *$p<0.05$.

In Vivo Degradation of PEG-MAL Hydrogels in Mouse Subcutaneous Implants

4-arm PEG-MAL polymers were pre-labeled with a thiol-terminated CF640R fluorescent dye and an RGD adhesive peptide and then used to fabricate 7.5wt% hydrogels made with PEG-dt, PEG-MAL-PTK, and VPM peptide crosslinkers. The fluorescently-labeled hydrogels were then implanted into ventral subcutaneous pockets in male BALB/c mice; the hydrogel-associated fluorescent signal from each implanted sample was measured at day 0 using an IVIS imaging system to obtain baseline gel signal values and then quantified over time to determine material retention at the implantation site. As shown in Figure 23, both the PEG-dt and PTK hydrogels have significantly less fluorescent signal than the VPM samples over the first few days following implantation. However, the PEG-dt and VPM gel signals converge following this initial stage and are statistically equivalent for the remainder of the time course. The PTK hydrogels continue a relatively steady decrease in their fluorescent signal over time and have statistically lower values than both PEG-dt and VPM implants after day 11 until day 35.

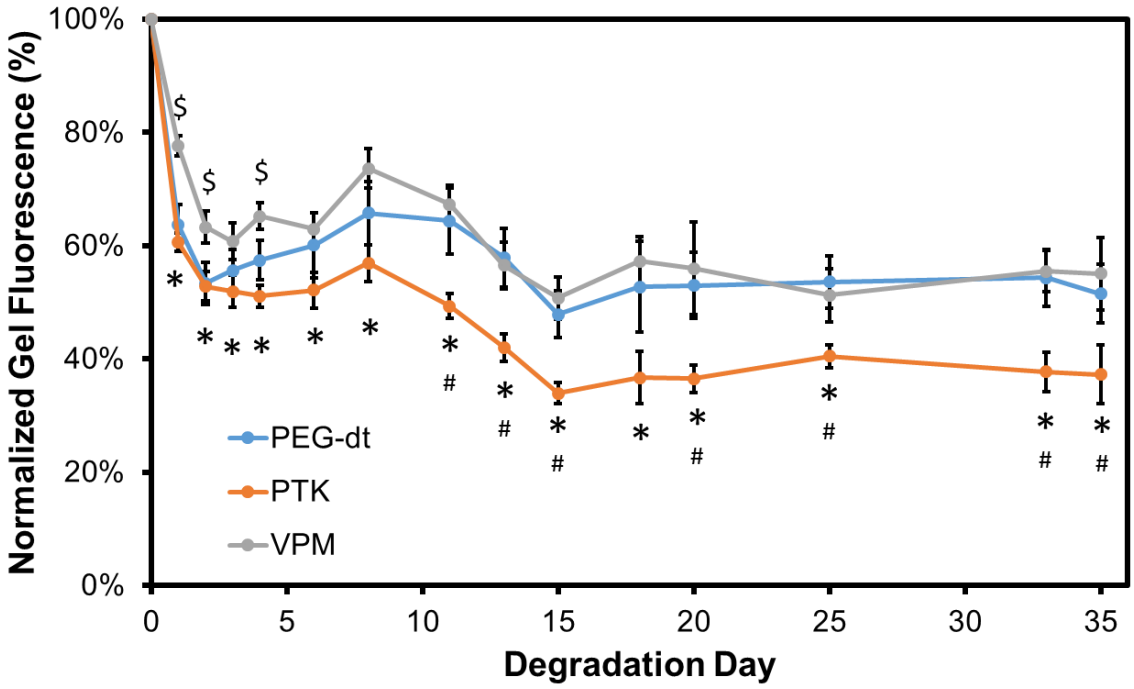

Figure 23. *In vivo* degradation of fluorescently-labeled PEG-MAL hydrogels. Degradation of PTK gels is significantly faster than VPM gels across all time points tested (*p<0.05) and is also significantly faster than PEG-dt gel degradation after 11 days ($^{\#}$p<0.05). The PEG-dt gels degrade significantly faster than VPM gels initially ($^{\$}$p<0.05) but are statistically equal after 4 days of implantation. N=8 samples until day 15, n=4 samples afterwards.

5.4 Discussion

Injectable, *in situ*-forming PEG-based hydrogels represent an extremely promising class of synthetic biomaterial due to their minimally-invasive delivery, ease of functionalization, and inherent biocompatibility[88]. Injectable hydrogels formed from PEG-MAL macromers are particularly exciting due to their high gelation efficiency and amenability for *in vivo* cell and drug delivery. Like many injectable hydrogels, current PEG-MAL gels derive their biodegradability from the incorporation of enzymatically-degradable peptide cross-linkers into their covalent network[93, 94]. While these hydrogels and other similar materials achieve cell-mediated biodegradation[115, 120, 269], the expenses of synthesizing peptides in quantities large enough to create large-scale tissue engineering materials will most likely limit these materials' clinical usefulness[37, 38]. Therefore, creating a cost-effective, synthetic, cell-degradable crosslinker to replace peptides in the formation of PEG-MAL hydrogels would greatly enhance the translatability of these materials. To this end, we have synthesized water-soluble PTK polymers that are easily synthesized, feature terminal thiol end-chemistries, and successfully couple with PEG-MAL units to form covalently-linked networks. Previous work has demonstrated synthetic PTK polymers' potential for creating cell-degradable materials[30, 45, 124, 177, 178, 268]; these novel PEG-MAL-PTK materials represent the first development of a covalently-tethered hydrogel that is specifically degraded by cell-generated ROS while maintaining the benefits of previous PEG-MAL gels.

Initial efforts in trying to synthesize a water-soluble PTK polymer were pursued using the same previously utilized condensation polymerization schemes for PTK synthesis[45] but utilizing more hydrophilic ethylene glycol (EG)-based dithiol monomers to increase the water-solubility of the final polymer (Figure A19). Dithiol monomers featuring 1, 2, 5, and 12 EG units were first used in attempts to synthesize water-soluble PTK polymers, with only the 12-EG dithiol monomer (600g/mol) yielding a polymer that dissolved in aqueous solutions. However, the 12-EG-PTK polymer also did not possess appropriate thiol end groups and only had a polymerization degree of two, yielding a polymer that did not form hydrogels with PEG-MAL, featured an inefficient condensation reaction, and was very difficult to purify due to the relatively small difference in monomer and polymer molecular weight. Interestingly, the

1 and 2-EG dithiol monomers both polymerized effectively (polymerization degrees > 3), potentially signifying that the PTK condensation polymerization under these reaction conditions is most effective using relatively small (<200g/mol) dithiol monomers. Unfortunately, PTK polymers made from 1 and 2-EG monomers were both hydrophobic; since the 2-EG dithiol monomer (EDDT) is more hydrophilic than the 1-EG monomer, EDDT-PTK polymers were pursued in the further fabrication of water-soluble PEG-MAL-PTK macromers as outlined in Figure 19.

To encourage a fast conjugation of EDDT-PTK polymers to PEG-MAL units while limiting uncontrolled crosslinking of multiple PEG-MAL groups, three strategic aspects were incorporated into the synthesis of PEG-MAL-PTK macromers: using an eight-fold molar excess of PTK to PEG-MAL (two-fold molar excess of EDDT-PTK polymers to each maleimide-terminated arm of the PEG macromer), diluting the concentration of PEG-MAL compared to the more highly concentrated PTK, and using a slow, drop-wise addition to apply PEG-MAL to the PTK solution. These synthetic protocol features were all designed to quickly react single thiol groups on different EDDT-PTK polymers with the four arms of more dilute PEG-MAL, thereby rapidly consuming all the available maleimide groups on single PEG-MAL units (Figure 20A). This approach spares the thiol group on the unconjugated end of each attached PTK polymer, generating a four-arm PEG-MAL-PTK macromer with terminal sulfhydryl groups (Table 3) that are free to participate in future thiol-ene reactions. The large hydrophilic PEG component of the macromer (10,000Da PEG vs. 3400Da PTK) pushes the entire polymer into aqueous solubility despite the hydrophobic PTK content and makes the water-soluble PEG-MAL-PTK tetrathiol amenable to hydrogel formation. Moreover, any excess EDDT-PTK is easily purified from the hydrophilic PEG-MAL-PTK macromer by precipitation of the macromer into diethyl ether (Figure 20A).

Hydrogels fabricated using the PEG-MAL-PTK macromers were directly compared against control hydrogels made with the same PEG-MAL but utilizing a commercially-available 1000Da PEG dithiol (PEG-dt) to determine these materials' physical attributes and degradation properties *in vitro.* The PEG-dt features the same ethylene glycol units that comprise most of the EDDT-PTK's polymeric backbone but does not contain the ROS-sensitive thioketal moiety. Unsurprisingly due to the decreased crosslink density,

it was found that 5wt% hydrogels were significantly more swollen than 7.5wt% samples for both formulations (Figure A18A). However, PTK-crosslinked hydrogels were also less swollen than PEG-dt samples at both 7.5 and 5wt% (Figure A18A) most likely due to the incorporation of the hydrophobic EDDT-PTK component into the hydrogel's 3D matrix. Rheometry of both PTK and PEG-dt hydrogels revealed a similar trend as the PTK materials had decreased modulus values compared to PEG-dt gels. Both hydrogel formulations experienced a roughly 2*x* decrease in stiffness values when decreasing from 7.5 to 5wt%, displaying the mechanical tunability of this biomaterial system. Moreover, assuming the Poisson's ratio of these hydrogels is around 0.5, the Elastic modulus of these hydrogels is approximately three times higher than the G′ storage modulus[270]. Given that these hydrogels range between 1000 and 300Pa for G′ values, it can be assumed these materials have Elastic moduli values between 1-3kPa, well in line with previously cited PEG hydrogel systems used for cell delivery[93, 271].

When placed in degradation media containing H_2O_2 and hydroxyl radical-generating $CoCl_2$, it was found that the swelling ratio of PTK hydrogels significantly increased compared to the PEG-dt samples at both 7.5 and 5wt% as displayed in Figure 21. Both PEG-dt and PTK hydrogels incubated in water over the same time frame were also unchanged over the same time period, signifying the selective ROS-mediated degradation of thioketal bonds in the PTK crosslinks and the overall breakdown of these samples as seen in other thioketal-based biomaterials[177, 268]. These hydrogel degradation data were also confirmed by rheometric mechanical testing of gel samples incubated in 65mM H_2O_2 for three days (Figure A18B-C). In agreement with swelling ratio degradation data (Figure 21), PTK hydrogels had decreased G′ values compared to PEG-dt samples as demonstrated in Figure A18B-C. Though to a significantly lesser degree than seen in the PTK hydrogels, the PEG-dt samples were also somewhat sensitive to the ROS media compared to water (Figure 21, Figure A18B-C), potentially indicating ROS-mediated degradation of ether bonds in the PEG-dt crosslinker or the PEG-MAL macromer. Ether bonds have well known susceptibility to ROS, particularly hydroxyl radicals[228], though the ROS-mediated degradation of thioketal groups is significantly faster than covalent ether bond cleavage in biomaterials[30]. However, these data further indicate that the PEG-dt crosslinked hydrogels, and PEG-based materials in general[272], should be

considered “minimally-degradable” as opposed to “non-degradable” due to ether bond sensitivity to ROS over longer time-frames.

Injectable PEG hydrogels are particularly useful as cell-delivery vehicles due to a number of factors, but chiefly *in situ* gelation which encapsulates and protects cells after deployment of the hydrogel solution. Furthermore, PEG’s lack of protein adsorption[90] means that these materials can be specifically functionalized with chemical motifs to affect the behavior of encapsulated cells. In particular, RGD-based peptides are particularly effective at promoting cell viability and spreading within PEG hydrogels[92, 273]. As a proof of concept, mouse MSCs were encapsulated in RGD-containing 7.5 and 5wt% PEG-MAL hydrogels made with PEG-dt, PEG-MAL-PTK, and VPM peptide crosslinkers and cultured for 72h. PEG-MAL hydrogels made with RGD and VPM crosslinkers are non-cytotoxic and promote robust cellular attachment[93, 94], making these materials a benchmark for cellular encapsulation applications. MSCs embedded in 7.5wt% gel samples achieved statistically similar viability levels across all three hydrogel formulations (Figure 22B), and roughly similar levels of cell spreading as qualitatively assessed from fluorescent microscopy images in Figure 22A. However, MSCs encapsulated in 5wt% PTK hydrogels had a significantly higher signal from viable cells than both 5wt% VPM and PEG-dt samples, while the VPM cell signal was also significantly higher than PEG-dt (Figure 22B). These results are reflected in the microscopy images in Figure 22A as the encapsulated cells in 5wt% VPM and PTK gels were notably more spread through the hydrogel matrix compared to cells in 5wt% PEG-dt samples. These collective data, in accordance with previous reports[93], indicate that the higher crosslinking density of 7.5wt% hydrogels limits spreading and expansion of encapsulated MSCs, while lower wt% hydrogels with a degradable crosslinker (VPM or PTK) allow for greater cellular trafficking through the matrix compared to the minimally degradable PEG-dt samples. The higher viable cell signal seen in 5wt% PTK hydrogels compared to the corresponding VPM samples further justifies the usage of these novel, ROS-degradable materials for cell delivery applications due to their enhanced cellular performance compared to a “gold-standard” biomaterial.

Fluorescently-labeled biomaterials have been previously used for the longitudinal evaluation of *in vivo* hydrogel degradation[274-276], and this strategy was employed here to track the degradation of 7.5wt% PEG-MAL gels made with the three previously utilized crosslinking groups. Instead of labeling the RGD peptide or thiolated crosslinker, the PEG-MAL was pre-conjugated with a thiol-terminated fluorescent probe to collect the most accurate determination of hydrogel degradation since the PEG-MAL component makes up the majority of the gel and the multi-armed PEG more effectively integrates the probe into the bulk of the hydrogel. All three fluorescently-labeled hydrogel formulations implanted subcutaneously in mice had decreased signals over time as seen in Figure 23, though the PTK hydrogels had significantly lower signal compared to VPM samples across the entire time course and also had significantly lower values compared to PEG-dt gels after day 11. Though some of the early decrease in the fluorescent hydrogel signal is likely due to loss of poorly conjugated dye, the PTK hydrogels lose their fluorescent signal at a faster rate than PEG-dt or VPM samples even after the initial burst of signal reduction. These data indicate that PTK hydrogels undergo more substantial *in vivo* degradation than MMP-degradable peptides, suggesting that targeting cell-generated ROS as a mediator of *in vivo* biomaterial breakdown could be a more effective strategy than utilizing protease-degradable systems.

5.5 Conclusion

We have successfully developed a PEG-based hydrogel that is crosslinked with ROS-degradable PTK polymers. These are the first reported hydrogels to feature water-soluble PTK macromers, with these novel, easily-synthesized hydrophilic PTK units possessing terminal thiol groups that allow for covalent bonding with maleimide-capped, multi-armed PEG molecules for hydrogel fabrication. PTK hydrogels are mechanically robust and undergo ROS-mediated, dose dependent degradation *in vitro*, while PEG hydrogels without PTK units are only minimally affected by ROS. Furthermore, mesenchymal stem cells were successfully encapsulated in PTK hydrogels and maintained their viability in 7.5wt% gels at comparable levels to cells encapsulated in benchmark hydrogels crosslinked with an enzymatically-degradable peptide. However, MSCs encapsulated in less tightly bound 5wt% hydrogels maintained

significantly more viable cells in PTK gels than peptide-linked materials, indicating that PTK hydrogels perform better as cell delivery vehicles than enzymatically-degradable materials. Finally, fluorescently-labeled PTK hydrogels subcutaneously implanted in mice underwent significantly faster degradation *in vivo* compared to minimally-degradable PEG gels or enzymatically-degradable hydrogel implants. These *in vivo* data demonstrate that PTK hydrogels undergo significant degradation following implantation and that ROS could be a more potent cell-generated signal for triggering material degradation than conventionally-used enzymatic activity. Together, these results represent a paradigm shift in the creation of biodegradable hydrogels due to the enhanced performance of ROS-degradable PTK hydrogels in comparison to conventional benchmark materials, and further motivates the continued exploration of these novel materials for clinically-translatable applications.

CHAPTER 6

Synopsis and Future Directions

6.1 Summary

With the increasing prevalence of diabetes and the corresponding increase in non-healing wounds arising from diabetic complications, there is a growing need for therapies that correct and treat these chronic wound pathologies. Biodegradable implants that enhance the local healing response while also serving as a depot for sustained, localized drug delivery could help improve outcomes for patients with these persistent lesions. However, currently developed materials that undergo *in vivo* biodegradation can suffer from a number of shortcomings, including material degradation kinetics that are misaligned with tissue regeneration rates and prohibitively expensive material components that limit economic feasibility of the implants in the clinic. Cheaply-synthesized poly(thioketal) (PTK) polymers that are biocompatible and specifically degraded by cell-generated reactive oxygen species (ROS) address these concerns and represent a promising material platform for fabricating new classes of biomaterials. These studies set out to develop PTK-based biomaterials in both hydrophobic and hydrophilic formats, and demonstrated the utility of these novel materials as therapeutic delivery vehicles that can enhance wound healing.

In Aim 1, a family of PTK polymers was synthesized by condensation polymerization and incorporated into PTK-urethane (PTK-UR) scaffolds. These PTK-UR materials were compared against conventional, heavily investigated poly(ester-urethane) scaffolds and were found to have similar cytotoxicity profiles. However, PTK-URs were more mechanically robust despite having a lower crosslink density than PEURs and were completely inert to hydrolytic degradation unlike the ester-containing PEUR materials. Moreover, PTK-UR scaffolds were significantly degraded by ROS in a dose-dependent fashion, demonstrating the ROS-specific degradation mechanism of these new scaffold materials.

In Aim 2, PTK-UR scaffolds were utilized in a number of animal models to determine their *in vivo* degradability and potential as drug delivery vehicles. PTK-URs underwent controlled, 1st-order

degradation kinetics when implanted subcutaneously in rats while PEUR scaffolds experienced accelerated, autocatalytic degradation over the same time period. PTK-UR scaffolds also promoted more robust tissue regeneration than benchmark PEURs when implanted in excisional diabetic rat wounds. Additionally, PTK-UR scaffolds were able to load nanoparticles carrying small interfering RNA (siRNA) and release this drug payload *in vivo* to silence the expression of the angiogenesis regulator prolyl hydroxylase domain protein 2 (PHD2). The reduction in PHD2 activity led to an increase in blood vessel formation, cell proliferation, and overall wound healing in these diabetic wounds.

Aim 3 sought to take PTK polymer chemistry and apply it for the fabrication of hydrogels. Hydrophobic PTK polymers were combined with a maleimide-terminated, 4-arm poly(ethylene glycol) (PEG-MAL) molecule to create water-soluble PEG-MAL-PTK macromers. These novel, hydrophilic PTKs were then formulated with additional PEG-MAL polymers to form robust PTK hydrogels that were selectively degraded by ROS. These PTK hydrogels better maintained viable mesenchymal stem cells than benchmark peptide-crosslinked gels in *in vitro* culture, and PTK-based gels also underwent significantly faster *in vivo* degradation in subcutaneous mouse wounds than the enzymatically-degradable peptide hydrogels.

Together, these results show that synthetic PTK polymers can be easily fabricated into a number of biomaterial platforms that are amenable to both cell and drug delivery to serve as regenerative constructs for the treatment of chronic wounds.

6.2 Concerns and limitations

Though the biomaterials developed in these studies were tested for cytotoxicity and *in vivo* biocompatibility in rodent models, it is important to note that evaluating the immune response to PTK-based materials implanted over long periods of time presents major considerations for the clinical translation of PTK biomaterials in wound healing applications. It is anticipated that these potential hurdles can be overcome with proper *in vitro* screening efforts and appropriate use of preclinical animal models.

Though PTK-UR scaffolds implanted in either subcutaneous or excisional wounds in rats did not elicit any obvious deleterious immune responses as assessed by histology (Figure 13, Figure 15), it is well

understood that rodent skin wounds poorly model wounds in human patients[277]. As such, the favorable biological response to these implants in rodents could be drastically different in actual patients. To address these concerns, we have recently begun studies to evaluate the *in vivo* tissue response to implanted PTK-UR scaffolds in a novel model of impaired wound healing in pigs (see section 6.4 and Figure A21). Pig skin wounds are more similar to those seen in humans and are considered the "gold-standard" preclinical model for wound healing evaluation. As seen in trichrome histology images, PTK-UR implants made with either LTI or HDIt isocyanate chemistries have robust granulation tissue formation at day 10 and appear to be healing similarly to implants in excisional rat wounds (Figure A23A). However, at day 28 post surgery the scaffold remnants seem to have elicited an abnormal healing response as indicated by the bright-red, cell-dense patches of tissue that are selectively surrounding some scaffold sections. Interestingly, this response does not uniformly surround all scaffold remnants equally but seems to be associated with pieces that are deeper in the wound bed. Furthermore, this response does not seem to have hampered the formation of new collagen networks (green staining) in the scaffold interior or hampered re-epithelialization so it is difficult to say what impact this unusual tissue response is having on overall wound healing.

Initial efforts to characterize the cellular immune response to these implants through IHC demonstrated that the scaffold remnants are directly covered with $CD206^{+}$ cells (Figure A23B), indicating that the cells primarily interacting with the implanted materials are M2-polarized macrophages which have a more reparative phenotype[278]. However, the cell-dense areas corresponding with the unusual tissue response are positively stained for iNOS (Figure A23B), a marker of M1-polarized macrophages which are considered more pro-inflammatory[279]. These very preliminary data potentially indicate that the PTK-UR implants are encouraging immune activation and inflammation, though this effect does not seem to be hindering overall healing of the wound site. Since this possibly inflammatory tissue response only appears at day 28 but was not seen at day 10, it could indicate that PTK-UR scaffolds themselves do not elicit an immune response but that the degradation products (only present in substantial concentrations at later time-points after material degradation) could be pro-inflammatory. Though more analysis is needed before drawing final conclusions, these data signify the importance of testing not only biodegradable materials

themselves for cytotoxicity and immune activation, but also their degradation products. They also demonstrate the importance of using advanced animal models for preclinical material evaluation. Therefore, future preclinical studies with PTK-based materials will also evaluate inflammatory capacity of material degradation products both *in vitro* and *in vivo* using rodent and porcine models.

A final concern to evaluate is the choice of isocyanate used in the fabrication of PTK-UR and PEUR scaffolds. It has been previously shown that LTI and HDIt evoke drastically different degradation profiles *in vitro*[76] (Figure 12), but these materials also elicit different responses upon *in vivo* implantation. As shown in Figure A16, PHD2 siNP-loaded PTK-UR scaffolds made with HDIt and implanted into diabetic excisional rat wounds were able to significantly decrease PHD2 expression as evaluated by qRT-PCR, similar to results seen with LTI-based PTK-UR scaffolds. However, histological evaluation of PTK-UR (HDIt) implants reveals that these scaffolds are much less integrated with the native tissue than LTI-based implants in excisional wounds (Figure A16). A similar difference in tissue infiltration between LTI and HDIt scaffolds was also seen in mice in previous work[28]. Interestingly, PTK-UR (HDIt) scaffolds implanted subcutaneously in rats (Figure 13) behaved very similarly to PTK-UR (LTI) scaffolds in the same wound model (Figure A10) over a 7-day time period by demonstrating very minimal infiltration. Therefore, it appears that LTI-based scaffolds elicit a more favorable tissue response in the more severe excisional wound model than HDIt scaffolds, whereas both scaffolds perform equally as well in the less-compromised subcutaneous model. This effect also seems to be apparent in the preliminary porcine wound healing data, with LTI-based PTK-UR scaffolds hosting more tissue infiltration and integration than analogous HDIt implants as demonstrated in Figure A23A. Though HDIt-based scaffolds might feature prolonged degradation times compared to LTI materials, its clinical usage could be limited by its reduced cellular adhesion properties and diminished cytocompatibility.

6.3 Broader impacts

Ongoing work discussed in section 6.4 outlines the application of PTK-UR scaffolds in a large animal model for wound healing studies. Successful outcomes from these tests may provide opportunities for

applying these materials in clinical trials either as a stand-alone scaffold material or as a drug delivery platform. The chronic wound healing market is estimated at $25B, and coupled with the rising number of diabetic patients and increased healthcare costs, there exists a great clinical need for therapies that improve wound healing. To date there is only a single siRNA/biomaterial platform in clinical trials for a wound healing application[192], indicating that there is both tremendous room for product growth in bioactive wound healing but also lingering hesitation by the pharmaceutical industry to invest in siRNA technologies. Conversely, the employment of stand-alone, biodegradable scaffold materials that improve wound healing without the use of a therapeutic agent would likely have a lower regulatory burden and could potentially find an easier path to market. PTK-UR formulations are protected by a recently approved US patent[280], and procurement of this technology through commercial licensing or acquisition could represent a viable strategy for clinical implementation of this biomaterial system.

As PTK-based hydrogels are in earlier stages of development, their horizon for clinical use is on a much longer trajectory. Also, these materials were designed as cell delivery vehicles; the use of allogenic or even autologous cells in patients is notoriously difficult to clear through regulators[192], thus making PTK hydrogels less commercially exciting for cell implantation applications. However, the facile chemistry of the water-soluble PEG-MAL-PTK macromers makes these materials easily transferred to any number of PEG hydrogel technologies. This translational potential of water-soluble PTK polymers is also aided by the high cost of enzymatically-degradable peptides. As companies look for hydrophilic materials that are specifically degraded by cellular activity, cheap and easily scalable PTK polymers could represent a promising candidate for commercialization.

6.4 Future work

The long-term goal of this work is to deploy therapeutic-laded tissue engineering materials into non-healing skin wounds to improve their healing outcomes. Initial efforts to delivery siRNA against PHD2 from PTK-UR scaffolds in diabetic rats were successful in improving blood vessel formation and overall wound healing as outlined in Chapter 4. However, siRNA-mediated silencing of PHD2 only lasted for 4

days post scaffold implantation due to the fast rate of tissue growth and the high dose of excipient that ensured a relatively quick rate of the siRNA. Future work will look to modify the siRNA release rate from the scaffolds using different excipients while also utilizing a more severe rodent wound healing model [281] that will decrease the rate of healing to make it more representative of chronic wound. Preliminary work has gone into developing this impaired rat skin wound healing model using a bipedicle ischemic flap as seen in Figure 43. Furthermore, recent work has highlighted additional molecular targets that modulate HIF-1α, providing new therapeutic strategies which can be incorporated into these local drug delivery systems. Work from the Matsui lab has demonstrated that intracellular oxidation can modify HIF-1α with glutathione units to stabilize the protein by preventing the binding of HIF-1α with the degradative von Hippel-Lindau protein[282]. These glutathione adducts are removed by glutaredoxin-1 (Glrx), thus making Glrx a potent regulator of HIF-1α activity separate from the classical PHD2 regulatory pathway and a potential siRNA target. Future work will explore the use of PHD2 and Glrx siRNA delivered separately and in tandem from implanted scaffolds to assess their relative potency for HIF-1α stabilization and any possible synergism between the two drug targets for improving wound healing outcomes.

For longer-term goals with PTK-UR scaffolds for local siRNA delivery, many efforts are underway to modify the siRNA delivery system to limit or eliminate the polymeric component needed to achieve intracellular siRNA distribution. Cationic polymer systems have well known toxicity issues due to their positive charge, and limiting the amount of polymer necessary for siRNA delivery will not only improve the effectiveness of these systems but also improve the clinical translatability of these technologies. Our lab is exploring the usage of hydrophobic tethers covalently attached to siRNA molecules to reduce the amount of nanoparticle-forming polymer necessary for effective payload delivery, and continuing work is underway to try and completely eliminate the need for cationic polymers as siRNA delivery vehicles. Efforts are also underway to develop an impaired skin wound model in pigs using bipedicle skin flaps Figure 44. Like the similar model developed in our lab for rats (Figure 43), this porcine model has shown impaired blood flow and a slowed healing rate compared to non-ischemic skin (Figure 45). Since skin wounds in pigs are the gold-standard for pre-clinical wound healing studies, the long-term goal of this work

is to implant our lead-candidate siRNA-containing PTK-UR scaffold formulation in these wounds following the guidance of the additional rat studies. It is anticipated that positive wound healing results in a large-scale, impaired wound healing model in pigs using our technology will effectively position this work for an easy transition into initial clinical trials.

Finally, additional work with PTK hydrogels will first complete additional *in vitro* studies to explore the ability for gel-encapsulated cells to maintain their viability without the presence of adhesive RGD peptides in the hydrogel networks. Since the PTK hydrogels are more hydrophobic than the other formulations, it is anticipated these new gel formulations could naturally adsorb adhesive proteins, thus completely eliminating the need for external incorporation of adhesive moieties. Next, the effect of gel weight % on *in vivo* material degradation in mice will be evaluated before delivering hydrogel-encapsulated MSCs *in vivo.* These studies will utilize the best-performing hydrogel formulations with a luciferase-expressing MSC cell line to non-invasively measure cell viability after *in vivo* implantation into wounds to assess cell survival over time. If these efforts prove successful, the long-term goals of this project involve tether siRNA into the hydrogel to transfect encapsulated MSCs and promote their proliferation to further enhance the wound healing potential of these cell/hydrogel materials.

6.5 Conclusion

The development of materials that are biocompatible, specifically degrade in the presence of cell-generated ROS, and can be affordably-synthesized in large scales presents a paradigm-shifting new technology in the biomaterials field. These multi-purpose materials represent an exciting new advance in environmentally-responsive materials and have the potential to enhance the healing outcomes of patients with chronic wounds.

Bibliography

1. Sen, C.K., et al., *Human skin wounds: A major and snowballing threat to public health and the economy.* Wound Repair and Regeneration, 2009. **17**(6): p. 763-771.
2. Geiss, L.S., et al., *Prevalence and Incidence Trends for Diagnosed Diabetes Among Adults Aged 20 to 79 Years, United States, 1980-2012* The Journal of the American Medical Association, 2014. **312**(12): p. 1218-1226.
3. CDC, *National Diabetes Statistics Report: Estimates of Diabetes and Its Burden in the United States*, U.D.o.H.a.H. Services, Editor. 2014: Atlanta, GA.
4. Catrina, S.-B. and X. Zheng, *Disturbed hypoxic responses as a pathogenic mechanism of diabetic foot ulcers.* Diabetes/Metabolism Research and Reviews, 2016. **32**: p. 179-185.
5. Moseley, R., et al., *Comparison of oxidative stress biomarker profiles between acute and chronic wound environments.* Wound Repair and Regeneration, 2004. **12**(4): p. 419-429.
6. Wlaschek, M. and K. Scharffetter-Kochanek, *Oxidative stress in chronic venous leg ulcers.* Wound Repair and Regeneration, 2005. **13**(5): p. 452-461.
7. Steed, D.L. and t.D.U. Study Group, *Clinical evaluation of recombinant human platelet – derived growth factor for the treatment of lower extremity diabetic ulcers.* Journal of Vascular Surgery, 1995. **21**(1): p. 71-81.
8. Rosemann, A., *Why Regenerative Stem Cell Medicine Progresses Slower Than Expected.* Journal of Cellular Biochemistry, 2014. **115**(12): p. 2073-2076.
9. Catrina, S.-B., et al., *Hyperglycemia Regulates Hypoxia-Inducible Factor-1α Protein Stability and Function.* Diabetes, 2004. **53**(12): p. 3226-3232.
10. Thangarajah, H., et al., *HIF-1α dysfunction in diabetes.* Cell Cycle, 2010. **9**(1): p. 75-79.
11. Forsythe, J.A., et al., *Activation of vascular endothelial growth factor gene transcription by hypoxia-inducible factor 1.* Molecular and cellular biology, 1996. **16**(9): p. 4604-4613.
12. Kelly, B.D., et al., *Cell type–specific regulation of angiogenic growth factor gene expression and induction of angiogenesis in nonischemic tissue by a constitutively active form of hypoxia-inducible factor 1.* Circulation Research, 2003. **93**(11): p. 1074-1081.
13. Ceradini, D.J., et al., *Progenitor cell trafficking is regulated by hypoxic gradients through HIF-1 induction of SDF-1.* Nature medicine, 2004. **10**(8): p. 858-864.
14. Epstein, A.C.R., et al., *C. elegans EGL-9 and Mammalian Homologs Define a Family of Dioxygenases that Regulate HIF by Prolyl Hydroxylation.* Cell, 2001. **107**(1): p. 43-54.
15. Berra, E., et al., *HIF prolyl-hydroxylase 2 is the key oxygen sensor setting low steady-state levels of HIF-1α in normoxia.* The EMBO journal, 2003. **22**(16): p. 4082-4090.
16. Wu, S., et al., *Enhancement of Angiogenesis Through Stabilization of Hypoxia-inducible Factor-1 by Silencing Prolyl Hydroxylase Domain-2 Gene.* Mol Ther, 2008. **16**(7): p. 1227-1234.
17. Kalucka, J., et al., *Loss of Epithelial Hypoxia-Inducible Factor Prolyl Hydroxylase 2 Accelerates Skin Wound Healing in Mice.* Molecular and Cellular Biology, 2013. **33**(17): p. 3426-3438.
18. Zhang, X., et al., *Wound Healing Improvement with PHD-2 Silenced Fibroblasts in Diabetic Mice.* PLoS ONE, 2013. **8**(12): p. e84548.
19. Zimmermann, A.S., et al., *Epidermal or Dermal Specific Knockout of PHD-2 Enhances Wound Healing and Minimizes Ischemic Injury.* PLoS ONE, 2014. **9**(4): p. e93373.
20. Botusan, I.R., et al., *Stabilization of HIF-1α is critical to improve wound healing in diabetic mice.* Proceedings of the National Academy of Sciences, 2008. **105**(49): p. 19426-19431.
21. Zhang, Y., et al., *Drug-induced regeneration in adult mice.* Science Translational Medicine, 2015. **7**(290): p. 290ra92.
22. Chang, E.I., et al., *Age Decreases Endothelial Progenitor Cell Recruitment Through Decreases in Hypoxia-Inducible Factor 1α Stabilization During Ischemia.* Circulation, 2007. **116**(24): p. 2818-2829.
23. Chen, H., et al., *Upregulating Hif-1α by Hydrogel Nanofibrous Scaffolds for Rapidly Recruiting Angiogenesis Relative Cells in Diabetic Wound.* Advanced Healthcare Materials, 2016. **5**(8): p. 907-918.
24. Fraisl, P., J. Aragones, and P. Carmeliet, *Inhibition of oxygen sensors as a therapeutic strategy for ischaemic and inflammatory disease.* Nat Rev Drug Discov, 2009. **8**(2): p. 139-152.
25. Schneider, M., et al., *Therapeutic inhibition of prolyl hydroxylase domain-containing enzymes in surgery: putative applications and challenges.* Hypoxia, 2015. **3**: p. 1-14.

26. Chan, M.C., et al., *Pharmacological targeting of the HIF hydroxylases – A new field in medicine development.* Molecular Aspects of Medicine, 2016. **47–48**: p. 54-75.
27. Wetterau, M., et al., *Topical prolyl hydroxylase domain-2 silencing improves diabetic murine wound closure.* Wound Repair and Regeneration, 2011. **19**(4): p. 481-486.
28. Nelson, C.E., et al., *Tunable Delivery of siRNA from a Biodegradable Scaffold to Promote Angiogenesis In Vivo.* Advanced Materials, 2014. **26**(4): p. 607-614.
29. Vandegrift, M.T., et al., *Acellular dermal matrix-based gene therapy augments graft incorporation.* Journal of Surgical Research, 2015. **195**(1): p. 360-367.
30. Martin, J.R., et al., *A porous tissue engineering scaffold selectively degraded by cell-generated reactive oxygen species.* Biomaterials, 2014. **35**(12): p. 3766-3776.
31. Nelson, C.E., *Tunable Delivery of siRNA from a Biodegradable Scaffold for Regenerative Medicine*. 2014, Vanderbilt University.
32. Ren, G., et al., *Mesenchymal Stem Cell-Mediated Immunosuppression Occurs via Concerted Action of Chemokines and Nitric Oxide.* Cell Stem Cell, 2008. **2**(2): p. 141-150.
33. Chen, L., et al., *Paracrine factors of mesenchymal stem cells recruit macrophages and endothelial lineage cells and enhance wound healing.* PloS one, 2008. **3**(4): p. e1886.
34. Nair, L.S. and C.T. Laurencin, *Biodegradable polymers as biomaterials.* Progress in Polymer Science, 2007. **32**(8–9): p. 762-798.
35. Amini, A.R., J.S. Wallace, and S.P. Nukavarapu, *Short-term and long-term effects of orthopedic biodegradable implants.* Journal of long-term effects of medical implants, 2011. **21**(2): p. 93-122.
36. Dumas, J.E., et al., *Balancing the Rates of New Bone formation and Polymer Degradation Enhances Healing of Weight-Bearing Allograft/Polyurethane Composites in Rabbit Femoral Defects.* Tissue Engineering Part A, 2013. **20**(1-2): p. 115-129.
37. Thayer, A.M., *Improving Peptides*, in *Chemical & Engineering News*. 2011, American Chemical Society. p. 13-20.
38. Thundiamadathil, J., *Challenges in the large scale production of peptides*, in *Specialty Chemicals Magazine*. 2013. p. 26-28.
39. Hensley, K., et al., *Reactive oxygen species, cell signaling, and cell injury.* Free Radical Biology and Medicine, 2000. **28**(10): p. 1456-1462.
40. Pacher, P., J.S. Beckman, and L. Liaudet, *Nitric Oxide and Peroxynitrite in Health and Disease.* Physiological Reviews, 2007. **87**(1): p. 315-424.
41. Lee, S.H., et al., *Current Progress in Reactive Oxygen Species (ROS)-Responsive Materials for Biomedical Applications.* Advanced Healthcare Materials, 2013. **2**(6): p. 908-915.
42. Song, C.-C., F.-S. Du, and Z.-C. Li, *Oxidation-responsive polymers for biomedical applications.* Journal of Materials Chemistry B, 2014. **2**(22): p. 3413-3426.
43. Martin, J.R. and C.L. Duvall, *Oxidation State as a Bioresponsive Trigger*, in *Oxidative Stress and Biomaterials*, T. Dziubla and D.A. Butterfield, Editors. 2016, Academic Press: Cambridge, MA. p. 225-250.
44. Liu, W.F., et al., *Real-time in vivo detection of biomaterial-induced reactive oxygen species.* Biomaterials, 2011. **32**(7): p. 1796-1801.
45. Wilson, D.S., et al., *Orally delivered thioketal nanoparticles loaded with TNF-α–siRNA target inflammation and inhibit gene expression in the intestines.* Nat Mater, 2010. **9**(11): p. 923-928.
46. Martin, J.R., et al., *Local Delivery of PHD2 siRNA from ROS-Degradable Scaffolds to Promote Diabetic Wound Healing.* Advanced Healthcare Materials, 2016. **5**(21): p. 2751-2757.
47. Lin, C.-C. and K.S. Anseth, *PEG Hydrogels for the Controlled Release of Biomolecules in Regenerative Medicine.* Pharmaceutical Research, 2009. **26**(3): p. 631-643.
48. Zhong, S., Y. Zhang, and C. Lim, *Tissue scaffolds for skin wound healing and dermal reconstruction.* Wiley Interdisciplinary Reviews: Nanomedicine and Nanobiotechnology, 2010. **2**(5): p. 510-525.
49. Sarett, S.M., C.E. Nelson, and C.L. Duvall, *Technologies for controlled, local delivery of siRNA.* Journal of Controlled Release, 2015. **218**: p. 94-113.
50. Mooney, D.J. and H. Vandenburgh, *Cell Delivery Mechanisms for Tissue Repair.* Cell Stem Cell, 2008. **2**(3): p. 205-213.
51. Whang, K., et al., *A novel method to fabricate bioabsorbable scaffolds.* Polymer, 1995. **36**(4): p. 837-842.
52. Ishaug-Riley, S.L., et al., *Three-dimensional culture of rat calvarial osteoblasts in porous biodegradable polymers.* Biomaterials, 1998. **19**(15): p. 1405-1412.

53. Lowry, K.J., et al., *Polycaprolactone/glass bioabsorbable implant in a rabbit humerus fracture model.* Journal of Biomedical Materials Research, 1997. **36**(4): p. 536-541.
54. Ciapetti, G., et al., *Osteoblast growth and function in porous poly ε-caprolactone matrices for bone repair: a preliminary study.* Biomaterials, 2003. **24**(21): p. 3815-3824.
55. Leong, K.W., V. Simonte, and R.S. Langer, *Synthesis of polyanhydrides: melt-polycondensation, dehydrochlorination, and dehydrative coupling.* Macromolecules, 1987. **20**(4): p. 705-712.
56. Ibim, S.E.M., et al., *Preliminary in vivo report on the osteocompatibility of poly(anhydride-co-imides) evaluated in a tibial model.* Journal of Biomedical Materials Research, 1998. **43**(4): p. 374-379.
57. Nilsson, A., et al., *Results from a degradable TMC joint Spacer (Artelon) compared with tendon arthroplasty.* The Journal of Hand Surgery, 2005. **30**(2): p. 380-389.
58. Gogolewski, S., K. Gorna, and A.S. Turner, *Regeneration of bicortical defects in the iliac crest of estrogen-deficient sheep, using new biodegradable polyurethane bone graft substitutes.* Journal of Biomedical Materials Research Part A, 2006. **77A**(4): p. 802-810.
59. Lü, J.-M., et al., *Current advances in research and clinical applications of PLGA-based nanotechnology.* Expert Review of Molecular Diagnostics, 2009. **9**(4): p. 325-341.
60. Bezwada, R.S., et al., *Monocryl® suture, a new ultra-pliable absorbable monofilament suture.* Biomaterials, 1995. **16**(15): p. 1141-1148.
61. Dang, W., T. Daviau, and H. Brem, *Morphological Characterization of Polyanhydride Biodegradable Implant Gliadel® During in Vitro and in Vivo Erosion Using Scanning Electron Microscopy.* Pharmaceutical Research, 1996. **13**(5): p. 683-691.
62. Chen, J., et al., *Scaffolds for tendon and ligament repair: review of the efficacy of commercial products.* Expert Review of Medical Devices, 2009. **6**(1): p. 61-73.
63. Hafeman, A.E., et al., *Injectable Biodegradable Polyurethane Scaffolds with Release of Platelet-derived Growth Factor for Tissue Repair and Regeneration.* Pharmaceutical Research, 2008. **25**(10): p. 2387-2399.
64. Ignatius, A.A. and L.E. Claes, *In vitro biocompatibility of bioresorbable polymers: poly(L, DL-lactide) and poly(L-lactide-co-glycolide).* Biomaterials, 1996. **17**(8): p. 831-839.
65. Hua, N. and J. Sun, *Body distribution of poly(d,l-lactide-co-glycolide) copolymer degradation products in rats.* Journal of Materials Science: Materials in Medicine, 2008. **19**(10): p. 3243-3248.
66. Visscher, G.E., et al., *Biodegradation of and tissue reaction to 50:50 poly(DL-lactide-co-glycolide) microcapsules.* Journal of Biomedical Materials Research, 1985. **19**(3): p. 349-365.
67. Zustiak, S.P. and J.B. Leach, *Hydrolytically Degradable Poly(Ethylene Glycol) Hydrogel Scaffolds with Tunable Degradation and Mechanical Properties.* Biomacromolecules, 2010. **11**(5): p. 1348-1357.
68. Middleton, J.C. and A.J. Tipton, *Synthetic biodegradable polymers as orthopedic devices.* Biomaterials, 2000. **21**(23): p. 2335-2346.
69. Maurus, P.B. and C.C. Kaeding, *Bioabsorbable implant material review.* Operative Techniques in Sports Medicine, 2004. **12**(3): p. 158-160.
70. Fu, K., et al., *Visual Evidence of Acidic Environment Within Degrading Poly(lactic-co-glycolic acid) (PLGA) Microspheres.* Pharmaceutical Research, 2000. **17**(1): p. 100-106.
71. Lu, L., et al., *In vitro and in vivo degradation of porous poly(dl-lactic-co-glycolic acid) foams.* Biomaterials, 2000. **21**(18): p. 1837-1845.
72. Antheunis, H., et al., *Autocatalytic Equation Describing the Change in Molecular Weight during Hydrolytic Degradation of Aliphatic Polyesters.* Biomacromolecules, 2010. **11**(4): p. 1118-1124.
73. An, Y.H., S.K. Woolf, and R.J. Friedman, *Pre-clinical in vivo evaluation of orthopaedic bioabsorbable devices.* Biomaterials, 2000. **21**(24): p. 2635-2652.
74. Guelcher, S.A., *Biodegradable Polyurethanes: Synthesis and Applications in Regenerative Medicine.* Tissue Engineering: Part B, 2008. **14**(1): p. 3-17.
75. Guelcher, S.A., et al., *Synthesis, In Vitro Degradation, and Mechanical Properties of Two-Component Poly(Ester Urethane)Urea Scaffolds: Effects of Water and Polyol Composition* Tissue Engineering, 2007. **13**(9): p. 2321-2333.
76. Hafeman, A.E., et al., *Characterization of the degradation mechanisms of lysine-derived aliphatic poly(ester urethane) scaffolds.* Biomaterials, 2011. **32**(2): p. 419-429.
77. Dumas, J.E., et al., *Injectable reactive biocomposites for bone healing in critical-size rabbit calvarial defects.* Biomedical Materials, 2012. **7**(2): p. 024112.
78. Li, B., J.M. Davidson, and S.A. Guelcher, *The effect of the local delivery of platelet-derived growth factor from reactive two-component polyurethane scaffolds on the healing in rat skin excisional wounds.* Biomaterials, 2009. **30**(20): p. 3486-3494.

79. Adolph, E.J., et al., *Injectable polyurethane composite scaffolds delay wound contraction and support cellular infiltration and remodeling in rat excisional wounds.* Journal of Biomedical Materials Research Part A, 2012. **100A**(2): p. 450-461.
80. Adolph, E.J., et al., *Injected biodegradable polyurethane scaffolds support tissue infiltration and delay wound contraction in a porcine excisional model.* Journal of Biomedical Materials Research Part B: Applied Biomaterials, 2015: p. n/a-n/a.
81. Li, B., et al., *The effects of rhBMP-2 released from biodegradable polyurethane/microsphere composite scaffolds on new bone formation in rat femora.* Biomaterials, 2009. **30**(35): p. 6768-6779.
82. Dumas, J.E., et al., *Synthesis and characterization of an injectable allograft bone/polymer composite bone void filler with tunable mechanical properties.* Tissue Engineering, Part A: Tissue Engineering, 2010. **16**(8): p. 2505-2518.
83. Page, J.M., et al., *Biocompatibility and chemical reaction kinetics of injectable, settable polyurethane/allograft bone biocomposites.* Acta Biomaterialia, 2012. **8**(12): p. 4405-4416.
84. Hafeman, A.E., et al., *Local Delivery of Tobramycin from Injectable Biodegradable Polyurethane Scaffolds.* Journal of Biomaterials Science, Polymer Edition, 2010. **21**(1): p. 95-112.
85. Nelson, C.E., et al., *Sustained local delivery of siRNA from an injectable scaffold.* Biomaterials, 2012. **33**(4): p. 1154-1161.
86. Adolph, E.J., et al., *Enhanced performance of plasmid DNA polyplexes stabilized by a combination of core hydrophobicity and surface PEGylation.* Journal of Materials Chemistry B, 2014. **2**(46): p. 8154-8164.
87. Guo, R., et al., *A transient cell-shielding method for viable MSC delivery within hydrophobic scaffolds polymerized in situ.* Biomaterials, 2015. **54**(0): p. 21-33.
88. Li, Y., J. Rodrigues, and H. Tomas, *Injectable and biodegradable hydrogels: gelation, biodegradation and biomedical applications.* Chemical Society Reviews, 2012. **41**(6): p. 2193-2221.
89. Khetan, S. and J.A. Burdick, *Patterning network structure to spatially control cellular remodeling and stem cell fate within 3-dimensional hydrogels.* Biomaterials, 2010. **31**(32): p. 8228-8234.
90. Michel, R., et al., *Influence of PEG Architecture on Protein Adsorption and Conformation.* Langmuir, 2005. **21**(26): p. 12327-12332.
91. Zhu, J., *Bioactive modification of poly(ethylene glycol) hydrogels for tissue engineering.* Biomaterials, 2010. **31**(17): p. 4639-4656.
92. Burdick, J.A. and K.S. Anseth, *Photoencapsulation of osteoblasts in injectable RGD-modified PEG hydrogels for bone tissue engineering.* Biomaterials, 2002. **23**(22): p. 4315-4323.
93. Phelps, E.A., et al., *Maleimide Cross-Linked Bioactive PEG Hydrogel Exhibits Improved Reaction Kinetics and Cross-Linking for Cell Encapsulation and In Situ Delivery.* Advanced Materials, 2012. **24**(1): p. 64-70.
94. Phelps, E.A., et al., *Vasculogenic bio-synthetic hydrogel for enhancement of pancreatic islet engraftment and function in type 1 diabetes.* Biomaterials, 2013. **34**(19): p. 4602-4611.
95. Aimetti, A.A., A.J. Machen, and K.S. Anseth, *Poly(ethylene glycol) hydrogels formed by thiol-ene photopolymerization for enzyme-responsive protein delivery.* Biomaterials, 2009. **30**(30): p. 6048-6054.
96. Lin, G., et al., *Injectable and thermosensitive PLGA-g-PEG hydrogels containing hydroxyapatite: preparation, characterization and in vitro release behavior.* Biomedical Materials, 2012. **7**(2): p. 024107.
97. Elisseeff, J., et al., *Transdermal photopolymerization for minimally invasive implantation.* Proceedings of the National Academy of Sciences, 1999. **96**(6): p. 3104-3107.
98. Lee, S.H., et al., *In Situ Crosslinkable Gelatin Hydrogels for Vasculogenic Induction and Delivery of Mesenchymal Stem Cells.* Advanced Functional Materials, 2014: p. n/a-n/a.
99. Jin, R., et al., *Injectable chitosan-based hydrogels for cartilage tissue engineering.* Biomaterials, 2009. **30**(13): p. 2544-2551.
100. Kim, K.S., et al., *Injectable hyaluronic acid–tyramine hydrogels for the treatment of rheumatoid arthritis.* Acta Biomaterialia, 2011. **7**(2): p. 666-674.
101. van Dijk, M., et al., *Synthesis and Characterization of Enzymatically Biodegradable PEG and Peptide-Based Hydrogels Prepared by Click Chemistry.* Biomacromolecules, 2010. **11**(6): p. 1608-1614.
102. DeForest, C.A., B.D. Polizzotti, and K.S. Anseth, *Sequential click reactions for synthesizing and patterning three-dimensional cell microenvironments.* Nat Mater, 2009. **8**(8): p. 659-664.
103. Jin, R., et al., *Synthesis and characterization of hyaluronic acid–poly(ethylene glycol) hydrogels via Michael addition: An injectable biomaterial for cartilage repair.* Acta Biomaterialia, 2010. **6**(6): p. 1968-1977.

104. Rizzi, S.C. and J.A. Hubbell, *Recombinant Protein-co-PEG Networks as Cell-Adhesive and Proteolytically Degradable Hydrogel Matrixes. Part I: Development and Physicochemical Characteristics.* Biomacromolecules, 2005. **6**(3): p. 1226-1238.
105. Lutolf, M.P. and J.A. Hubbell, *Synthesis and Physicochemical Characterization of End-Linked Poly(ethylene glycol)-co-peptide Hydrogels Formed by Michael-Type Addition.* Biomacromolecules, 2003. **4**(3): p. 713-722.
106. Ifkovits, J.L. and J.A. Burdick, *Review: photopolymerizable and degradable biomaterials for tissue engineering applications.* Tissue engineering, 2007. **13**(10): p. 2369-2385.
107. DeLong, S.A., A.S. Gobin, and J.L. West, *Covalent immobilization of RGDS on hydrogel surfaces to direct cell alignment and migration.* Journal of Controlled Release, 2005. **109**(1–3): p. 139-148.
108. Bryant, S.J., C.R. Nuttelman, and K.S. Anseth, *Cytocompatibility of UV and visible light photoinitiating systems on cultured NIH/3T3 fibroblasts in vitro.* Journal of Biomaterials Science, Polymer Edition, 2000. **11**(5): p. 439-457.
109. Ovsianikov, A., et al., *Three-dimensional laser micro- and nano-structuring of acrylated poly(ethylene glycol) materials and evaluation of their cytoxicity for tissue engineering applications.* Acta Biomaterialia, 2011. **7**(3): p. 967-974.
110. Williams, C.G., et al., *Variable cytocompatibility of six cell lines with photoinitiators used for polymerizing hydrogels and cell encapsulation.* Biomaterials, 2005. **26**(11): p. 1211-1218.
111. Mather, B.D., et al., *Michael addition reactions in macromolecular design for emerging technologies.* Progress in Polymer Science, 2006. **31**(5): p. 487-531.
112. Miller, J.S., et al., *Bioactive hydrogels made from step-growth derived PEG–peptide macromers.* Biomaterials, 2010. **31**(13): p. 3736-3743.
113. Hermanson, G.T., *Bioconjugate Techniques*. Vol. 3. 2013, San Diego: Academic Press.
114. Roy, D., J.N. Cambre, and B.S. Sumerlin, *Future perspectives and recent advances in stimuli-responsive materials.* Progress in Polymer Science, 2010. **35**(1–2): p. 278-301.
115. West, J.L. and J.A. Hubbell, *Polymeric Biomaterials with Degradation Sites for Proteases Involved in Cell Migration.* Macromolecules, 1998. **32**(1): p. 241-244.
116. Lutolf, M.P., et al., *Repair of bone defects using synthetic mimetics of collagenous extracellular matrices.* Nat Biotech, 2003. **21**(5): p. 513-518.
117. Dey, J., et al., *Development of biodegradable crosslinked urethane-doped polyester elastomers.* Biomaterials, 2008. **29**(35): p. 4637-4649.
118. Stakleff, K.S., et al., *Resorbable, amino acid-based poly(ester urea)s crosslinked with osteogenic growth peptide with enhanced mechanical properties and bioactivity.* Acta Biomaterialia, 2013. **9**(2): p. 5132-5142.
119. Guan, J. and W.R. Wagner, *Synthesis, Characterization and Cytocompatibility of Polyurethaneurea Elastomers with Designed Elastase Sensitivity.* Biomacromolecules, 2005. **6**(5): p. 2833-2842.
120. Patterson, J. and J.A. Hubbell, *Enhanced proteolytic degradation of molecularly engineered PEG hydrogels in response to MMP-1 and MMP-2.* Biomaterials, 2010. **31**(30): p. 7836-7845.
121. Lin, J. and M.L. Lindsey, *MMP roles in the initiation and progression of cardiac remodeling leading to congestive heart failure*, in *Matrix Metalloproteinases in Tissue Remodelling and Inflammation*, V. Lagente and E. Boichot, Editors. 2008, Springer: Basel, CHE. p. 103.
122. Parrott, M.C., et al., *Tunable Bifunctional Silyl Ether Cross-Linkers for the Design of Acid-Sensitive Biomaterials.* Journal of the American Chemical Society, 2010. **132**(50): p. 17928-17932.
123. Napoli, A., et al., *Oxidation-responsive polymeric vesicles.* Nat Mater, 2004. **3**(3): p. 183-189.
124. Pu, H.-L., et al., *Nanoparticles with Dual Responses to Oxidative Stress and Reduced pH for Drug Release and Anti-inflammatory Applications.* ACS Nano, 2014. **8**(2): p. 1213-1221.
125. Qiu, Y. and K. Park, *Environment-sensitive hydrogels for drug delivery.* Advanced Drug Delivery Reviews, 2012. **64, Supplement**(0): p. 49-60.
126. Cheng, R., et al., *Dual and multi-stimuli responsive polymeric nanoparticles for programmed site-specific drug delivery.* Biomaterials, 2013. **34**(14): p. 3647-3657.
127. Vasir, J.K. and V. Labhasetwar, *Biodegradable nanoparticles for cytosolic delivery of therapeutics.* Advanced Drug Delivery Reviews, 2007. **59**(8): p. 718-728.
128. Savic, R., A. Eisenberg, and D. Maysinger, *Block copolymer micelles as delivery vehicles of hydrophobic drugs: micelle-cell interactions.* Journal of drug targeting, 2006. **14**(6): p. 343-355.
129. Zhu, M., et al., *Physicochemical Properties Determine Nanomaterial Cellular Uptake, Transport, and Fate.* Accounts of Chemical Research, 2013. **46**(3): p. 622-631.

130. Convertine, A.J., et al., *Development of a novel endosomolytic diblock copolymer for siRNA delivery.* Journal of Controlled Release, 2009. **133**(3): p. 221-229.
131. Nelson, C.E., et al., *Balancing Cationic and Hydrophobic Content of PEGylated siRNA Polyplexes Enhances Endosome Escape, Stability, Blood Circulation Time, and Bioactivity in Vivo.* ACS Nano, 2013. **7**(10): p. 8870-8880.
132. Dupré-Crochet, S., M. Erard, and O. Nüβe, *ROS production in phagocytes: why, when, and where?* Journal of leukocyte biology, 2013. **94**(4): p. 657-670.
133. Rosen, G.M., et al., *Free radicals and phagocytic cells.* The FASEB Journal, 1995. **9**(2): p. 200-209.
134. Ross, R., *Atherosclerosis — An Inflammatory Disease.* New England Journal of Medicine, 1999. **340**(2): p. 115-126.
135. Trachootham, D., J. Alexandre, and P. Huang, *Targeting cancer cells by ROS-mediated mechanisms: a radical therapeutic approach?* Nat Rev Drug Discov, 2009. **8**(7): p. 579-591.
136. Kumar, B., et al., *Oxidative Stress Is Inherent in Prostate Cancer Cells and Is Required for Aggressive Phenotype.* Cancer Research, 2008. **68**(6): p. 1777-1785.
137. Dopheide, J.F., et al., *Critical limb ischaemia is characterised by an increased production of whole blood reactive oxygen species and expression of TREM-1 on neutrophils.* Atherosclerosis, 2013. **229**(2): p. 396-403.
138. Di, A., et al., *The redox-sensitive cation channel TRPM2 modulates phagocyte ROS production and inflammation.* Nat Immunol, 2012. **13**(1): p. 29-34.
139. Vo, C.D., G. Kilcher, and N. Tirelli, *Polymers and Sulfur: what are Organic Polysulfides Good For? Preparative Strategies and Biological Applications.* Macromolecular Rapid Communications, 2009. **30**(4-5): p. 299-315.
140. Carampin, P., et al., *Oxidant-Dependent REDOX Responsiveness of Polysulfides.* Macromolecular Chemistry and Physics, 2012. **213**(19): p. 2052-2061.
141. Jeanmaire, D., et al., *Chemical specificity in REDOX-responsive materials: the diverse effects of different Reactive Oxygen Species (ROS) on polysulfide nanoparticles.* Polymer Chemistry, 2014. **5**(4): p. 1393-1404.
142. Gupta, M.K., et al., *Poly(PS-b-DMA) micelles for reactive oxygen species triggered drug release.* Journal of Controlled Release, 2012. **162**(3): p. 591-598.
143. Gupta, M.K., et al., *Cell Protective, ABC Triblock Polymer-Based Thermoresponsive Hydrogels with ROS-Triggered Degradation and Drug Release.* Journal of the American Chemical Society, 2014. **136**(42): p. 14896-14902.
144. Poole, K.M., et al., *ROS-responsive microspheres for on demand antioxidant therapy in a model of diabetic peripheral arterial disease.* Biomaterials, 2015. **41**(0): p. 166-175.
145. Hu, P. and N. Tirelli, *Scavenging ROS: Superoxide Dismutase/Catalase Mimetics by the Use of an Oxidation-Sensitive Nanocarrier/Enzyme Conjugate.* Bioconjugate Chemistry, 2012. **23**(3): p. 438-449.
146. Cerritelli, S., et al., *Aggregation Behavior of Poly(ethylene glycol-bl-propylene sulfide) Di- and Triblock Copolymers in Aqueous Solution.* Langmuir, 2009. **25**(19): p. 11328-11335.
147. Velluto, D., D. Demurtas, and J.A. Hubbell, *PEG-b-PPS Diblock Copolymer Aggregates for Hydrophobic Drug Solubilization and Release: Cyclosporin A as an Example.* Molecular Pharmaceutics, 2008. **5**(4): p. 632-642.
148. Dane, K.Y., et al., *Nano-sized drug-loaded micelles deliver payload to lymph node immune cells and prolong allograft survival.* Journal of Controlled Release, 2011. **156**(2): p. 154-160.
149. Rehor, A., J.A. Hubbell, and N. Tirelli, *Oxidation-Sensitive Polymeric Nanoparticles.* Langmuir, 2005. **21**(1): p. 411-417.
150. Reddy, S.T., et al., *In vivo targeting of dendritic cells in lymph nodes with poly(propylene sulfide) nanoparticles.* Journal of Controlled Release, 2006. **112**(1): p. 26-34.
151. Reddy, S.T., et al., *Exploiting lymphatic transport and complement activation in nanoparticle vaccines.* Nat Biotech, 2007. **25**(10): p. 1159-1164.
152. Scott, E.A., et al., *Dendritic cell activation and T cell priming with adjuvant- and antigen-loaded oxidation-sensitive polymersomes.* Biomaterials, 2012. **33**(26): p. 6211-6219.
153. Xu, H., W. Cao, and X. Zhang, *Selenium-Containing Polymers: Promising Biomaterials for Controlled Release and Enzyme Mimics.* Accounts of Chemical Research, 2013. **46**(7): p. 1647-1658.
154. Ma, N., et al., *Selenium-containing block copolymers and their oxidation-responsive aggregates.* Polymer Chemistry, 2010. **1**(10): p. 1609-1614.

155. Han, P., et al., *Oxidation-Responsive Micelles Based on a Selenium-Containing Polymeric Superamphiphile.* Langmuir, 2010. **26**(18): p. 14414-14418.
156. Ren, H., et al., *Side-chain selenium-containing amphiphilic block copolymers: redox-controlled self-assembly and disassembly.* Soft Matter, 2012. **8**(5): p. 1460-1466.
157. Liu, J., et al., *Therapeutic Nanocarriers with Hydrogen Peroxide-Triggered Drug Release for Cancer Treatment.* Biomacromolecules, 2013. **14**(5): p. 1627-1636.
158. Ghosh, J., *Rapid induction of apoptosis in prostate cancer cells by selenium: reversal by metabolites of arachidonate 5-lipoxygenase.* Biochemical and Biophysical Research Communications, 2004. **315**(3): p. 624-635.
159. Chandross, E.A., *A new chemiluminescent system.* Tetrahedron Letters, 1963. **4**(12): p. 761-765.
160. Bos, R., et al., *Studies on the mechanism of the peroxyoxalate chemiluminescence reaction: Part 1. Confirmation of 1,2-dioxetanedione as an intermediate using 13C nuclear magnetic resonance spectroscopy.* Analytica Chimica Acta, 2004. **502**(2): p. 141-147.
161. Lee, D., et al., *In vivo imaging of hydrogen peroxide with chemiluminescent nanoparticles.* Nat Mater, 2007. **6**(10): p. 765-769.
162. Cho, S., et al., *Chemiluminescent and Antioxidant Micelles as Theranostic Agents for Hydrogen Peroxide Associated-Inflammatory Diseases.* Advanced Functional Materials, 2012. **22**(19): p. 4038-4043.
163. Lee, D., et al., *Hydrogen peroxide-responsive copolyoxalate nanoparticles for detection and therapy of ischemia–reperfusion injury.* Journal of Controlled Release, 2013. **172**(3): p. 1102-1110.
164. Lee, D., et al., *H2O2-responsive molecularly engineered polymer nanoparticles as ischemia/reperfusion-targeted nanotherapeutic agents.* Sci. Rep., 2013. **3**.
165. Kwon, J., et al., *Inflammation-Responsive Antioxidant Nanoparticles Based on a Polymeric Prodrug of Vanillin.* Biomacromolecules, 2013. **14**(5): p. 1618-1626.
166. Ainley, A.D. and F. Challenger, *CCLXXX.—Studies of the boron–carbon linkage. Part I. The oxidation and nitration of phenylboric acid.* Journal of the Chemical Society (Resumed), 1930: p. 2171-2180.
167. Chang, M.C.Y., et al., *A Selective, Cell-Permeable Optical Probe for Hydrogen Peroxide in Living Cells.* Journal of the American Chemical Society, 2004. **126**(47): p. 15392-15393.
168. Weinstain, R., et al., *In Vivo Targeting of Hydrogen Peroxide by Activatable Cell-Penetrating Peptides.* Journal of the American Chemical Society, 2014. **136**(3): p. 874-877.
169. Major Jourden, J.L. and S.M. Cohen, *Hydrogen Peroxide Activated Matrix Metalloproteinase Inhibitors: A Prodrug Approach.* Angewandte Chemie, 2010. **122**(38): p. 6947-6949.
170. Wang, M., et al., *Reactive Oxygen Species-Responsive Protein Modification and Its Intracellular Delivery for Targeted Cancer Therapy.* Angewandte Chemie International Edition, 2014. **53**(49): p. 13444-13448.
171. Broaders, K.E., S. Grandhe, and J.M.J. Fréchet, *A Biocompatible Oxidation-Triggered Carrier Polymer with Potential in Therapeutics.* Journal of the American Chemical Society, 2010. **133**(4): p. 756-758.
172. de Gracia Lux, C., et al., *Biocompatible Polymeric Nanoparticles Degrade and Release Cargo in Response to Biologically Relevant Levels of Hydrogen Peroxide.* Journal of the American Chemical Society, 2012. **134**(38): p. 15758-15764.
173. Viger, M.L., et al., *Collective Activation of MRI Agents via Encapsulation and Disease-Triggered Release.* Journal of the American Chemical Society, 2013. **135**(21): p. 7847-7850.
174. Zhang, D., et al., *Biocompatible Reactive Oxygen Species (ROS)-Responsive Nanoparticles as Superior Drug Delivery Vehicles.* Advanced Healthcare Materials, 2015. **4**(1): p. 69-76.
175. Song, C.-C., et al., *Oxidation-Accelerated Hydrolysis of the Ortho Ester-Containing Acid-Labile Polymers.* ACS Macro Letters, 2013. **2**(3): p. 273-277.
176. Song, C.-C., et al., *Oxidation-Responsive Poly(amino ester)s Containing Arylboronic Ester and Self-Immolative Motif: Synthesis and Degradation Study.* Macromolecules, 2013. **46**(21): p. 8416-8425.
177. Shim, M.S. and Y. Xia, *A Reactive Oxygen Species (ROS)-Responsive Polymer for Safe, Efficient, and Targeted Gene Delivery in Cancer Cells.* Angewandte Chemie International Edition, 2013. **52**(27): p. 6926-6929.
178. Kim, J.S., et al., *ROS-induced biodegradable polythioketal nanoparticles for intracellular delivery of anti-cancer therapeutics.* Journal of Industrial and Engineering Chemistry, 2015. **21**(0): p. 1137-1142.
179. Kontoyiannis, D., et al., *Impaired On/Off Regulation of TNF Biosynthesis in Mice Lacking TNF AU-Rich Elements: Implications for Joint and Gut-Associated Immunopathologies.* Immunity, 1999. **10**(3): p. 387-398.

180. Seshadri, G., et al., *The delivery of superoxide dismutase encapsulated in polyketal microparticles to rat myocardium and protection from myocardial ischemia-reperfusion injury.* Biomaterials, 2010. **31**(6): p. 1372-1379.
181. Avci, G., et al., *Curcumin protects against ischemia/reperfusion injury in rat skeletal muscle.* Journal of Surgical Research, 2012. **172**(1): p. e39-e46.
182. Anand, P., et al., *Bioavailability of curcumin: problems and promises.* Molecular pharmaceutics, 2007. **4**(6): p. 807-818.
183. Champion, J., A. Walker, and S. Mitragotri, *Role of Particle Size in Phagocytosis of Polymeric Microspheres.* Pharmaceutical Research, 2008. **25**(8): p. 1815-1821.
184. Anderson, J.M. and M.S. Shive, *Biodegradation and biocompatibility of PLA and PLGA microspheres.* Advanced drug delivery reviews, 2012. **64**: p. 72-82.
185. Stadtman, E.R. and R.L. Levine, *Free radical-mediated oxidation of free amino acids and amino acid residues in proteins.* Amino Acids, 2003. **25**(3-4): p. 207-218.
186. Gupta, M.K., et al., *Oligoproline-derived nanocarrier for dual stimuli-responsive gene delivery.* Journal of Materials Chemistry B, 2015. **3**(36): p. 7271-7280.
187. Yu, S.S., et al., *Physiologically Relevant Oxidative Degradation of Oligo(proline) Cross-Linked Polymeric Scaffolds.* Biomacromolecules, 2011. **12**(12): p. 4357-4366.
188. Lee, S.H., et al., *ROS-cleavable proline oligomer crosslinking of polycaprolactone for pro-angiogenic host response.* Journal of Materials Chemistry B, 2014. **2**(41): p. 7109-7113.
189. McEnery, M.A.P., et al., *Oxidatively degradable poly(thioketal urethane)/ceramic composite bone cements with bone-like strength.* RSC Advances, 2016. **6**(111): p. 109414-109424.
190. Hogg, N., et al., *Production of hydroxyl radicals from the simultaneous generation of superoxide and nitric oxide.* Biochem. J, 1992. **281**: p. 419-424.
191. Vicentini, F.T.M.d.C., et al., *Delivery Systems and Local Administration Routes for Therapeutic siRNA.* Pharmaceutical Research, 2013. **30**(4): p. 915-931.
192. Whittam, A.J., et al., *Challenges and Opportunities in Drug Delivery for Wound Healing.* Advances in wound care, 2016. **5**(2): p. 79-88.
193. Jiang, B., et al., *Investigation of lysine acrylate containing poly (N-isopropylacrylamide) hydrogels as wound dressings in normal and infected wounds.* Journal of Biomedical Materials Research Part B: Applied Biomaterials, 2012. **100**(3): p. 668-676.
194. Duscher, D., et al., *Transdermal deferoxamine prevents pressure-induced diabetic ulcers.* Proceedings of the National Academy of Sciences, 2015. **112**(1): p. 94-99.
195. Saraswati, S., et al., *Pyrvinium, a potent small molecule Wnt inhibitor, promotes wound repair and post-MI cardiac remodeling.* PLoS One, 2010. **5**(11): p. e15521.
196. Mealy, J.E., C.B. Rodell, and J.A. Burdick, *Sustained small molecule delivery from injectable hyaluronic acid hydrogels through host-guest mediated retention.* Journal of Materials Chemistry B, 2015. **3**(40): p. 8010-8019.
197. Hori, K., et al., *Controlled-release of epidermal growth factor from cationized gelatin hydrogel enhances corneal epithelial wound healing.* Journal of controlled release, 2007. **118**(2): p. 169-176.
198. Brudno, Y., et al., *Enhancing microvascular formation and vessel maturation through temporal control over multiple pro-angiogenic and pro-maturation factors.* Biomaterials, 2013. **34**(36): p. 9201-9209.
199. Cai, S., et al., *Injectable glycosaminoglycan hydrogels for controlled release of human basic fibroblast growth factor.* Biomaterials, 2005. **26**(30): p. 6054-6067.
200. Senet, P., et al., *Topical treatment of hypertensive leg ulcers with platelet-derived growth factor-bb: A randomized controlled trial.* Archives of Dermatology, 2011. **147**(8): p. 926-930.
201. Hanft, J., et al., *Phase I trial on the safety of topical rhVEGF on chronic neuropathic diabetic foot ulcers.* Journal of wound care, 2008. **17**(1).
202. McCarty, S.M. and S.L. Percival, *Proteases and delayed wound healing.* Advances in wound care, 2013. **2**(8): p. 438-447.
203. Tyrone, J.W., et al., *Collagen-Embedded Platelet-Derived Growth Factor DNA Plasmid Promotes Wound Healing in a Dermal Ulcer Model.* Journal of Surgical Research, 2000. **93**(2): p. 230-236.
204. Rabbany, S.Y., et al., *Continuous delivery of stromal cell-derived factor-1 from alginate scaffolds accelerates wound healing.* Cell transplantation, 2010. **19**(4): p. 399-408.
205. Kobsa, S., et al., *An electrospun scaffold integrating nucleic acid delivery for treatment of full-thickness wounds.* Biomaterials, 2013. **34**(15): p. 3891-3901.

206. Shea, L.D., et al., *DNA delivery from polymer matrices for tissue engineering.* Nature biotechnology, 1999. **17**(6): p. 551-554.
207. Castleberry, S.A., et al., *Self-Assembled Wound Dressings Silence MMP-9 and Improve Diabetic Wound Healing In Vivo.* Advanced Materials, 2015.
208. Castleberry, S.A., et al., *Nanolayered siRNA delivery platforms for local silencing of CTGF reduce cutaneous scar contraction in third-degree burns.* Biomaterials, 2016. **95**: p. 22-34.
209. Nguyen, P.D., et al., *Improved diabetic wound healing through topical silencing of p53 is associated with augmented vasculogenic mediators.* Wound Repair and Regeneration, 2010. **18**(6): p. 553-559.
210. Pavco, P.A. *Update on Phase 2a Clinical Trial Results of RXI-109 Treatment to Reduce the Formation of Hypertrophic Dermal Scars and Keloids*. in *23rd World Congress of Dermatology*. 2015. Vancourver, Canada.
211. White, P.J., *Barriers to successful delivery of short interfering RNA after systemic administration.* Clinical and Experimental Pharmacology and Physiology, 2008. **35**(11): p. 1371-1376.
212. Dominska, M. and D.M. Dykxhoorn, *Breaking down the barriers: siRNA delivery and endosome escape.* Journal of cell science, 2010. **123**(8): p. 1183-1189.
213. Wu, Y., et al., *Mesenchymal Stem Cells Enhance Wound Healing Through Differentiation and Angiogenesis.* Stem Cells, 2007. **25**(10): p. 2648-2659.
214. Sotiropoulou, P.A., et al., *Interactions Between Human Mesenchymal Stem Cells and Natural Killer Cells.* Stem Cells, 2006. **24**(1): p. 74-85.
215. Falanga, V., et al., *Autologous bone marrow-derived cultured mesenchymal stem cells delivered in a fibrin spray accelerate healing in murine and human cutaneous wounds.* Tissue engineering, 2007. **13**(6): p. 1299-1312.
216. Ma, K., et al., *Effects of nanofiber/stem cell composite on wound healing in acute full-thickness skin wounds.* Tissue Engineering Part A, 2011. **17**(9-10): p. 1413-1424.
217. Wong, V.W., et al., *Pullulan Hydrogels Improve Mesenchymal Stem Cell Delivery into High-Oxidative-Stress Wounds.* Macromolecular Bioscience, 2011. **11**(11): p. 1458-1466.
218. Rustad, K.C., et al., *Enhancement of mesenchymal stem cell angiogenic capacity and stemness by a biomimetic hydrogel scaffold.* Biomaterials, 2012. **33**(1): p. 80-90.
219. Garg, R.K., et al., *Capillary Force Seeding of Hydrogels for Adipose-Derived Stem Cell Delivery in Wounds.* Stem Cells Translational Medicine, 2014.
220. Yoshikawa, T., et al., *Wound therapy by marrow mesenchymal cell transplantation.* Plastic and reconstructive surgery, 2008. **121**(3): p. 860-877.
221. Ichioka, S., et al., *Bone marrow-impregnated collagen matrix for wound healing: experimental evaluation in a microcirculatory model of angiogenesis, and clinical experience.* British journal of plastic surgery, 2005. **58**(8): p. 1124-1130.
222. Kirby, G.T., et al., *Stem cells for cutaneous wound healing.* BioMed research international, 2015. **2015**.
223. Li, H., et al., *Matrix Metalloproteinase Responsive, Proximity-Activated Polymeric Nanoparticles for siRNA Delivery.* Advanced Functional Materials, 2013. **23**(24): p. 3040-3052.
224. Ku, T.-H., et al., *Controlling and Switching the Morphology of Micellar Nanoparticles with Enzymes.* Journal of the American Chemical Society, 2011. **133**(22): p. 8392-8395.
225. Salvatore, R.N., et al., *A mild and highly convenient chemoselective alkylation of thiols using Cs2CO3–TBAI.* Tetrahedron Letters, 2005. **46**(51): p. 8931-8935.
226. ASTM-International, *E1899 - 08. Standard Test Method for Hydroxyl Groups Using Reaction with p-Toluenesulfonyl Isocyanate (TSI) and Potentiometric Titration with Tetrabutylammonium Hydroxide.* 2008.
227. Pike, J.K., T. Ho, and K.J. Wynne, *Water-Induced Surface Rearrangements of Poly(dimethylsiloxane−urea−urethane) Segmented Block Copolymers.* Chemistry of Materials, 1996. **8**(4): p. 856-860.
228. Schubert, M.A., et al., *Role of oxygen in biodegradation of poly(etherurethane urea) elastomers.* Journal of Biomedical Materials Research, 1997. **34**(4): p. 519-530.
229. Christenson, E.M., J.M. Anderson, and A. Hiltner, *Oxidative mechanisms of poly(carbonate urethane) and poly(ether urethane) biodegradation: In vivo and in vitro correlations.* Journal of Biomedical Materials Research Part A, 2004. **70A**(2): p. 245-255.
230. Hogg, N., et al., *Production of hydroxyl radicals from the simultaneous generation of superoxide and nitric oxide.* Biochemical Journal, 1992. **281**(2): p. 419-424.
231. Hu, Y., et al., *Fabrication of poly(α-hydroxy acid) foam scaffolds using multiple solvent systems.* Journal of Biomedical Materials Research, 2002. **59**(3): p. 563-572.

232. Karageorgiou, V. and D. Kaplan, *Porosity of 3D biomaterial scaffolds and osteogenesis.* Biomaterials, 2005. **26**(27): p. 5474-5491.
233. Mikos, A.G. and J.S. Temenoff, *Formation of highly porous biodegradable scaffolds for tissue engineering.* Electronic Journal of Biotechnology, 2000. **3**(2): p. 114-119.
234. Harbers, G.M. and D.W. Grainger, *Cell-Material Interactions: Fundamental Design Issues for Tissue Engineering and Clinical Considerations*, in *An Introduction to Biomaterials*, S.A. Guelcher and J.O. Hollinger, Editors. 2006, CRC Press, Taylor & Francis Group.
235. Arima, Y. and H. Iwata, *Effect of wettability and surface functional groups on protein adsorption and cell adhesion using well-defined mixed self-assembled monolayers.* Biomaterials, 2007. **28**(20): p. 3074-3082.
236. Eglin, D., S. Griffon, and M. Alini, *Thiol-Containing Degradable Poly(thiourethane-urethane)s for Tissue Engineering.* Journal of Biomaterials Science, Polymer Edition, 2010. **21**(4): p. 477-491.
237. Laschke, M.W., et al., *In vivo biocompatibility and vascularization of biodegradable porous polyurethane scaffolds for tissue engineering.* Acta Biomaterialia, 2009. **5**(6): p. 1991-2001.
238. Beckman, J.S. and W.H. Koppenol, *Nitric oxide, superoxide, and peroxynitrite: the good, the bad, and ugly.* American Journal of Physiology-Cell Physiology, 1996. **271**(5): p. C1424-C1437.
239. Aste-Amezaga, M., et al., *Molecular Mechanisms of the Induction of IL-12 and Its Inhibition by IL-10.* The Journal of Immunology, 1998. **160**(12): p. 5936-5944.
240. Jayakumar, A., et al., *Transcriptional Inhibition of Interleukin-12 Promoter Activity in Leishmania Spp.–Infected Macrophages.* Journal of Parasitology, 2008. **94**(1): p. 84-93.
241. Oh, S.H., et al., *Oxygen generating scaffolds for enhancing engineered tissue survival.* Biomaterials, 2009. **30**(5): p. 757-762.
242. Rockwood, D.N., et al., *Culture on electrospun polyurethane scaffolds decreases atrial natriuretic peptide expression by cardiomyocytes in vitro.* Biomaterials, 2008. **29**(36): p. 4783-4791.
243. Falanga, V., *Wound healing and its impairment in the diabetic foot.* The Lancet, 2006. **366**(9498): p. 1736-1743.
244. Kim, S.Y. and E.G. Yang, *Recent Advances in Developing Inhibitors for Hypoxia-Inducible Factor Prolyl Hydroxylases and Their Therapeutic Implications.* Molecules, 2015. **20**(11): p. 20551-20568.
245. Takeda, K., et al., *Regulation of adult erythropoiesis by prolyl hydroxylase domain proteins.* Blood, 2008. **111**(6): p. 3229-3235.
246. Cowburn, A.S., et al., *Epidermal Deletion of HIF-2α Stimulates Wound Closure.* Journal of Investigative Dermatology, 2014. **134**(3): p. 801-808.
247. Dykxhoorn, D., D. Palliser, and J. Lieberman, *The silent treatment: siRNAs as small molecule drugs.* Gene therapy, 2006. **13**(6): p. 541-552.
248. Miteva, M., et al., *Tuning PEGylation of mixed micelles to overcome intracellular and systemic siRNA delivery barriers.* Biomaterials, 2015. **38**: p. 97-107.
249. Sarett, S.M., et al., *Conjugation of palmitic acid improves potency and longevity of siRNA delivered via endosomolytic polymer nanoparticles.* Journal of Biomedical Materials Research Part A, 2015. **103**(9): p. 3107-3116.
250. Convertine, A.J., et al., *pH-Responsive Polymeric Micelle Carriers for siRNA Drugs.* Biomacromolecules, 2010. **11**(11): p. 2904-2911.
251. Krebs, M.D. and E. Alsberg, *Localized, Targeted, and Sustained siRNA Delivery.* Chemistry – A European Journal, 2011. **17**(11): p. 3054-3062.
252. Almquist, B.D., et al., *Combination growth factor therapy via electrostatically assembled wound dressings improves diabetic ulcer healing in vivo.* Advanced Healthcare Materials, 2015. **4**(14): p. 2090-2099.
253. Kundu, K., et al., *Hydrocyanines: A Class of Fluorescent Sensors That Can Image Reactive Oxygen Species in Cell Culture, Tissue, and In Vivo.* Angewandte Chemie International Edition, 2009. **48**(2): p. 299-303.
254. Davidson, J.M., F. Yu, and S.R. Opalenik, *Splinting strategies to overcome confounding wound contraction in experimental animal models.* Advances in wound care, 2013. **2**(4): p. 142-148.
255. Lee, S.Y., et al., *In vivo conjunctival reconstruction using modified PLGA grafts for decreased scar formation and contraction.* Biomaterials, 2003. **24**(27): p. 5049-5059.
256. Vairamon, S.J., M. Babu, and V. Viswanathan, *Oxidative stress markers regulating the healing of foot ulcers in patients with type 2 diabetes.* Wounds, 2009. **21**(10): p. 273-279.
257. Arya, A.K., D. Pokharia, and K. Tripathi, *Relationship between oxidative stress and apoptotic markers in lymphocytes of diabetic patients with chronic non healing wound.* Diabetes Research and Clinical Practice, 2011. **94**(3): p. 377-384.

258. Murray, P.J. and T.A. Wynn, *Protective and pathogenic functions of macrophage subsets.* Nat Rev Immunol, 2011. **11**(11): p. 723-737.
259. Kaushik, J.K. and R. Bhat, *Why is trehalose an exceptional protein stabilizer? An analysis of the thermal stability of proteins in the presence of the compatible osmolyte trehalose.* Journal of Biological Chemistry, 2003. **278**(29): p. 26458-26465.
260. Strutz, F., et al., *Identification and characterization of a fibroblast marker: FSP1.* The Journal of Cell Biology, 1995. **130**(2): p. 393-405.
261. Opalenik, S.R. and J.M. Davidson, *Fibroblast differentiation of bone marrow-derived cells during wound repair.* The FASEB Journal, 2005. **19**(11): p. 1561-1563.
262. Lorden, E.R., et al., *Mitigation of hypertrophic scar contraction via an elastomeric biodegradable scaffold.* Biomaterials, 2015. **43**: p. 61-70.
263. Shekaran, A., et al., *Bone regeneration using an alpha 2 beta 1 integrin-specific hydrogel as a BMP-2 delivery vehicle.* Biomaterials, 2014. **35**(21): p. 5453-5461.
264. Gutowski, S.M., et al., *Protease-degradable PEG-maleimide coating with on-demand release of IL-1Ra to improve tissue response to neural electrodes.* Biomaterials, 2015. **44**: p. 55-70.
265. Foster, G.A., et al., *Protease-degradable microgels for protein delivery for vascularization.* Biomaterials, 2017. **113**: p. 170-175.
266. Headen, D.M., et al., *Microfluidic-Based Generation of Size-Controlled, Biofunctionalized Synthetic Polymer Microgels for Cell Encapsulation.* Advanced Materials, 2014. **26**(19): p. 3003-3008.
267. Ma, N., et al., *Dual Redox Responsive Assemblies Formed from Diselenide Block Copolymers.* Journal of the American Chemical Society, 2009. **132**(2): p. 442-443.
268. Martin, J.R., et al., *Local Delivery of PHD2 siRNA from ROS-Degradable Scaffolds to Promote Diabetic Wound Healing.* Advanced Healthcare Materials, 2016: p. n/a-n/a.
269. Raeber, G.P., M.P. Lutolf, and J.A. Hubbell, *Molecularly Engineered PEG Hydrogels: A Novel Model System for Proteolytically Mediated Cell Migration.* Biophysical Journal, 2005. **89**(2): p. 1374-1388.
270. Caliari, S.R. and J.A. Burdick, *A practical guide to hydrogels for cell culture.* Nat Meth, 2016. **13**(5): p. 405-414.
271. Fairbanks, B.D., et al., *A Versatile Synthetic Extracellular Matrix Mimic via Thiol-Norbornene Photopolymerization.* Advanced Materials, 2009. **21**(48): p. 5005-5010.
272. Ulbricht, J., R. Jordan, and R. Luxenhofer, *On the biodegradability of polyethylene glycol, polypeptoids and poly (2-oxazoline) s.* Biomaterials, 2014. **35**(17): p. 4848-4861.
273. Hern, D.L. and J.A. Hubbell, *Incorporation of adhesion peptides into nonadhesive hydrogels useful for tissue resurfacing.* Journal of Biomedical Materials Research, 1998. **39**(2): p. 266-276.
274. Artzi, N., et al., *In vivo and in vitro tracking of erosion in biodegradable materials using non-invasive fluorescence imaging.* Nat Mater, 2011. **10**(9): p. 704-709.
275. Kim, S.H., et al., *Near-Infrared Fluorescence Imaging for Noninvasive Trafficking of Scaffold Degradation.* Sci. Rep., 2013. **3**: p. 1-7.
276. Cai, L., R.E. Dewi, and S.C. Heilshorn, *Injectable Hydrogels with In Situ Double Network Formation Enhance Retention of Transplanted Stem Cells.* Advanced Functional Materials, 2015: p. n/a-n/a.
277. Sullivan, T.P., et al., *The pig as a model for human wound healing.* Wound repair and regeneration, 2001. **9**(2): p. 66-76.
278. Brown, B.N., et al., *Macrophage phenotype as a predictor of constructive remodeling following the implantation of biologically derived surgical mesh materials.* Acta Biomaterialia, 2012. **8**(3): p. 978-987.
279. Guo, R., et al., *Substrate modulus of 3D-printed scaffolds regulates the regenerative response in subcutaneous implants through the macrophage phenotype and Wnt signaling.* Biomaterials, 2015. **73**: p. 85-95.
280. Duvall, C.L., et al., *Poly(thioketal-urethane) scaffolds and methods of use.* 2016.
281. Gould, L.J., et al., *Optimization and validation of an ischemic wound model.* Wound Repair and Regeneration, 2005. **13**(6): p. 576-582.
282. Watanabe, Y., et al., *Glutathione adducts induced by ischemia and deletion of glutaredoxin-1 stabilize HIF-1α and improve limb revascularization.* Proceedings of the National Academy of Sciences, 2016. **113**(21): p. 6011-6016.

Appendix

Appendix A - Chapter 3 Supplementary Information

A Porous Tissue Engineering Scaffold Selectively Degraded by Cell-Generated Reactive Oxygen Species

John R. Martin, Mukesh K. Gupta, Jonathan M. Page, Fang Yu, Jeffrey M. Davidson, Scott A. Guelcher, Craig L. Duvall

Appendix Contents:

- A.1 PTK polymer and scaffold characterization
- A.2 PTK-UR and PEUR *in vitro* scaffold degradation
- A.3 Scaffold cytocompatibility

A.1 PTK polymer and scaffold characterization

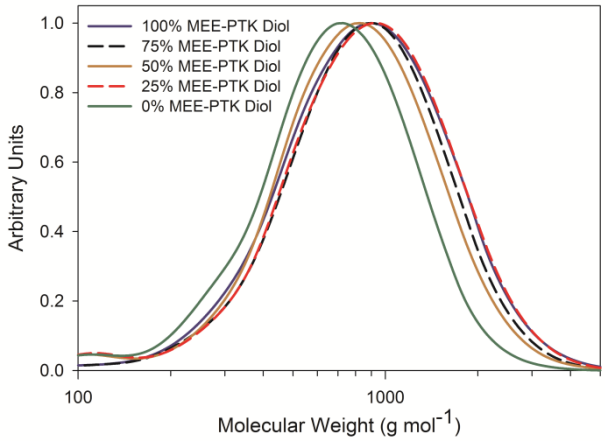

Figure A1 GPC chromatograms of PTK diols

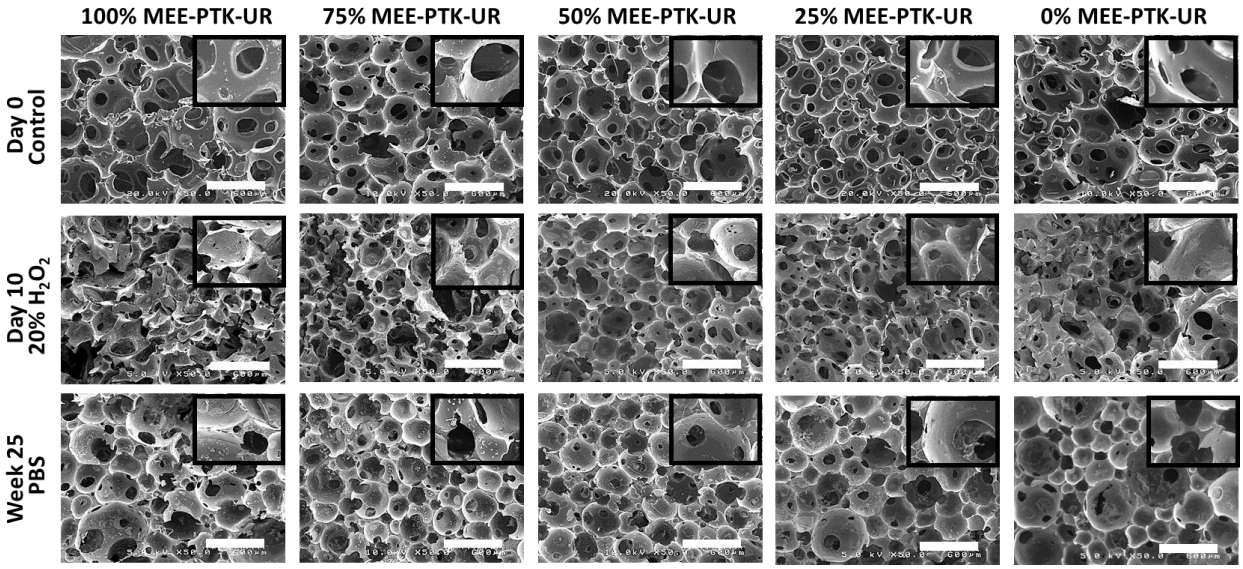

Figure A2. SEM images of PTK-UR scaffolds. Day 0 samples (top row) show representative untreated scaffolds. The day 10 degradation samples (middle row) were incubated in 20% H_2O_2 in 0.1M $CoCl_2$ for 10 days at 37°C to demonstrate oxidative degradation of the PTK-URs (note visible changes in structure of "macro-pores" and appearance of "micro-pores" in the struts of the scaffold). Week 25 PBS samples (bottom row) were incubated in PBS for 25 weeks at 37°C to demonstrate the resistance of the PTKs to hydrolytic breakdown. White scale bar represents 600 μm, and the inset images display higher magnification views (2.6x magnification of large image).

Table A1. Thermomechanical properties of PTK-UR and PEUR scaffolds and neat polymers.

	Polymer	***Scaffold***	
	DSC T_g (°C)	**DSC T_g (°C)**	**DMA T_g (°C)**
100% MEE-PTK	-66.1	-25.2	20.7
75% MEE-PTK	-67.7	-36.0	14.9
50% MEE-PTK	-78.5	-11.1	13.9
25% MEE-PTK	-72.9	-27.9	20.3
0% MEE-PTK	-76.8	-19.3	23.1
900 Triol Polyester	-47.7	-1.7	34.4
1500 Triol Polyester	-56.9	-26.4	24.7
1000 Diol Polyester	-43.1	-30.1	18.2

A.2 PTK-UR and PEUR *in vitro* scaffold degradation

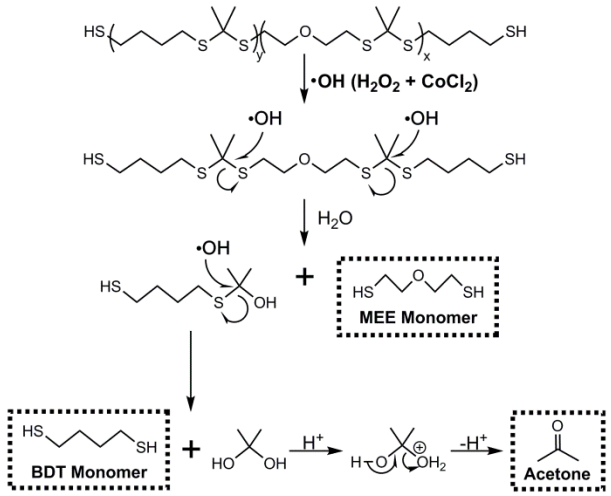

Figure A3. Proposed mechanism for hydroxyl radical degradation of PTK polymers.

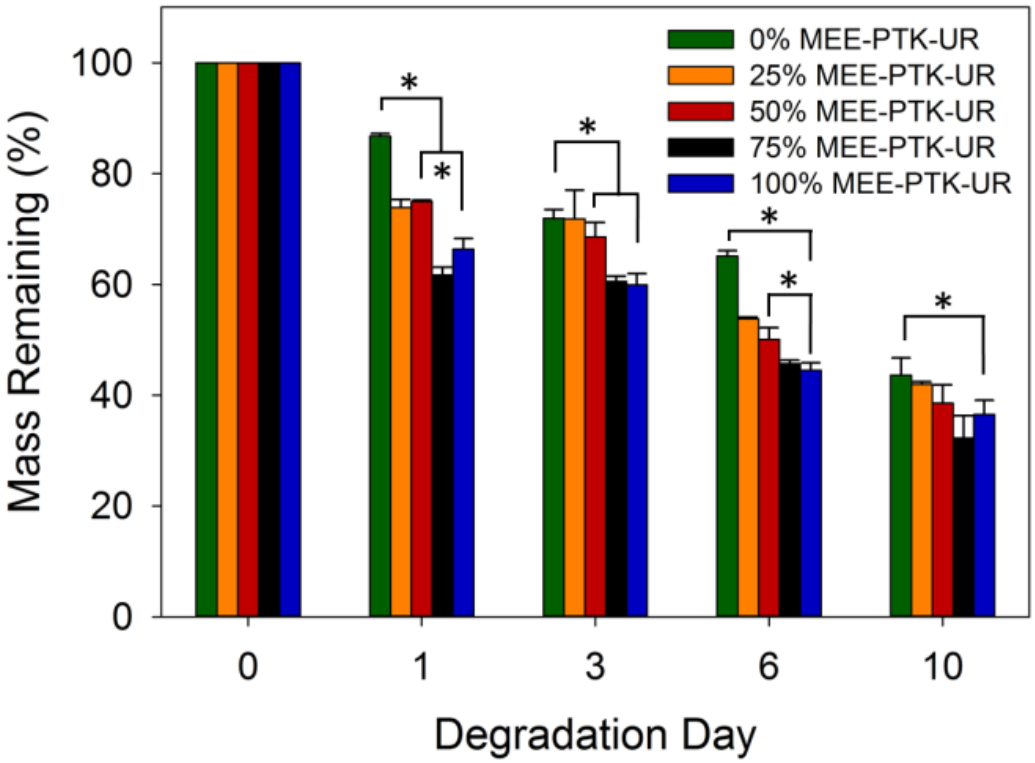

Figure A4. *In vitro* degradation of full set of PTK-UR scaffolds incubated in accelerated oxidative conditions (20% H_2O_2 in 0.1M $CoCl_2$). For simplicity, only 100%, 50%, and 0% MEE-PTK-UR samples were displayed with statistical comparisons (*$p < 0.05$).

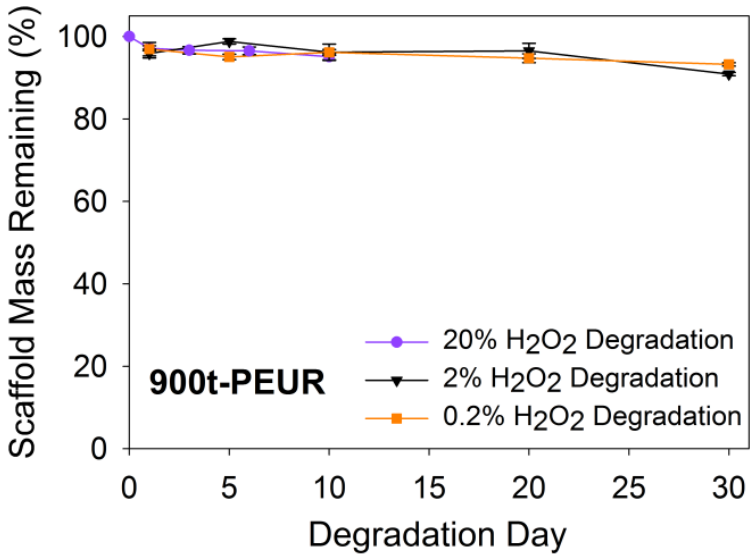

Figure A5. H_2O_2 dose-dependent degradation of 900t-PEUR scaffolds.

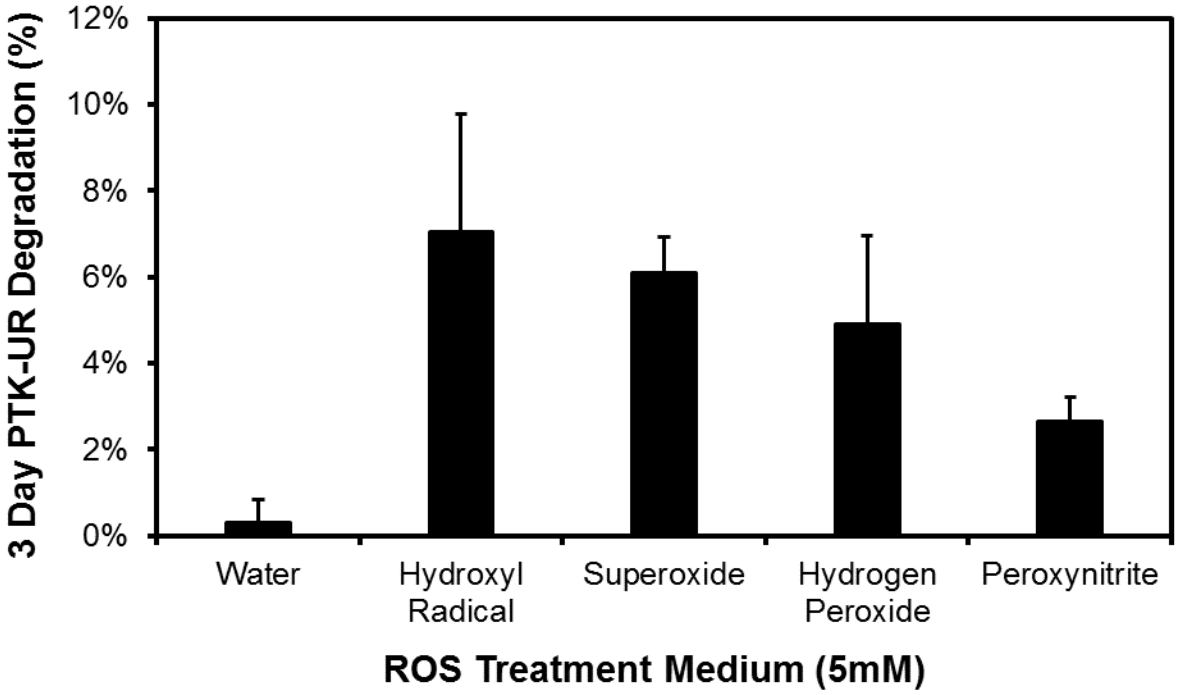

Figure A6. *In vitro* degradation of PTK-UR (LTI) scaffolds in varying ROS media. Scaffolds were incubated in water or different ROS media containing 5mM of hydrogen peroxide with $CoCl_2$ (produces hydroxyl radicals), 5mM potassium superoxide, 5mM hydrogen peroxide, or 5mM SIN-1 (produces peroxynitrite) for three days and then weighed for mass loss. Scaffolds incubated in the different ROS were all significantly degraded compared to samples incubated in water ($p<0.05$).

A.3 Scaffold cytocompatibility

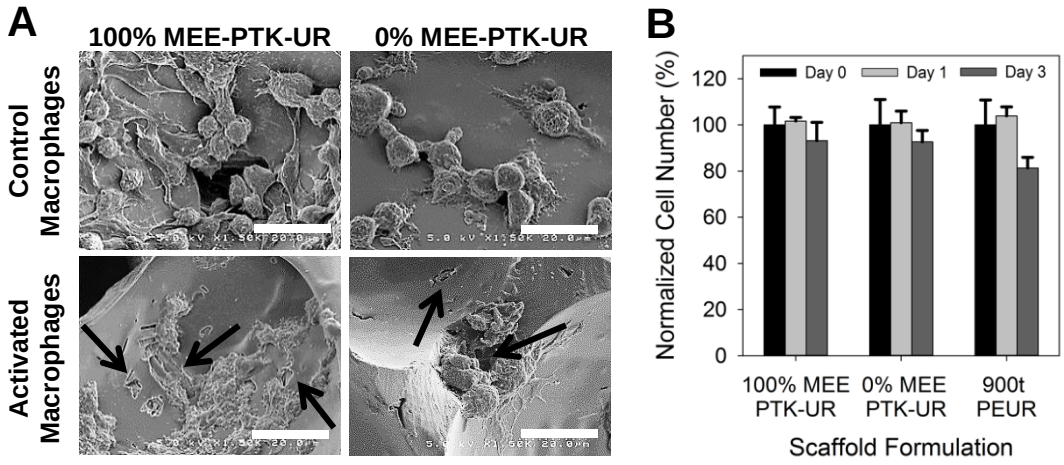

Figure A7. *In vitro* cell-mediated degradation and cytocompatibility of PTK-UR scaffolds. (A) PTK-UR scaffolds seeded with RAW 267.4 macrophages and incubated for 3 days in either control or activation media (containing LPS and IFN-γ). Qualitatively, it appears that the activated macrophages generated pitting on the scaffold surface (black arrows), potentially indicating ROS-dependent cell-mediated scaffold degradation. Scale bar = 20 μm. (B) *In vitro* cytotoxicity evaluation of porous 3D PTK-UR scaffolds. The bioluminescence (indicative of cell number) from 3T3 fibroblast-seeded scaffolds was normalized to day 0 values and remained stable over 3 days in culture.

Appendix B - Chapter 4 Supplementary Information

A Porous Tissue Engineering Scaffold Selectively Degraded by Cell-Generated Reactive Oxygen Species
John R. Martin, Mukesh K. Gupta, Jonathan M. Page, Fang Yu, Jeffrey M. Davidson, Scott A. Guelcher, Craig L. Duvall

Local delivery of PHD2 siRNA from ROS-degradable scaffolds to promote diabetic wound healing
John R. Martin, Christopher E. Nelson, Mukesh K. Gupta, Fang Yu, Samantha M. Sarett, Kyle M. Hocking, Alonda C. Pollins, Lillian B. Nanney, Jeffrey M. Davidson, Scott A. Guelcher, Craig L. Duvall

Appendix Contents:

- B.1 Characterization of subcutaneous scaffold implants
- B.2 Characterization of excisional wound scaffold implants
- B.3 Scaffold-mediated delivery of PHD2 siRNA in diabetic excisional wounds

B.1 Characterization of subcutaneous scaffold implants

Table A2. PTK-UR and PEUR scaffold components

Component	*PPHP*	*Mass (mg)*	*Component*	*PPHP*	*Mass (mg)*
PTK Diol (1100 g/mol)	100.0	69.5	PE Triol (900 g/mol)	100.0	62.7
Water	1.5	1.0	Water	1.5	0.9
TEGOAMIN33	2.3	1.6	TEGOAMIN33	2.3	1.4
Calcium stearate	4.0	2.8	Calcium stearate	4.0	2.5
LTI	36.1	25.1	LTI	51.8	32.5

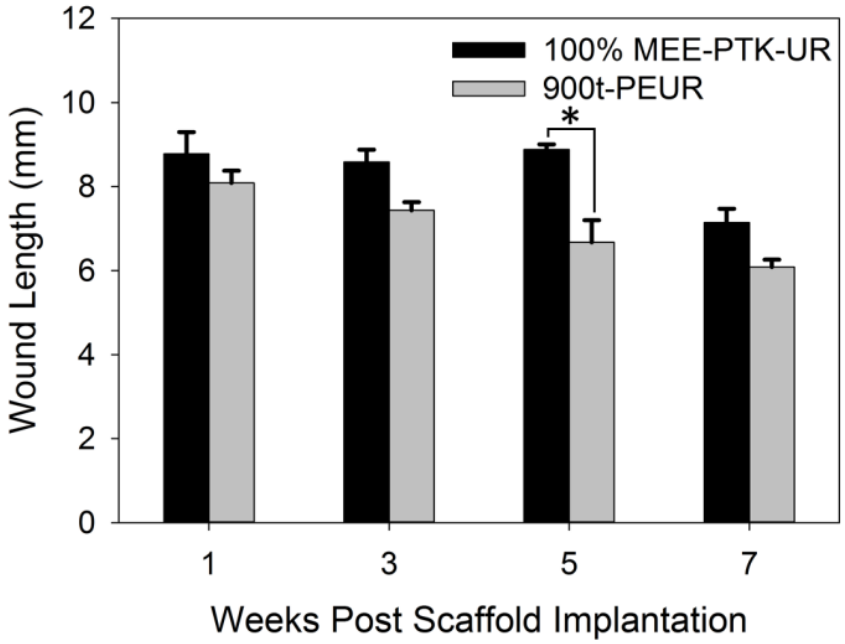

Figure A8. Subcutaneous wound lengths of implanted 100% MEE-PTK-UR and 900t-PEUR scaffolds made with HDIt over 7 weeks, *$p < 0.05$.

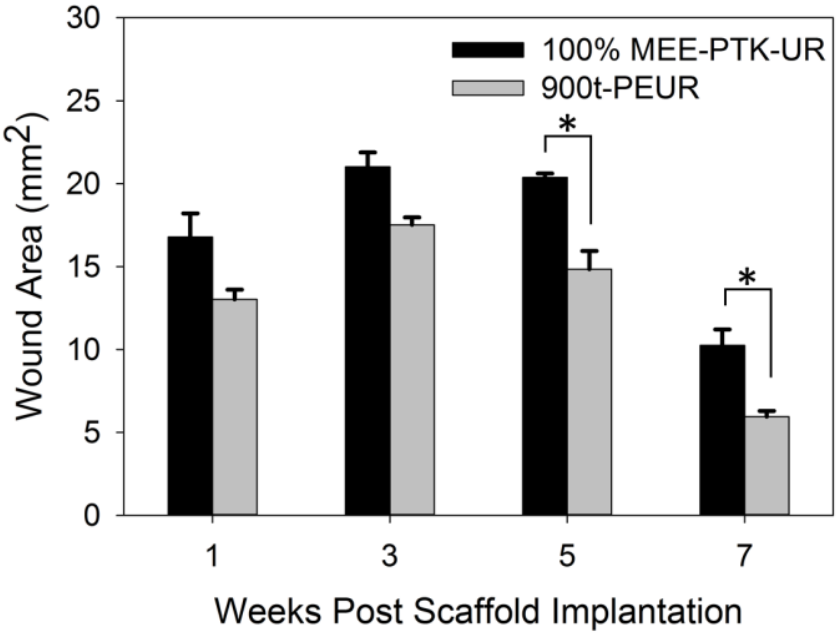

Figure A9. Subcutaneous wound areas of implanted 100% MEE-PTK-UR and 900t-PEUR scaffolds made with HDIt over 7 weeks, *$p < 0.05$.

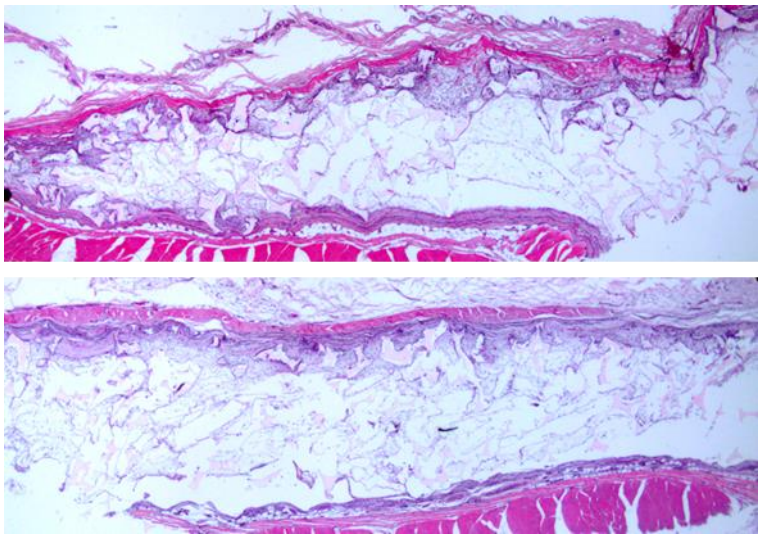

Figure A10. PTK-UR scaffolds made with LTI implanted subcutaneously in rats for 7-days.

B.2 Characterization of excisional wound scaffold implants

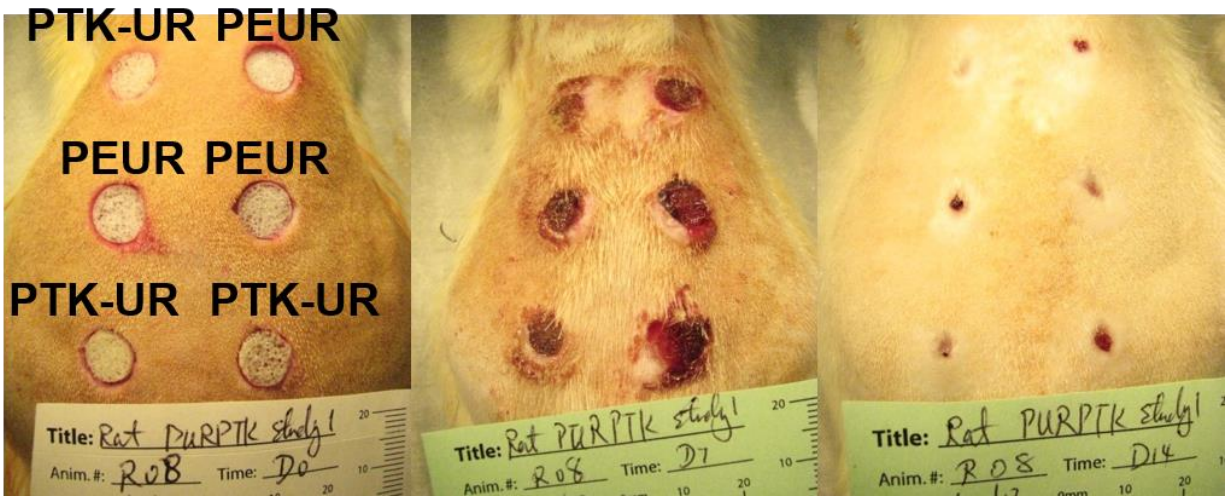

Figure A11. Diabetic rats with excisional wounds and implanted PEUR and PTK-UR scaffolds at day 0, day 7, and day 14 post surgery.

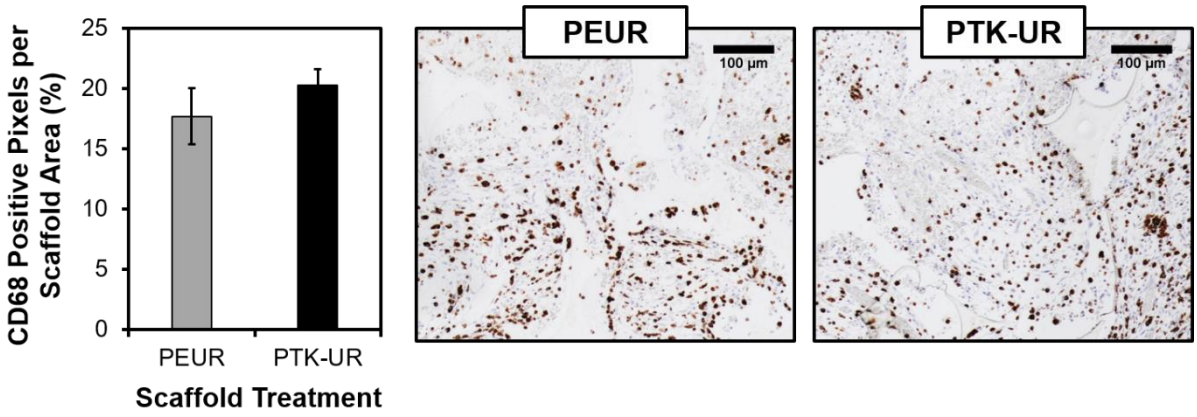

Figure A12. Macrophage presence in PEUR and PTK-UR scaffolds. There was no statistical difference in macrophage number between PEUR and PTK-UR scaffolds at day 7 post implantation in diabetic rats as quantitatively determined from CD68 IHC tissue sections.

B.3 Scaffold-mediated delivery of PHD2 siRNA in diabetic excisional wounds

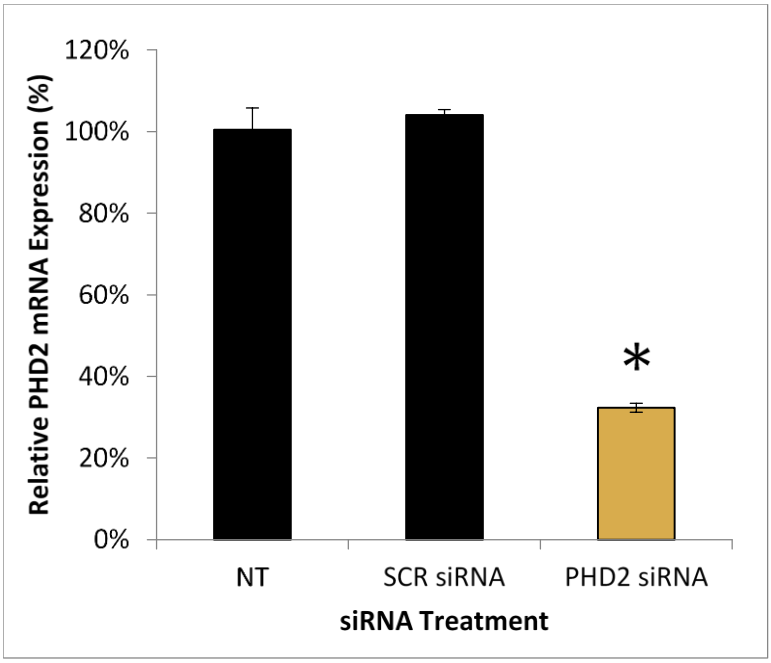

Figure A13. *In vitro* screen of PHD2 siRNA in A7r5 rat smooth muscle cells by qRT-PCR (*p<0.05).

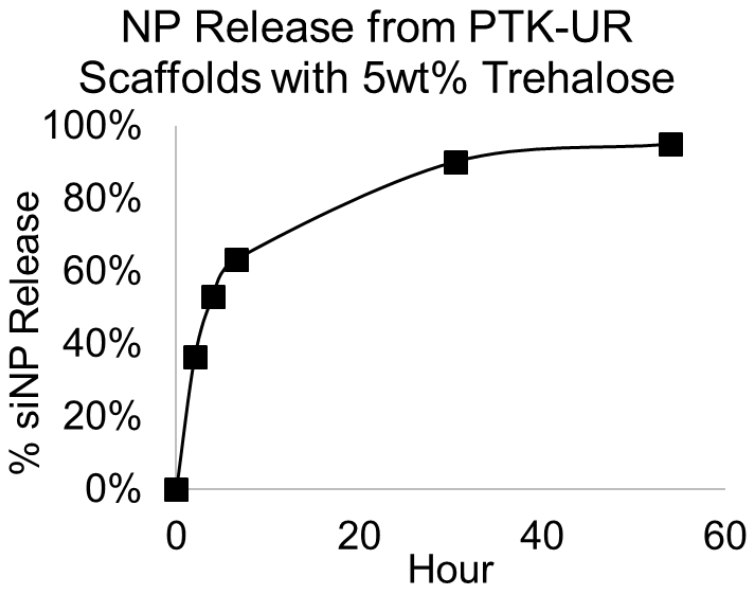

Figure A14. *In vitro* release of nanoparticles with 5wt% trehalose from PTK-UR (LTI) scaffolds. Nanoparticles were loaded with fluorescently labeled double-stranded DNA as a model for siRNA.

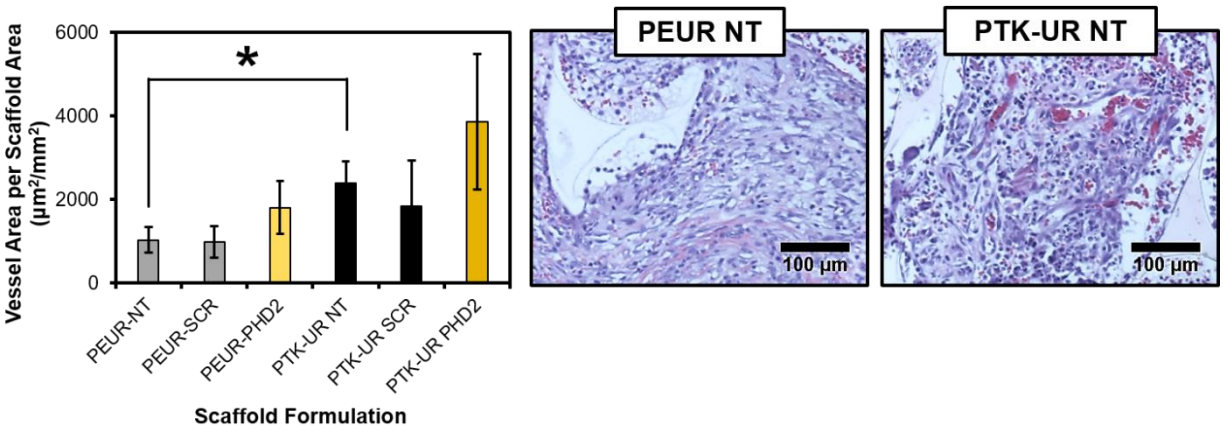

Figure A15. Initial *in vivo* screen of PEUR and PTK-UR scaffolds made with LTI for both baseline vascularization and stimulation of vascularization through PHD2 siNP delivery (mean ± SEM, n = 4 independent samples, *p<0.05).

Table A3. Nucleic acid sequences.

Name	Sequence
Scrambled siRNA	DS Scrambled Neg – From IDT
PHD2 siRNA	S: 5'-GGUACGCAAUAACCGUUUGGUAUTT-3' AS: 5'-AAAUACCAAACGGUUAUUGCGUACCUU-3'
GAPDH Primers	FWD: 5'-CTCACTCAAGATTGTCAGCAATG-3' REV: 5'-GAGGGAGATGCTCAGTGTTGG-3'
PPIB Primers	FWD: 5'-TTCCATCGTGTCATCAAG-3' REV: 5'-GAAGAACTGGGAGCCATT-3'
PHD2 Primers	FWD: 5'-ATCTCACAGGTGAGAAAGGT-3' REV: 5'-ACAGAAGGCAACTGAGAG-3'

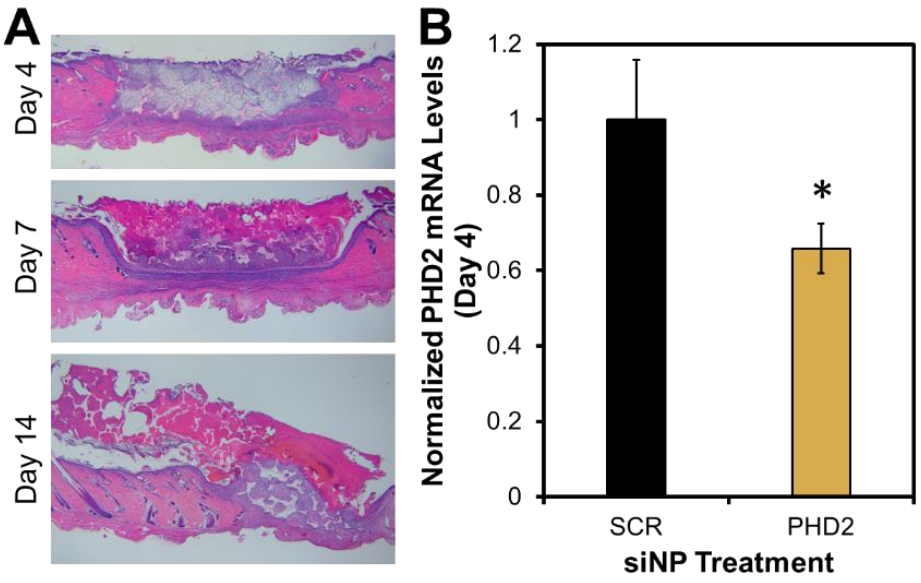

Figure A16. PTK-UR scaffolds made with HDIt and containing PHD2 siRNA nanoparticles were (A) implanted in diabetic rat excisional wounds over 14 days. Scaffolds with PHD2 siRNA had a significicant decrease in PHD2 mRNA at day 4 post implantation.

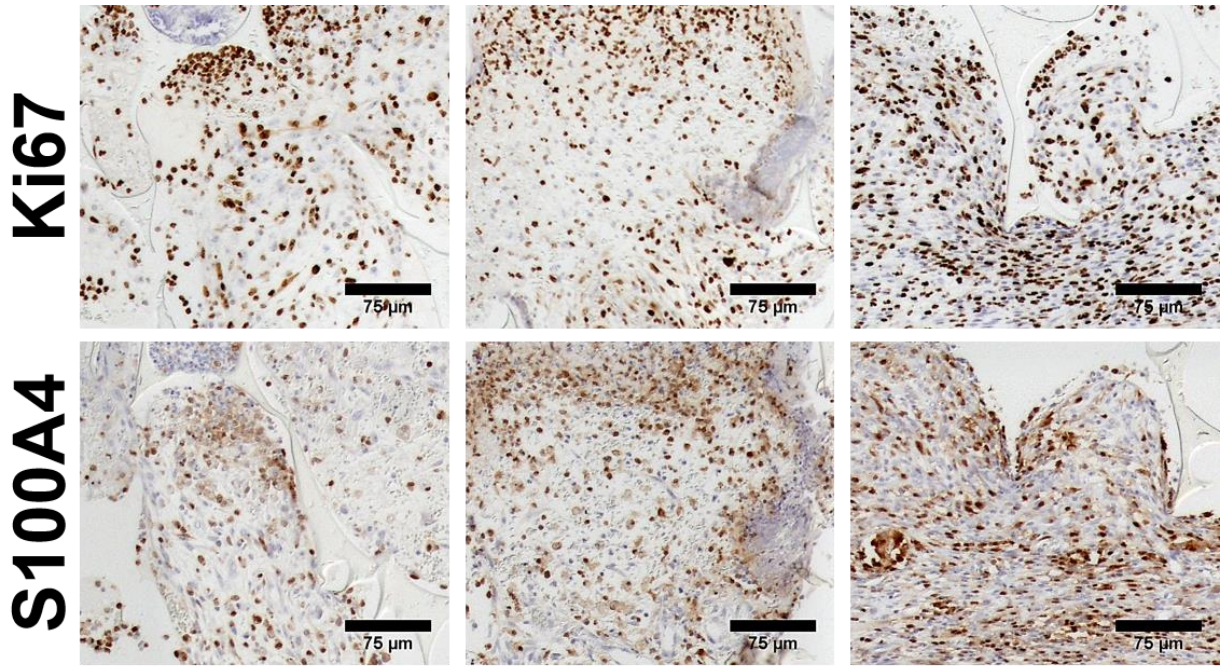

Figure A17. Representative comparison of Ki67 and S100A4 IHC staining. Serial tissue sections taken from day 7 PHD2-siNP implants (PTK-UR made with LTI), stained for either Ki67 (proliferating cells) or S100A4 (fibroblast marker), indicate that the proliferating cells are fibroblastic in nature.

Appendix C - Chapter 5 Supplementary Information

Enhanced Cell Viability and *In Vivo* Degradation of Injectable, Reactive Oxygen Species-Sensitive PEG Hydrogels

John R. Martin, Prarthana Patil, Mukesh K. Gupta, Craig L. Duvall

Appendix Contents:

- C.1 Physical characterization of PEG-MAL hydrogels
- C.2 Alternate strategy for synthesis of water-soluble PTK polymers

C.1 Physical characterization of PEG-MAL hydrogels

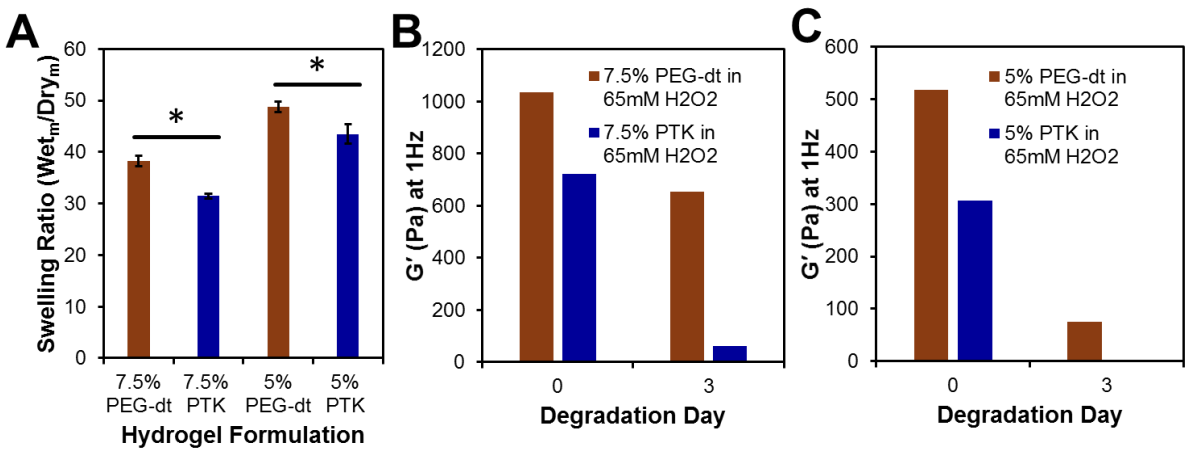

Figure A18 Physical characterization of hydrogels. (A) Swelling ratios of 7.5 and 5wt% PEG-dt and PTK hydrogels indicates that PEG-dt gels swell with more water than PTK gels. The lower wt% gels also swell more than the 7.5wt% materials. (B) 7.5wt% gels and (C) 5wt% gels made with both PEG-dt and PTK crosslinkers have decreased mechanical properties after three days of incubation in 65mM H_2O_2, though PTK modulus values are more decreased.

C.2 Alternate strategy for synthesis of water-soluble PTK polymers

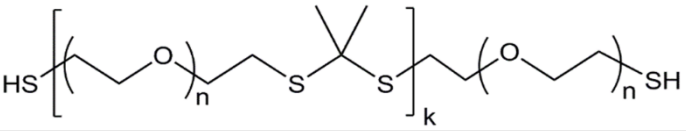

PTK Hydrophilicity

Polymer Designation	"n" ethylene glycol units per monomer	M_n	PDI	"k" thioketal units per polymer	Water Solubility
MEE-PTK (140PEG-PTK)	1	960	1.35	4.2	✗
EDDT-PTK (180PEG-PTK)	2	875	1.28	3.1	✗
300PEG-PTK	5	800	1.57	1.2	✗
600PEG-PTK	12	1310	1.65	1.0	✓

Figure A19. Alternatively pursued strategy for synthesizing hydrophilic PTK polymers. Increasing the number of ethylene glycol units per initial dithiol monomer increases the final polymer solubility, but a completely water-soluble PTK polymer was only achieved a PEG dithiol with n=12 ethylene glycols. However, the reaction efficiency and degree of polymerization (k thioketal units) decreases with increasing monomer molecular weight.

Appendix D - Chapter 6 Supplementary Information

Appendix Contents:

- D.1 Ischemic wound healing model in rats
- D.2 Ischemic wound healing model in pigs

D.1 Ischemic wound healing model in rats

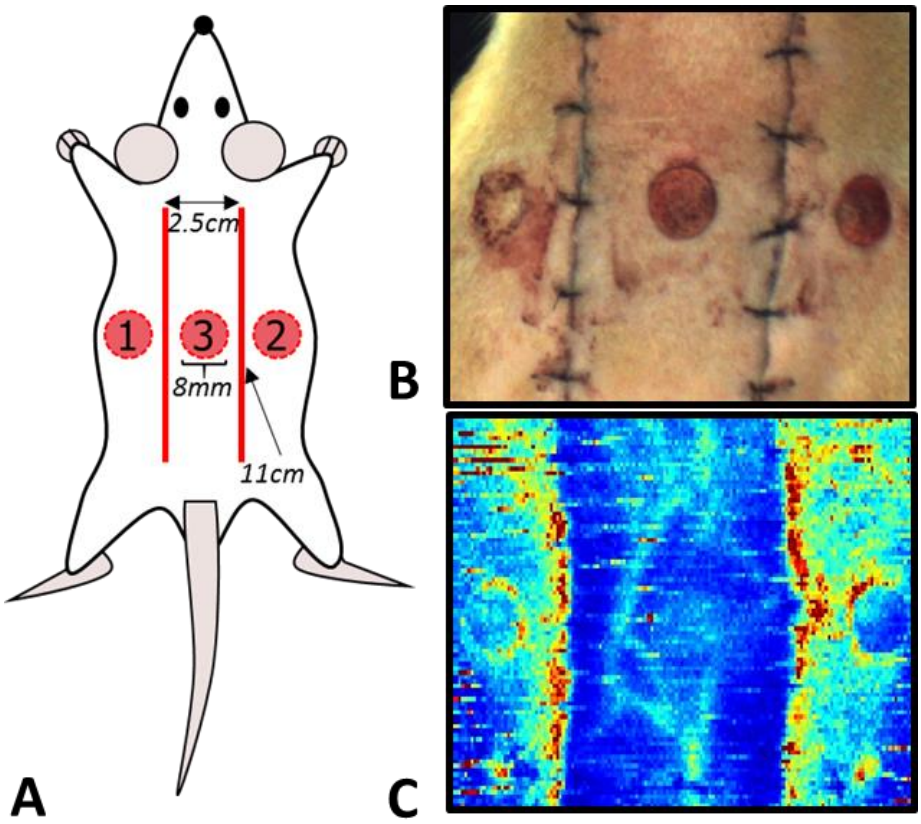

Figure A20. Optimized rat ischemic flap model featuring (A) one ischemic skin wound with two non-ischemic control wounds. (B) Flap and wounds at 1-day post-surgery with (C) laser Doppler perfusion image, highlighting the lack of blood flow in the ischemic flap skin (blue areas = less perfusion, red areas = high perfusion).

D.2 Ischemic wound healing model in pigs

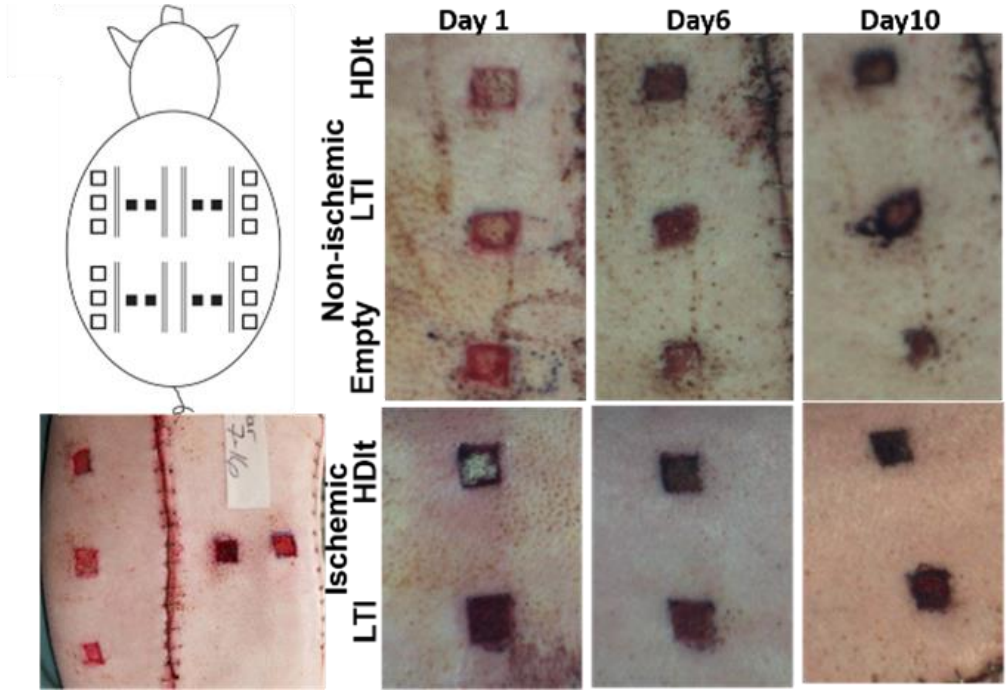

Figure A21. Impaired porcine wound healing model featuring surgical ischemic skin flaps. The 10cm x 15cm bipedicle flaps are raised from the underlying muscle to create a region of ischemia, and 1cm x 1cm wounds are placed in the flap and non-ischemic skin as controls. Wounds are either left empty or filled with PTK-UR scaffolds made with LTI or HDIt.

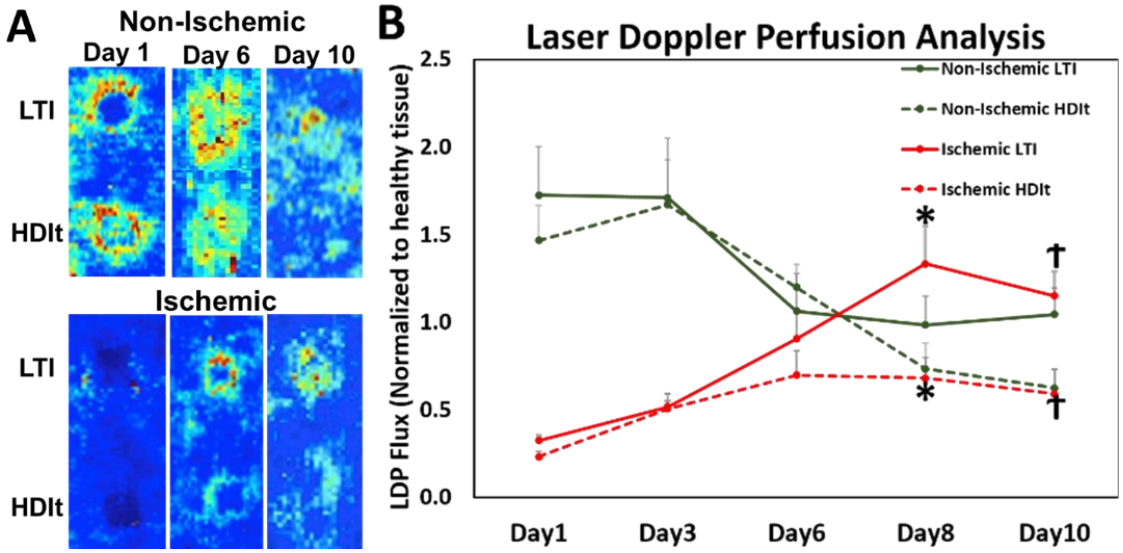

Figure A22. Laser Doppler perfusion imaging of blood flow in wound-implanted PTK-UR scaffolds and the surrounding tissue demonstrates that (A) the surgical flap creates ischemia compared to normal skin. Though the re-establishment of blood flow in HDIt vs LTI PTK-UR scaffolds is the same in normal skin, LTI materials create more perfusion than HDIt implants in the ischemic wounds.

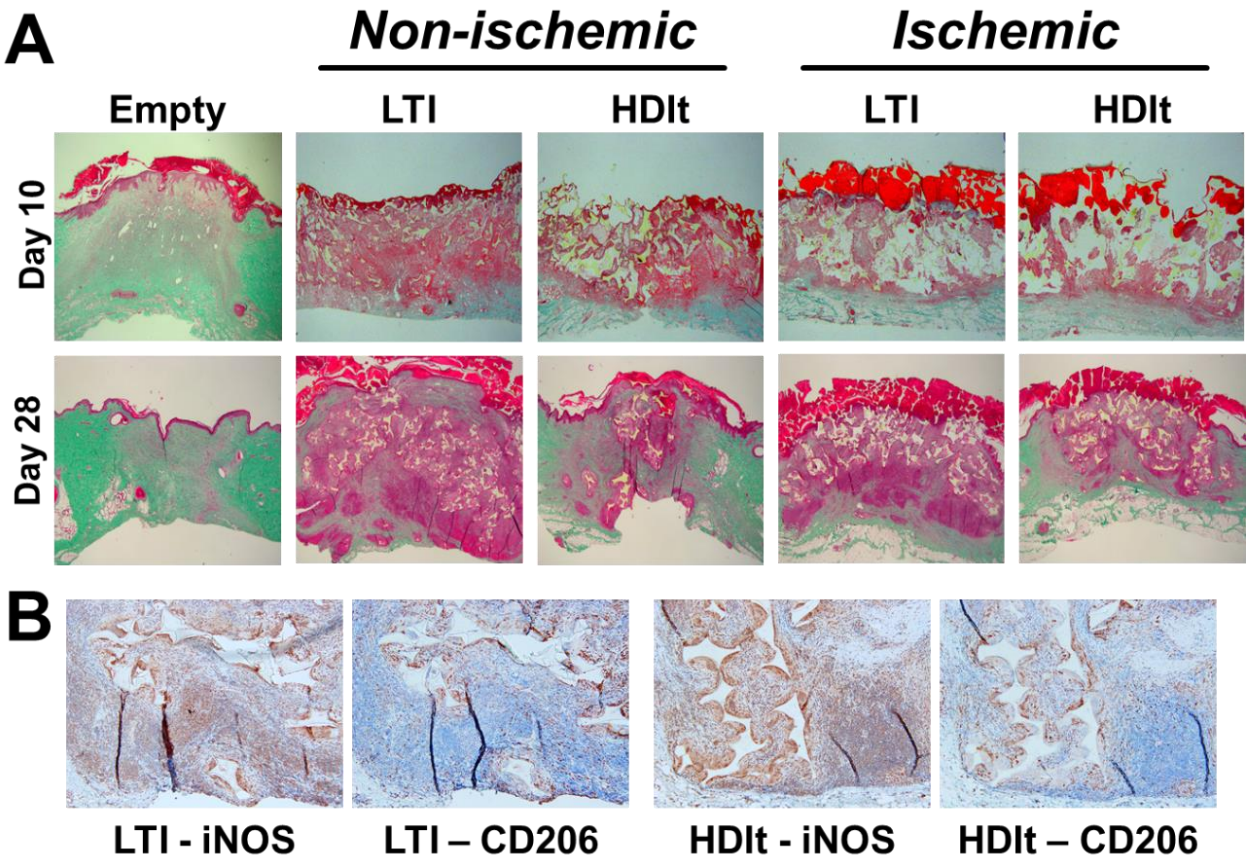

Figure A23. Histology of PTK-UR scaffolds in ischemic and non-ischemic porcine wounds. (A) Ischemic wounds generate less tissue infiltration into both scaffold formulations compared to non-ischemic wounds at day 10, though infiltration is more complete at day 28. There is more LTI scaffold present in the wounds at day 28 compared to HDIt, indicating that the HDIt materials could have been extruded from the wound rather than integrated with new tissue. (B) IHC for iNOS and CD206 at day 28 indicates that iNOS+ cells are present in the cell-dense regions surrounding the scaffold remnants, potentially indicating an inflammatory response, while CD206+ cells are directly in contact with the scaffold remnants.

Appendix E - Detailed Protocols and Additional Unpublished Data

Appendix Contents:

- E.1 PTK-UR scaffold fabrication
- E.2 siNP delivery from PTK-UR scaffolds for *in vivo* PHD2 knockdown
- B.3 Rat ischemic wound model

E.1 PTK-UR scaffold fabrication

PTK-UR or PEUR scaffolds can be fabricated in a variety of molds to yield final materials that have certain geometries, including microcentrifuge tubes (circular geometry, ~8mm diameter), soft-plastic polyethylene tubes (circular geometry, 6 or 10mm diameter), or even disposable UV-VIS cuvettes (square geometry, 1cm x 1cm). The scaffold precursor components can be directly mixed (by hand or with the Hauschild DAC 150 FVZ-K SpeedMixer) and allowed to react in these vessels, or they can pre-mixed in a larger container and then transferred before gelation to a final vessel. A number of tri-functional isocyanates can be used in scaffold fabrication, including hexamethylene diisocyanate trimer (HDIt), lysine triisocyanate (LTI), or LTI chain extended with a linear 2000g/mol PEG diol (LTI-PEG). Polyurethane scaffolds can be made in many formats, but are most often utilized as foams, cements, or films. This format is primarily determined by the catalyst chosen; the tertiary amine catalyst TEGOAMIN33, composed of 33 wt% triethylene diamine (TEDA) in dipropylene glycol, is a blowing catalyst and is the first choice for making polyurethane foams. An iron(III) acetylacetonate (FeAA) catalyst is the first choice for the fabrication of more cement-like polyurethanes, while the organobismuth catalyst Coscat83 is often used to make polyurethane films.

A successfully fabricated polyurethane foam balances the foaming and gelling reactions so that both proceed in a controlled fashion to make a homogenous porous architecture. A standard foam is made up of the polyol, the isocyanate, the catalyst, water to drive the foaming reaction, a “pore opener”, and a “pore stabilizer” if needed. The polyol reacts with the isocyanate to form the actual polyurethane matrix, while the TEGOAMIN33 catalyst drives both this gelling reaction and also the reaction of water with isocyanate groups to produce CO_2 bubbles that create the foaming. The amount of TEGOAMIN33 needed to make proper foams varies with the different isocyanates; in terms of parts per hundred parts polyol (PPHP), HDIt requires 10PPHP, LTI requires 2.3PPHP, and LTI-PEG requires 2.7PPHP. The pore opener, typically calcium stearate, is included in the reaction mix to promote connectivity between the forming pores. The pore stabilizer, sulfated castor oil, acts as a surfactant and decreases the surface tension of the gas bubbles

in the foaming polyurethane, encouraging large bubbles to burst and form smaller bubbles that yield a more homogenous porous architecture.

For fabricating a polyurethane foam with a new batch of polyol (PTK or polyester as either a diol or triol), there are a number of variables that can be tweaked to yield an optimum foam. The first variable is the effective hydroxyl content of the polyol, or how many primary hydroxyl groups are available to react with the isocyanate groups. This is usually determined from either the theoretical number of hydroxyl groups from the polymer's molecular weight (MW), or from a titration assay to determine hydroxyl content in the polymer. Once an estimated effective polyol molecular weight is determined, good practice is to make some foams using the estimated MW and then foams using the estimated MW at 125% and 75% its estimated value. Once the three foams are fabricated, they can be weighed, then incubated in dichloromethane (DCM) overnight, and finally dried and weighed again. The DCM will extract any foam components that are not covalently linked to the crosslinked polymer network, and the foam's reaction efficiency can be determined from the ratio of the foam weight post and pre-DCM incubation. The MW value that yields the foam with the highest reaction efficiency can then be used for fabricating polyurethane foams with that batch of polyol.

The final variables that can be tweaked are the relative amounts of water and pore stabilizer used in the foam. The amount of foaming is **highly** sensitive to the amount of water used and this is by far the most critical parameter for fabricating a high quality polyurethane foam. For most polyols, water at 0.5 – 2.0PPHP mediates controlled foaming and yields final materials that are ~90% porous. However, sometimes the foaming reaction is uncontrolled and creates materials with large voids or heterogeneous pore sizes, thus necessitating the use of the pore stabilizer. The pore stabilizer is usually used in amounts from 0.5 – 2.0PPHP and will dampen the formation of large pores or voids in the foam. Unfortunately, too much pore stabilizer can hinder the gelling reaction so that the mechanical integrity of the foam is not maintained, i.e. the foam will collapse on itself during hardening. Therefore, the usual process for creating optimally porous foams is as follows: fabricate a 100mg foam with your new polyol batch using 1.5PPHP water and no pore stabilizer and allow to harden for 20min. Choose that amount of water if the foam reaches

the desired level of overall porosity, and adjust the amount of water up or down by 0.5PPHP to increase or decrease the overall foaming. If the foam produces large voids or irregularly sized pores, remake the sample using 0.5PPHP pore stabilizer oil and increase as needed until the pores seem homogenous. However, use a minimal amount of pore stabilizer if possible to ensure that the mechanical integrity of the polyurethane is maintained through the gelling process. After creating an optimal foam formulation for a new batch of polyol, the materials should be allowed to harden for at least 3-4 hrs but preferably at least 12 hrs or overnight. Scaffolds can be sterilized by ultraviolet light or gamma irradiation, though samples that contain drug payloads should be sterilized with ethylene oxide gas to avoid decomposition of the drug (though gas sterilized samples must be allowed to vent for at least 3 days to remove any excess gas from the material matrix).

E.2 siNP delivery from PTK-UR scaffolds for *in vivo* PHD2 knockdown

The local delivery of siRNA from implanted PTK-UR scaffolds, though offering promising results in wound healing applications, is a complex system and must be optimized at many different stages before successful *in vivo* implementation can occur. The first step is to develop a mechanically-optimized PTK-UR scaffold formulation (detailed in section E.2). The second step is to synthesize a nanoparticle with effective siRNA intracellular delivery. This is usually accomplished by synthesizing a small library of DMAEMA-*block*-(DMAEMA-*co*-BMA *co*-PAA) polymers (same block size of DMAEMA with varied block lengths of DMAEMA-*co*-BMA *co*-PAA) and then screening the nanoparticle activity by complexing siRNA that silences the gene luciferase with the polymeric micelles and treating luciferase-expressing cells. The polymer carrier that most effectively silences luciferase expression *in vitro* can then be used in the following studies. The third step is to screen a library of siRNA sequences against the target gene using your optimized nanoparticle carrier as screened by qRT-PCR.

The final parameter that can be modulated is the selection of and concentration of excipient used to stabilize the siRNA nanoparticles through lyophilization. Previous work has used trehalose at a dose of 60:1 weight ratio to siRNA, though this amount of trehalose has been shown to promote almost complete siRNA release over two days *in vivo*. This was reflected in the data presented in Chapter 4 as significant PHD2 silencing was seen at day 4 post scaffold implantation but was not sustained to day 7. Nelson et al. demonstrated that decreasing the amount of trehalose decreases the nanoparticle release rate, and in an unpublished study PTK-UR (LTI) scaffolds were loaded with PHD2 siRNA nanoparticles using a 12:1 weight ratio of trehalose to siRNA and implanted subcutaneously in rats. Unfortunately, PHD2 levels in PHD2 siRNA samples were as high as scrambled control siRNA scaffolds silencing at day 7 post implantation. The lower dose of trehalose slowed the siRNA release rate, but this excipient is also critical for maintaining nanoparticle activity through lyophilization, potentially indicating that the reduced dose of trehalose compromised the particles. This motivates future studies either exploring intermediate trehalose doses that can maintain particle activity but slowing release, using new excipients that better stabilize particles, or using siRNA delivery vectors that are more stable through lyophilization.

B.3 Rat ischemic wound model

As detailed in Chapter 4, excisional wounds in diabetic rats, despite their hyperglycemic state, still had almost complete tissue infiltration into implanted scaffolds after 4 days. This robust healing response makes it difficult to assess the viability of therapeutics which are designed to increase healing in chronic, non-healing wounds. To create a more impaired wound model, we have attempted to create a bipedicle flap in the dorsal skin of rats as described in Figure A20. The raised skin flap limits blood flow to the skin in the central portion of the flap to create an area of ischemia and reduced healing. Initial efforts to develop this model tried to underlay the raised skin flap with a piece of medical grade silicone sheeting above to limit the re-establishment of blood flow from the underlying tissue. However, this sheeting served to trap fluid and made the skin flap too ischemic to the point of necrosis and was not used in subsequent studies. The initial iterations of this wound model also utilized two 8mm diameter wounds in the center flap, one frontal and one distal from the horizontal center of the flap. Though the inclusion of two wounds are designed to increase the statistical throughput of the model, the excised wounds themselves decreased blood flow to the tissue between the two wounds causing necrosis. The initial flap also featured dimensions of 9cm length by 2cm width which was too narrow to allow for adequate blood flow to the center of the flap, causing necrosis. Therefore, the optimized flap did not have silicone sheeting and featured dimensions of 9cm by 2.5cm with a single 8mm diameter wound in the center of the flap. This configuration creates robust ischemia in the center of the flap which persists for 10 days, but not severe enough ischemia to create necrosis.